ChemPhysMater 3 (2024) 36–63

Contents lists available at ScienceDirect

ChemPhysMater

journal homepage: https://www.keaipublishing.com/en/journals/chemphysmater/

Review Article

Covalent organic frameworks: Design, synthesis, characterization, and applications

Solomon Oluwaseun Akinnawo*

Department of Chemical Sciences, Olusegun Agagu University of Science and Technology, P.M.B 353, Okitipupa, Nigeria

ARTICLE INFO

Keywords:
Crystalline
Covalent organic framework
Catalysis
Porous material
Wastewater treatment

ABSTRACT

Covalent organic frameworks (COFs) have emerged as an interesting class of crystalline porous materials with desirable properties (such as highly ordered porosity, structural versatility, high chemical and thermal stabilities, and facile surface modification) and a broad range of potential applications. This critical review is aimed at providing insight into design strategies and synthetic methodologies for COFs. Unlike previous reviews on COFs, this article also focuses on the characterization of COFs, which is important for understanding the physical and chemical properties of COFs that are essential for practical applications. Furthermore, this review highlights the applications of COFs in various fields, including catalysis, photovoltaic devices, sensors, supercapacitors, wastewater treatment, biomedicine, chromatographic and spectroscopic analyses, and gas separation and storage. Lastly, perspectives on future directions and challenges associated with COFs are provided.

1. Introduction

Covalent organic frameworks (COFs) are an emerging class of crystalline porous organic materials based on covalently bonded building blocks comprising light elements (e.g., C, H, O, N and B), which are interconnected to form extended two-dimensional (2D) or three-dimensional (3D) architectures [1]. Recently, considerable attention has been focused on the intriguing properties of COFs, which include highly ordered porosity, structural versatility, high chemical and thermal stabilities, and facile surface modification [1,2]. As a type of organic polymer, COFs are commonly synthesized via the reversible condensation of building blocks, resulting in long-range-ordered highly crystalline structures with self-healing properties and high thermal and chemical stabilities. The excellent chemical stability of COFs has been attributed to their metal-free structures and pure covalently bonded nature.

Similar to COFs, conjugated microporous polymers (CMPs) are also reticular organic materials containing rigid backbones and permanent pores with potential applicability for organic solvent nanofiltration. However, COFs are highly crystalline, whereas CMPs have amorphous 3D networks owing to rotation around the π-conjugated bonds in their skeleton structures [3–6]. Furthermore, unlike COFs, which are fabricated using covalently bonded building blocks containing light elements, CMPs are based on all-rigid porous frameworks composed solely of chemically inert C–H and C–C bonds [3,4,7-9].

Both COFs and their counterpart supramolecular organic frameworks (SOFs) are free from biotoxic metals. Nevertheless, unlike metal–organic frameworks (MOFs), COFs and SOFs typically exhibit weak phosphorescence owing to insufficient spin–orbital coupling and the rapid nonradiative decay of triplet excitons. However, COFs have highly stable porous structures, whereas the periodic porous architectures of SOFs comprise organic units linked through supramolecular interactions [10,11].

The first classes of porous nanomaterials to be reported were MOFs and zeolitic imidazolate frameworks (ZIFs), which consist of metal ion–organic ligand structures with coordinative bonds [1,2,12-14]. Compared with inorganic zeolites and other porous silica-based materials, COFs exhibit enhanced porosities. COFs also have organic metal-free structures, well-defined topologies, low mass densities, permanent porosity, excellent thermal resistance, and structural diversity. Moreover, the strong covalent bonds in COFs impart exceptional stability in organic and aqueous solvents [15,16]. In addition, π-stacking interactions and hydrogen bonds strengthen the porous skeletons of COFs, providing protection from hydrolysis and solvation. Owing to these advantageous properties, COFs have been applied in catalysis, gas adsorption and separation, optoelectronics, sensing, energy storage, and ion conduction [17–20].

Recently, numerous novel COFs with ordered honeycomb structures have been achieved by introducing diverse building blocks. This progress has driven improvements in facile strategies for constructing free-standing and flexible COF membranes via liquid–liquid interface-confined chemical reactions at atmospheric pressure and ambient temperature [17]. For COF membranes fabricated by this procedure, prop-

---

* Corresponding author.
E-mail address: seunangel@gmail.com

https://doi.org/10.1016/j.chphma.2023.08.003
Received 7 June 2023; Received in revised form 8 August 2023; Accepted 10 August 2023

erties such as aperture size and channel chemistry can be controlled by bridging the molecular building blocks using strong covalent bonds. Nonetheless, most COFs are prepared via the thermodynamically favorable reversible polymerization of monomers containing light elements (e.g., C, H, O, N, and B), resulting in highly crystalline frameworks with long-range 2D or 3D order owing to robust covalent bonds between the monomeric building blocks [15,21-23]. The fabrication of a 2D or 3D COF network depends on the geometries of the molecular precursors and their ability to form stacked or interconnected structure [24]. In this review, in-depth insight is provided into the design strategies, synthetic methodologies, and applications of COFs. Furthermore, characterization techniques for determining the properties of COFs are discussed in detail, as this topic has been overlooked in previous reports.

2. Design strategies

The fabrication of COFs has been based on achieving properties that are crucial for the desired application. For instance, the utilization of COFs for water treatment operations requires suitable pore sizes, hydrophilicity, a high surface area, and stability in water, which is particularly challenging. Therefore, the choice of design strategy and fabrication method is crucial for obtaining COFs with tailored properties. Generally, COFs are designed using either a bottom-up or top-down strategy. Reported bottom-up strategies include interfacial, solvothermal, and room-temperature vapor-assisted conversion synthesis methods. Top-down strategies typically involve solvent-assisted exfoliation, chemical exfoliation, and mechanical delamination or self-exfoliation.

2.1. Enhancing the stability of COFs

The first COFs based on boroxine and boronate ester linkages (COF-1 and COF-2, respectively) exhibit poor stability in aqueous solution owing to the reversibility of the dehydration reactions [2,10]. Consequently, nucleophilic attack on the boron sites of boroxine-linked COF-1 and boronate ester-linked COF-2 results in decomposition [25,26]. In contrast, imine-linked COFs exhibit superior water stability, which has been attributed to their electron-rich structural networks [27]. For example, with limited porosity and low crystallinity, imine-linked 3D COF-300, which is based on the same principle of triazine-, hydrazine-, and azine-linked COFs, displays improved aqueous stability [26–28].

Intramolecular hydrogen bonding has also been found to improve the aqueous stability of COFs. Furthermore, the conversion of linkages is an alternative strategy for increasing the aqueous stability of COFs. For example, direct oxidation can convert the imine linkages of COFs into amide linkages, which are expected to provide improved aqueous stability under basic and acidic conditions [29]. Lastly, combining water-durable materials with COFs has been suggested to improve the aqueous stability of the fabricated composites. Owing to its stability in aqueous solution, graphene oxide (GO) has been used to functionalize COFs, resulting in a water-stable graphene-synergized (GS)-COF composite [30].

2.2. Adjusting the pore size of COFs

The pore size is a key characteristic for determining the applications of COFs. Thus, to produce ideal COFs for a range of applications, the pore size should be considered during the design and fabrication stages. COFs with controlled pore sizes can be realized using two strategies: direct synthesis and post-modification [2]. The direct synthesis method involves the use of various organic linkers with different structures and lengths. For instance, COF-1, which was manufactured using diboronic acid (BDBA), had a pore size of 1.5 nm, whereas a COF directly synthesized using 2,3,6,7,10,11-hexahydroxytriphenylene (HHTP) and BDBA exhibited a pore size of 2.7 nm [2,10].

In the post-modification approach, the pore sizes of COFs are adjusted by selectively introducing side functional groups into the structural network. For example, post-modification was used to obtain X%RTrz COF-5, which had a smaller pore size than COF-5 [31]. In addition, annealing has been utilized as a post-modification strategy to adjust the porosity, pore sizes, and surface areas of COFs. For instance, carbon fibers can be annealed to obtain various micropore and mesoporous ratios and this post-modification approach can enhance the overall efficiency of COFs [10]. As another post-modification strategy, the topology-directed growth and pore-surface engineering of COF walls and functionalities can be used to adjust pore sizes. In the pore-surface engineering strategy, multicomponent reactions and multistep synthesis are carried out using alkene-, alkyne-, azide-, or phenol-functionalized building blocks that can undergo further quantitative reactions to generate pore surfaces with desirable functionalities [32,33]. The pore-surface engineering strategy is limited by the flexible and adaptive nature of the appended groups. Thus, a two-stage topology-directed growth process was developed to insert additional rigid building blocks with appropriate symmetries and dimensions to divide a mesopore into several micropores or ultramicropores. The corresponding one-stage synthetic method utilizing three building blocks was unsuccessful, as shown in Fig. 1(b) [33]. However, topology-directed growth was achieved by anchoring secondary active sites on the linkers in boronic ester-linked DBAAn-BTBA-COF in the post-synthetic route as shown in Fig. 1(a). This COF was synthesized via a solvothermal condensation reaction using 1,3,5-benzenetriboronic acid (BTBA) as the vertices and 4,4′-(2,3,6,7-tetrahydroxyanthracene-9,10-diyl)dibenzaldehyde (DBAAn) as linkers. Compared with the parent network (hexagonal-shaped Ph-An-COF), boronic ester-linked DBAAn-BTBA-COF exhibited a hexagonal skeleton with benzene as the corners and aldehyde-appended anthracene as the walls. Further, based on symmetry and dimension matching, hexaminophenyl benzene (HAPB) was deployed as a pore partition in DBAAn-BTBA-COF as shown in Figs. 1(c)(d) and Figs. 2(a)–(c). Notably, DBAAn-BTBA-HAPB-COF had a pore size of 6.5 Å, whereas the pore sizes of DBAAn-BTBA-COF were 10 and 29 Å, respectively, as shown in Figs. 2 (d)(e), (f)(g) and (h)(i) [33].

Furthermore, crystal-size-controlled synthesis can be used to adjust the pore size of COFs, which influences the properties and applications of these materials. For LZU-111, which is characterized by rigid spiral channels, the crystal size controls the pore surface area by influencing the pore integrity. In contrast, for COF-300, which is flexible with straight channels, the crystal size affects the structural flexibility by changing the number of repeating units and thus influencing the sorption selectivity [34].

LZU-111 crystals with a size of 200 nm were fabricated by directly mixing the building units without a modulator to achieve fast nucleation and crystallization of tiny crystals. The incorporation of different quantities of modulator controlled the degree of nucleation inhibition and growth controlling forces to decrease the crystallization rate, resulting in the formation of LZU-111 single crystals of various sizes. Furthermore, variable-temperature heating accelerated crystal growth to produce 30 μm LZU-111 within 10 days, whereas previous crystal growth methods produced 60 μm LZU-111 in tens of days [34].

Although LZU-111 and COF-300 both have tetrahedral nodes, their structures have different types of channels and framework motilities (Fig. 3(a)). LZU-111 crystallizes in the hexagonal system with a 3-fold interlocked lonsdaleite topology (lon-b-c3, Fig. 3(b)), whereas COF-300 crystallizes in the tetragonal system with a 7-fold interpenetrated diamond topology (dia-c7, Fig. 3(c)). Further, LZU-111 contains 3D spiral channels and a rigid framework (Fig. 3(d)) that does not undergo significant structural changes upon the incorporation of guest molecules (e.g., N_2 and 1,4-dioxane). In comparison, COF-300 has one-dimensional (1D) straight channels in a flexible framework that can adapt to guest molecules by forming contracted or expanded phases (Fig. 3(e)) [34].

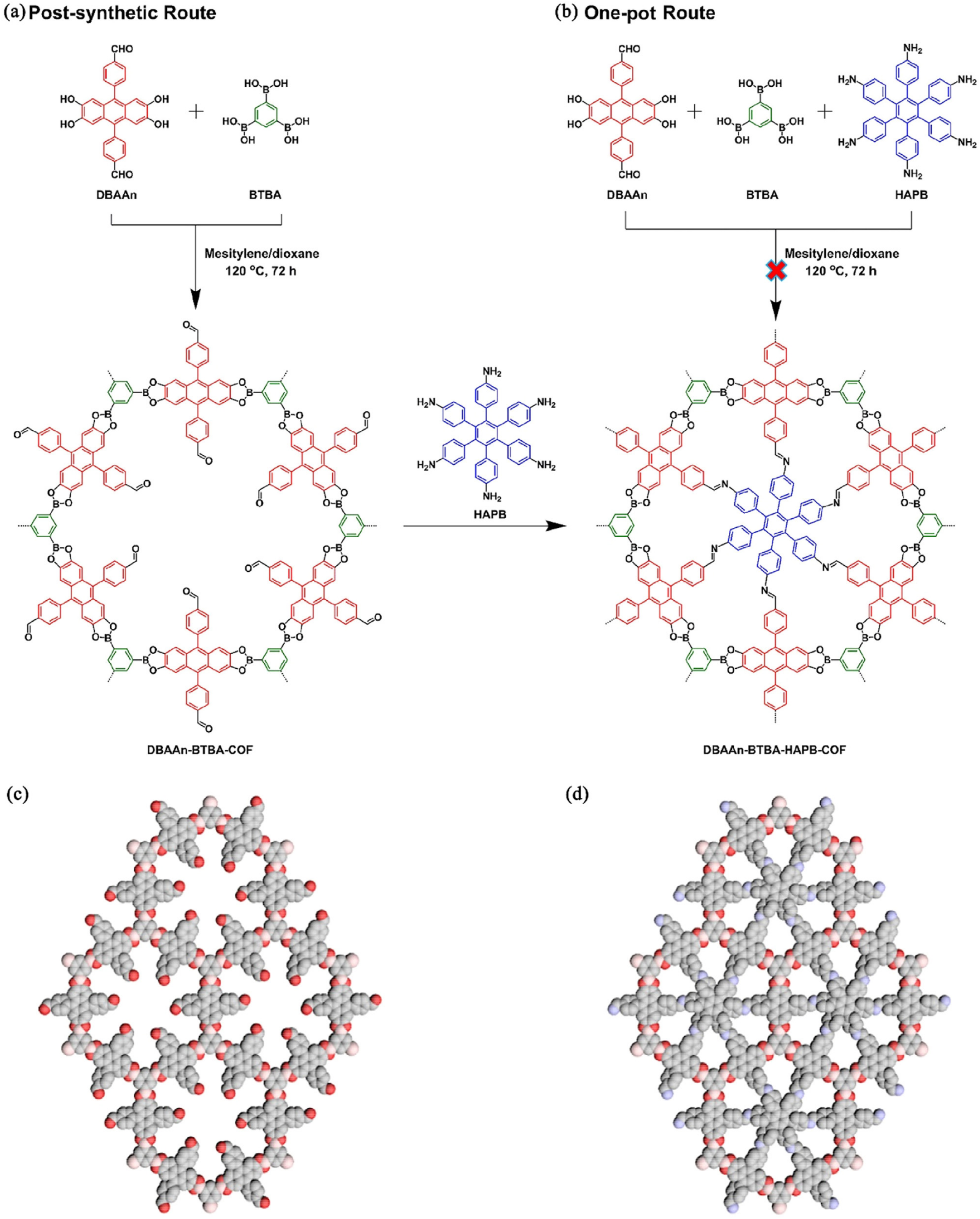

Fig. 1. (a) Post-synthetic route for DBAAn-BTBA-COF and DBAAn-BTBA-HAPB-COF, (b) one-pot synthetic route for DBAAn-BTBA-COF, (c) schematic diagram of DBAAn-BTBA-COF, and (d) schematic diagram of DBAAn-BTBA-HAPB-COF. Adapted from [33] under a Creative Commons license (CC BY 4.0).

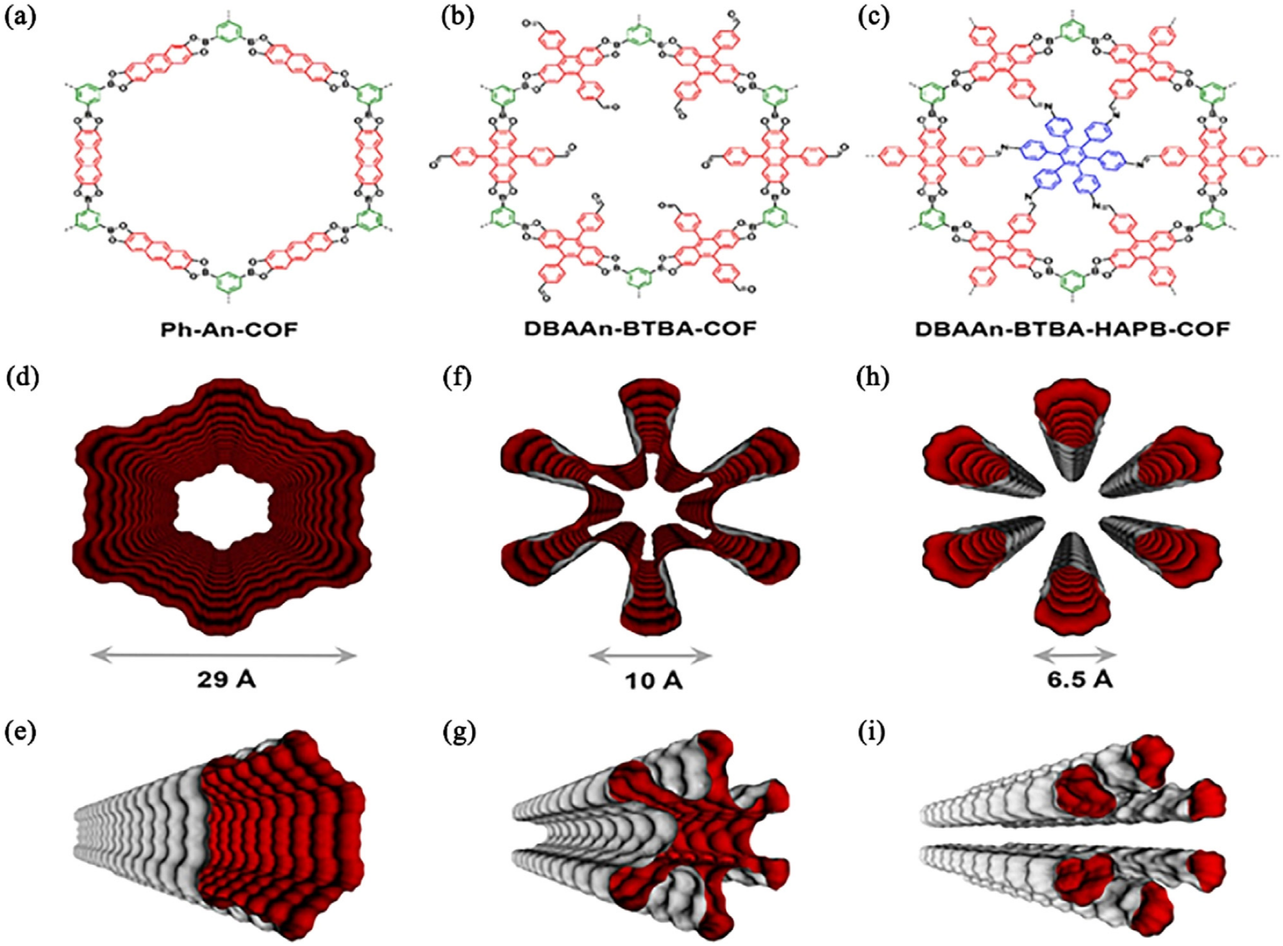

Fig. 2. (a)–(c) Structures of Ph-An-COF, DBAAn-BTBA-COF, and DBAAn-BTBA-HAPB-COF; top and side views of the van der Waals surfaces related to the 1D channels through (d)(e) Ph-An-COF, (f)(g) DBAAn-BTBA-COF, and (h)(i) DBAAn-BTBA-HAPB-COF. Adapted from [33] under a Creative Commons license (CC BY 4.0).

2.3. Functionalizing the structural networks of COFs

Functionalization, which is usually achieved by bottom-up synthesis or post-synthesis modification, can provide COFs with improved properties, such as the surface charge and hydrophilicity. Functional groups can be directly incorporated into the building units during the synthesis of COFs to yield COF-based hybrids or composites. The introduction of chelating groups is essential when synthesizing COFs that will be applied for the removal of metal ions [10,35]. Similarly, the surface charges of COFs should be considered for separation and adsorption applications. For instance, carboxyl functional groups can be incorporated into the structural network of COFs to impart the surface with a negative charge, thereby enhancing the ion rejection capacity of COFs [25,35].

COF nanosheets have been shown to have reduced mechanical strength because the interlamellar π–π interactions are weak. The mechanical strength of these nanosheets can be improved by combining porous 2D COFs with flexible and strong substrates, such as polyacrylonitrile (PAN) or carbon nanofiber. This design strategy has been found to improve the separation performance and mechanical strength of COF membranes owing to the synergetic effect of the properties of the substrate and COF membrane [36].

It should be emphasized as shown in Table 1, that the selection of materials for fabricating COF-based hybrids depends on the intended application. For instance, COF particles embedded in cross-linked polyamide can function as a selective layer during water treatment operations, including dye removal and seawater desalination. For ultrafiltration applications, design strategies such as graphene integration into COF thin films can improve desirable properties such as separation ability and water stability [37]. In addition, wood, which has high hydrophilicity, porous internal water transport pathways, low thermal conductivity, and low density, can be combined with a COF, which functions as photothermal material, to produce a wood@COF composite with a high evaporation efficiency for solar steam generation [38].

Table 1
Organic linkers frequently used as building blocks for COFs [39]

Name	Abbreviation
Triphenylamine	TPA
benzidine	BD
terephthalic dihydrazide	TPDH
o-tolidine	BD-Me$_2$
2,3,5,6-tetrafluoroterephthalaldehyde	TFTA
[1,1′-biphenyl]-4,4′-dicarbaldehyde	BPDA
1,3,5-triformylphloroglucinol	Tp
5,5′-diamino-2,2′-bipyridine	Bpy
trimesoyl chloride	TMC
2,6-diaminoanthraquinone	DAAQ
1,3,5-triformylbenzene	TFB, Tb
1,4-diaminobenzene	DAB
terephthaldicarboxaldehyde	TPDA
2,5-dihydroxyterephthaldehyde	DHTA
1,3,5-tris(4-aminophenyl)benzene	TAPB
2,5-dimethoxyterephthaldehyde	DMTP
2,4,6-tris(4-aminophenyl)-1,3,5-triazine	TAPT
4,4′,4″,4‴-(ethane-1,1,2,2-tetrayl)tetraaniline	ETTA
1,3,5-tris(*p*-formylphenyl)benzene	TFPB
p-phenylenediamine	Pa-1
tetra(4-anilyl)methane	TAM

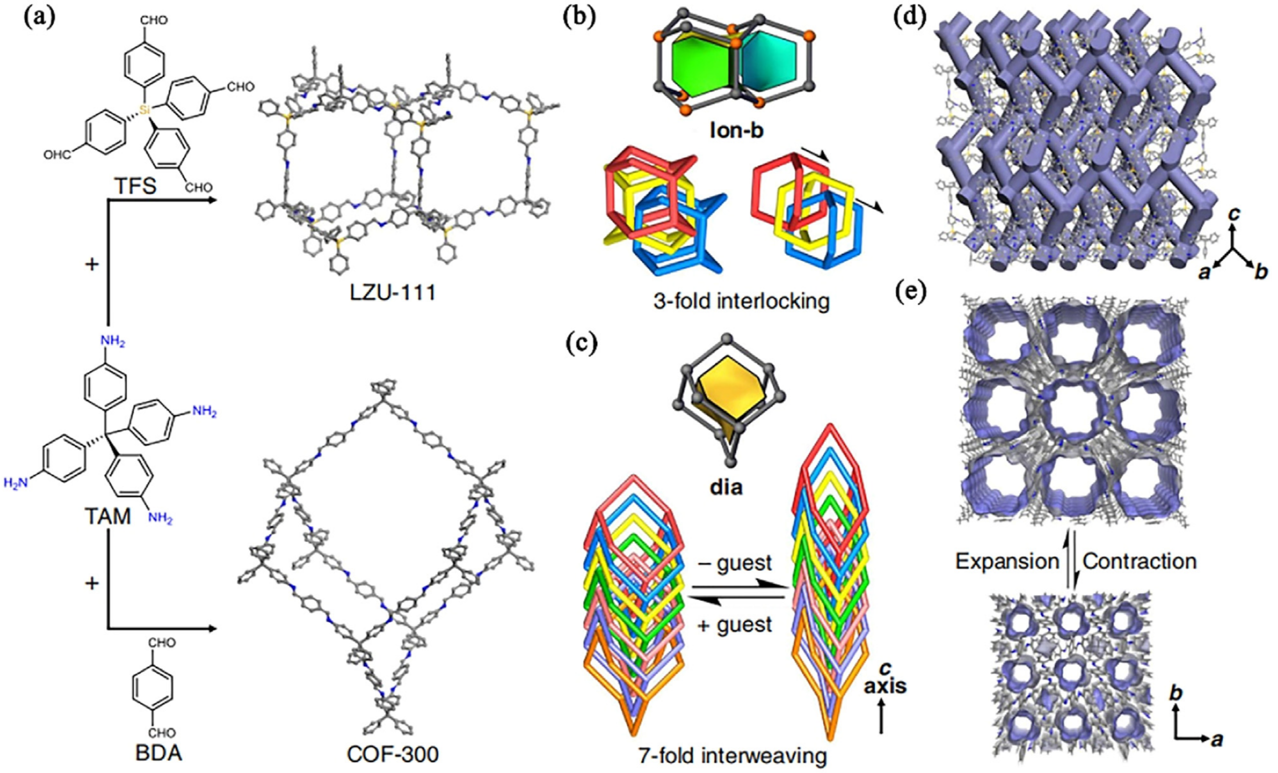

Fig. 3. (a) Synthetic routes and SXRD structures of LZU-111 and COF-300 (C, gray; Si, orange; N, blue; H is omitted for simplicity). LZU-111 consists of tetrakis(4-aminophenyl)methane (TAM) and tetrakis(4-formylphenyl)silane (TFS), whereas COF-300 consists of TAM and terephthaldehyde (BDA), (b) the lon-b net adopted by LZU-111 with characteristic 3-fold interlocking, (c) dia net adopted by COF-300 with 7-fold interweaving, which provides structural flexibility for guest inclusion and removal, (d) LZU-111 structure with 3D spiral channels, and (e) COF-300 structure with 1D channels that can contract and expand. Adapted from [34] under a Creative Commons license (CC BY 4.0).

2.3.1. Hybridization of COFs

The hybridization technique has been employed to fabricate COF-based composites or hybrids, which exhibit improved properties compared with their precursors. The hybridization technique is considered an effective approach for regulating and adjusting the pore structure of COF membranes by incorporating ultramicroporous MOFs or ZIFs to form MOF/COF and ZIF/COF hybrids. For example, the ZIF/COF hybrid formed by incorporating ZIF-67 into TpPa-1 had a pore size range of 0.29–0.5 nm, whereas TpPa-1 alone exhibited a larger pore size of 1.83 nm [32].

2.3.1.1. Metal-based COF composites.

2.3.1.1.1. Silicon dioxide–COF composites.

With the aim of fabricating COFs with desirable properties, strategies for growing uniform COF shells on SiO_2 microspheres have been developed. As a representative example, uniform core–shell COF@SiO_2 microspheres were fabricated using spherical 5 µm amino silica (SiO_2-NH_2) as both the core and a source of amino groups for the reaction with 1,3,5-triformylphloroglucinol (Tp) to achieve controllable shell growth [39,40]. Subsequently, benzidine (BD) was reacted with SiO_2-Tp to fabricate a TpBD shell on the SiO_2 core [40]. In another significant example, a 3D COF was synthesized on SiO_2 by refluxing SiO_2-NH_2 with terephthaldehyde (TPDA) and tetra(4-anilyl)methane (TAM) over several cycles to yield polymer@SiO_2, which was transformed into structurally ordered COF-300@SiO_2 under solvothermal conditions [41].

2.3.1.1.2. Iron oxide–COF composites.

Among metal-based COF composites, magnetic composites based on iron oxide nanoparticles (NPs) have been widely investigated owing to their remarkable magnetic properties, which allow rapid separation under an external magnetic field, high chemical and thermal stabilities, and biocompatibility [39]. In a typical synthetic procedure for an Fe_3O_4-COF nanocomposite, Fe_3O_4 NPs were synthesized and then applied to modify the surface of the COF using amino functionalities as anchoring groups [39,42]. In addition, magnetic COFs (MCOFs) were fabricated by sequentially modifying Fe_3O_4 NPs with (3-aminopropyl)trimethoxysilane and tetraethyl orthosilicate to obtain MNP-NH_2, which was then incorporated into the structural network of a COF to yield MCOF-1, MCOF-2, MCOF-3, MCOF-4 containing 50, 10, 150, and 200 mg of MNP-NH_2, respectively [43].

2.3.1.1.3. Aluminum oxide–COF composites.

The surface modification of a porous α-Al_2O_3 ceramic with (3-aminopropyl)triethoxysilane (APTES) followed by 4-formyphenylboronic acid treatment was used to fabricate α-Al_2O_3-functionalized COF-5 [39,44,45]. Using a similar procedure under solvothermal conditions, an imine-based 3D COF-320 with good structural stability was grown on an α-Al_2O_3 ceramic support. Furthermore, an α-Al_2O_3-COF consisting of a high-grade imine-linked COF-LZU1 membrane supported on α-Al_2O_3 tubes, was fabricated to achieve good thermal and chemical stabilities [46]. Recently, 2D COF layers were grown within the skeletal framework of a vertical aligned CoAl layered double hydroxide, which functioned as a template for the fabrication of COF-LZU1 [46,47].

2.3.1.1.4. Other metal-based COF composites.

Progress has also been made in the fabrication of other metal-based COFs composites, such as Co_3O_4-COF, which consisted of aggregated particles covered by a smooth COF shell with a thickness of 15–35 nm [39]. Moreover, covalent bonding was achieved between Ti and TpBD COF. TiO_2 nanotube arrays provided Ti-OH moieties that were modified with APTES and then functionalized with Tp to grow TpBD COF under solvothermal conditions. The fabricated TiO_2-TpBD COF composite consisted of fibers with spherical structures on the surface and a Ti coating with a thickness of 15–20 μm [48].

A Pd/COF composite was prepared by diffusing [Pd(η^3-C_3H_5)(η^5-C_5H_5)] as a volatile precursor into porous COF-102 followed by UV-light irradiation to form Pd NPs. The average size of the Pd NPs (2.4 ± 0.5 nm) was larger than the pore diameter of COF-102 (0.9 nm) [49]. Nevertheless, as the structure and crystalline network were maintained, the growth of the Pd NPs was proposed to involve pore alignment [49]. In another example, $Pd(OAc)_2$ was utilized as a precursor for loading Pd NPs into the framework of TpPa-1 to fabricate a Pd/TpPa-1 composite. Similarly, as a metal precursor that interacts with oxygen and nitrogen atoms, $HAuCl_4$ was used to synthesize an Au/TpPa-1 composite [50,51].

In addition, Au NPs were immobilized on TAPB-DMTP COF via electrostatic interactions with unsaturated amino groups on the COF surface to fabricate an Au/TAPB-DMTP composite that retained the crystalline nature of TAPB-DMTP COF [52]. However, this composite the surface area of this composite (1915 m^2 g^{-1}) was smaller than that of bulk TAPB-DMTP COF (2385 m^2 g^{-1}). This decrease in surface area was attributed to difficulties in controlling the growth of the Au NPs within the porous COF. In another study, Au and Pt NPs were incorporated in the framework of TAPB-DMTP COF to fabricate Au/TAPB-DMTP COF and Pt/TAPB-DMTP COF composites. Notably, 3.8 nm Pt NPs and 50 nm Au NPs were successfully introduced into TAPB-DMTP-COF without compromising the framework structure or composition [52].

Furthermore, heteroatom-rich acylhydrazone-linked COF-ASB, which was fabricated via the condensation of benzene-1,3,5-tricarbohydrazide and benzene-1,4-dicarboxaldehyde, was loaded with Ru NPs through $RuCl_3$ infiltration followed by $NaBH_4$ reduction. The Ru/COF-ASB composite contained homogeneously distributed Ru NPs (4.1 wt.% loading) with sizes in the range of 2–5 nm, and the physical and chemical properties of COF-ASB were maintained [53]. In another study, $PdCl_2$ was utilized as a metal precursor to functionalize a bipyridine (Bpy) building block for fabricating a Pd/TpBpy composite. Ruptured linkages between the building block and Pd precursor resulted in the growth of Pd NPs during the synthesis of the COF. The Pd/TpBpy composite exhibited a crystalline structure with a pore size distribution (PSD) of 1.4–2.3 nm [54]. Lastly, Ag/COF-LZU1 was obtained in a single step by growing Ag NPs from Ag ions (added as $AgNO_3$) on presynthesized COF-LZU1 in deionized water under ambient conditions. Similar findings have been reported with other ions, including Cu [55,56].

2.3.1.2. *Stainless steel–COF composites.*

Various stainless steel–COF composites have been produced. For example, a key COF building block (1,3,5-tris(*p*-formylphenyl)benzene, TFPB) was used to modify APTES-functionalized stainless-steel wire. Subsequent immersion in a solution containing BD (another COF building block) and acetic acid as a catalyst for 3 days under ambient conditions produced TFPB-BD-bonded fibers [57,58]. In another study, APTES-functionalized stainless-steel wires were immersed in a solution of COF building blocks in the presence of a catalyst [57,58]. Such stainless steel–COF composites have generated interest for solid-phase extraction and separation [59].

2.3.1.3. *Graphene-based COF composites.*

A GS-COF composite was developed via a solvothermal method with graphene, Tp, and 2,6-diaminoanthraquinone (DAAQ) as precursors. The corresponding oxime-containing o-GS-COF composite was characterized by a lamellar structure, indicating that the surface morphology of o-GS-COF was affected by oxime modification and intercalation effects between graphene and the COF [37,60].

GO-based membranes typically display undesirable properties, including poor water and organic solvent fluxes. To improve the permeate flux, GO was integrated with a COF synthesized using TFB and Pa-1 under solvothermal conditions to develop nanostructured GO/COF hybrid membranes with various GO/COF ratios [61]. In addition, GO and Fe_3O_4 NPs were used to prepare a COF-decorated graphene/magnetite composite (MagG@COF-5), which displayed desirable characteristics [62,63].

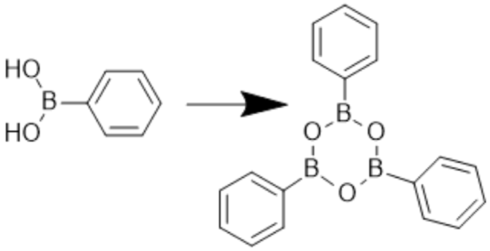

Fig. 4. Boroxine linkage of COFs.

2.3.1.4. *COF–MOF composites.*

The hybridization of COFs with MOFs has been reported to yield composites with improved properties. Notably, the integration of MOFs into the structural networks of COFs has been demonstrated to yield hybrid COF–MOF materials that are suitable for ratiometric fluorescence detection. A lanthanide organic framework was grown on the surface of a carboxyl-functionalized fluorescent COF under solvothermal conditions. The reaction between the surface –COOH groups, Eu^{3+} ions, and ligands ensured the integration of the MOF on the COF, thereby yielding a hybrid COF–MOF material with high chemical and thermal stabilities [64]. Furthermore, this COF–MOF composite exhibited dual emission at 446 and 621 nm, indicating that fluorescence resonance energy transfer occurred from the COF to MOF. The dual emission properties, structural stability, and high phosphate affinity of this COF–MOF system allowed for the ratiometric fluorescence detection of phosphate [64].

As porous materials, both COFs and MOFs have been utilized for membrane-based gas separation. To fabricate COF–MOF composite membranes, polyaniline-modified SiO_2 disks were coated with COF-300 and subjected to COF growth conditions in a Teflon-lined autoclave. Subsequently, an MOF was added using a similar procedure. The resulting composite membranes, including [COF-300]-[$Zn_2(bdc)_2(dabco)$] and [COF-300]-[ZIF-8], exhibited improved selectivity for H_2/CO_2 gas blends compared with the individual MOF and COF membranes [65].

2.3.1.5. *Polymer–COF composites.*

Polymeric membranes often suffer from physical ageing, plasticization, poor thermal stability, low selectivity–permeability, and membrane fouling. Thus, to enhance the properties of polymeric membranes, polymer–COF composites have been fabricated [66,67]. A polyvinylidene fluoride (PVDF)/COF membrane was synthesized under ambient conditions via the unidirectional diffusion of TpPa-1 on a commercially available PVDF microfiltration substrate [66,67]. Similarly, a polymer–COF hybrid membrane was prepared using a solution casting technique with dimethylacetamide (DMAc) as the solvent. Specifically, a polybenzimidazole (PBI-BuI) solution in DMAc was mixed with a COF suspension to fabricate highly flexible COF(*n*)@PBI-BuI hybrid membranes [66,67].

2.3.2. *Linkages of COFs*

2.3.2.1. *Single-linkage strategies.*

2.3.2.1.1. *Boron-containing COFs.*

Following the pioneering studies by the Yaghi group on COF synthesis, various reports have focused on the use of boronated esters or boronated anhydrides to synthesize boron-containing COFs [1]. These boron-containing COFs can be classified according to two condensation strategies. First, the self-condensation of a single building block results in cyclic six-membered boroxine-linked COFs (Fig. 4). Second, the co-condensation of boronic acids and catechol derivatives results in five-membered boronate ester COFs (Fig. 5) [1].

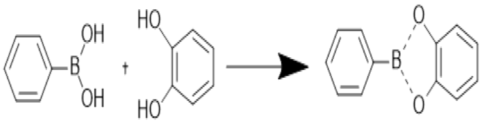

Fig. 5. Boronate ester linkage of COFs.

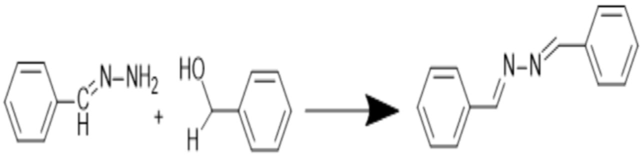

Fig. 6. Azine linkage of COFs.

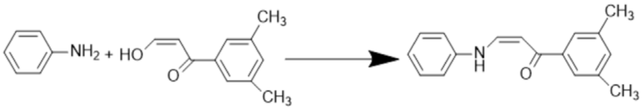

Fig. 7. Ketoenamine linkage of COFs.

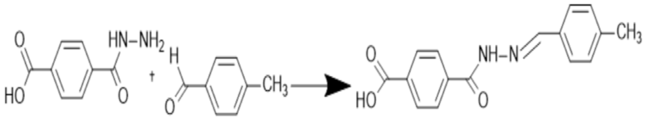

Fig. 8. Hydrazone linkage of COFs.

2.3.2.1.2. Azine-based COFs.

A larger number of COFs have been synthesized based on azine linkages (–C=N–N=C–, Fig. 6) [1,68]. In azine-linked COFs, a short hydrazine monomer is used to connect two aldehydes to form a polygon skeleton with small pores. Furthermore, a variety of knots, such as pyrene, benzenes, triphenylbenzene, and triphenyltriazine (TPT), have been investigated for the synthesis of azine-linked COFs with various topologies, including hexagonal, trigonal, and rhombic topologies [69–72].

2.3.2.1.3. Ketoenamine-based COFs.

Ketoenamine-based COFs have been fabricated using the irreversible enol–keto tautomerization of ketenimine linkages in imine-based COFs prepared using building blocks with –OH and CHO aldehyde groups (Fig. 7). Ketoenamine-based COFs have been reported to have high chemical stability, which is advantageous for many applications [73,74]. However, ketoenamine-based COFs exhibit decreased crystallinity because the irreversibility of enol–keto tautomerization impedes error correction in the COF lattice [74].

2.3.2.1.4. Hydrazone-based COFs.

The co-condensation of hydrazides and aldehydes in the presence of acetic acid as a catalyst has been used to fabricate hydrazine-linked COFs (Fig. 8). Notably, the incorporation of ethoxy units at the ortho position of knot building units, including 2,5-diethoxyterephthalohydrazide (DETH), is critical for realizing hydrazine-linked COFs through the introduction of intramolecular hydrogen bonds [1]. The DETH building block has been combined with various aromatic aldehydes to obtain COF-42, COF-43, and COF-JLU4 [75,76]. In addition, TpODH COF was synthesized from TFP-3OHCHO and the aliphatic hydrazone linker oxalyldihydrazide (ODH) in a mixture of 1,4-dioxane and mesitylene, whereas mixtures of THF and mesitylene were used to synthesize TFTP-COF and LZU-21 [77,78].

2.3.2.1.5. Imide-based COFs.

The synthesis of COFs with imide linkages can be achieved through the condensation of an amine with an acetic hydride at high temperatures of ~250 °C (Fig. 9). Various imide-linked COFs, including 2D polyimide (PI) COFs such as PI-COF-1 and PI-COF-2 synthesis require heating at 200 °C for 5 days, whereas PI-COF-3 synthesis require heating at 250 °C for 7 days, have been fabricated by reacting triamine building units with aromatic dianhydrides under solvothermal condition in *N*-methyl-2-pyrrolidone/mesitylene mixtures in the presence of isoquinoline as a catalyst [79,80]. In contrast, the construction of PI-COF-4 and PI-COF-5, which are 3D COFs, required a lower temperature of 160 °C for 5 days [80].

2.3.2.1.6. Imine-based COFs.

Imine-based COFs have been synthesized using a Schiff base reaction (Fig. 10), which involves the co-condensation of aldehydes and aromatic amines in the presence of a Lewis acid catalyst or organic acid [26,81]. Imine-based COFs can be classified as having trigonal, tetragonal, rhombic, hexagonal, or Kagome structures. The co-condensation of 1,4-diaminobenzene and 1,3,5-triformylbenzene in 1,4-dioxane was used to prepare COF-LZU1 [1,82-86]. This imine-based COFs exhibited superior structural regularity, chemical stability, crystallinity, and catalytic activity for Suzuki–Miyaura coupling reactions when compared with boron-based COFs [1,82].

2.3.2.1.7. sp^2-hybridized-carbon-conjugated COFs.

The Knoevenagel condensation of an aldehyde and a benzyl cyanide in the presence of a base as a catalyst is effective for preparing fully π-conjugated COFs (Fig. 11). For instance, the first C=C-linked COF (sp^2c-COF) was synthesized via the condensation of tetrakis(4-formylphenyl) pyrene and 1,4-phenylenediacetonitrile in a mixture of 1,4-dioxane and mesitylene with a 4 M NaOH aqueous solution as the catalyst [87,88]. Similarly, the condensation of 1,4-phenylenediacetonitrile and 1,3,5-tri(4-formylphenyl)benzene, a three-armed aromatic aldehyde, in *o*-dichlorobenzene with cesium carbonate as the catalyst was used to fabricate a 2D poly(phenylenevinylene) framework [88]. Furthermore, a 2D porphyrin-based sp^2-hybridized-carbon-conjugated COF (Por-sp^2c-COF) and 2D TP-COF with a triazine central planar unit bridged by sp^2-hybridized carbon linkers were constructed in 1,4-dioxane/$CHCl_3$ mixtures [89,90].

2.3.2.1.8. Other single linkages in COFs.

Other types of single linkages, including borazine (Fig. 12), phenazine (Fig. 13), triazine (Fig. 14), urea, squaraine (Fig. 15), dioxin (Fig. 16), azodioxide (Fig. 17), oxazole (Fig. 18), thiazole (Fig. 19), and viologen, have also been used to prepare COFs [23]. Compared with imine-, azine-, and hydrazone-linked COFs, those with triazine or phenazine linkages have been reported to exhibit enhanced chemical stability and extended π-conjugation, which are advantageous for photocatalytic applications [23,91]. Compared with COFs with imine link-

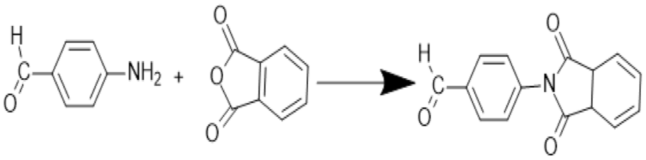

Fig. 9. Imide linkage of COFs.

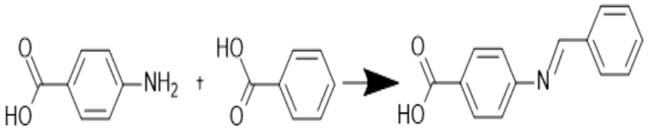

Fig. 10. Imine linkage of COFs.

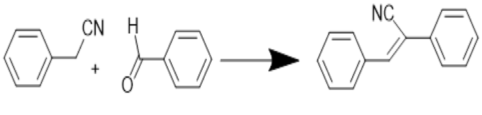

Fig. 11. C=C linkage of COFs.

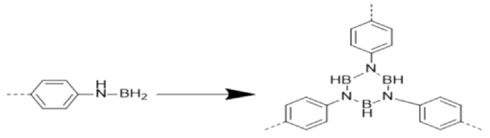

Fig. 12. Borazine linkage of COFs.

ages, COFs with sp^2-carbon linkages have conjugated structures with high chemical stability, increased electron delocalization, and charge transfer properties. However, the poor reversibility of C=C bonds has been reported to contribute to the complexity of constructing crystalline sp^2-carbon-linked COFs [91,92]. Post-synthesis modification has been used to convert one type of COF linkage to another, which is unattainable via the polycondensation method. In a typical example, the hydrogen perchloride-mediated oxidation of the imine linkages in a COF can produce amide-linked COFs. Similarly, imine linkages in COFs can be transformed into amide linkages via $NaBH_4$-mediated reduction. Imine-linked COFs have also been converted into oxazole- and thioazole-linked COFs [91–94].

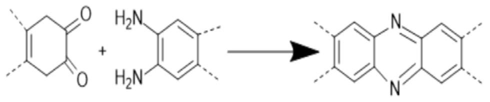

Fig. 13. Phenazine linkage of COFs.

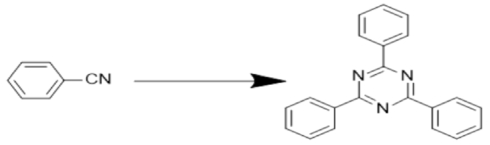

Fig. 14. Triazine linkage of COFs [95].

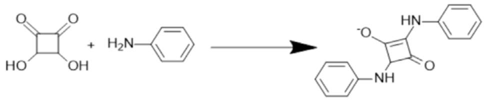

Fig. 15. Squaraine linkage of COFs.

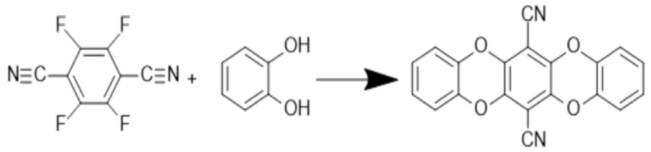

Fig. 16. Dioxin linkage of COFs.

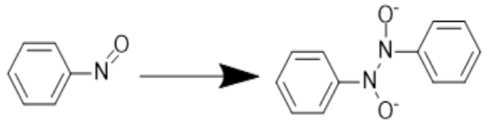

Fig. 17. Azodioxide linkage of COFs.

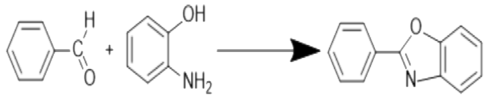

Fig. 18. Oxazole linkage of COFs.

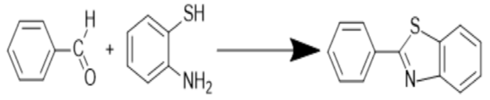

Fig. 19. Thiazole linkage of COFs.

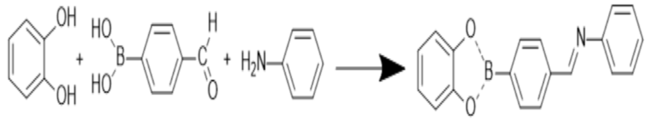

Fig. 20. Dual linkage of COFs.

2.3.2.2. Dual linkages.

In addition to COFs with single linkages, which have been widely reported, various COFs with dual linkages have been synthesized using monomers with bifunctional groups. As a typical monomer, 4-formylphenyl boronic acid (FPBA) has bifunctional reactive sites that can form boronate esters with imine or hydrazone linkages and boroxines with imine linkages (Fig. 20), which can be exploited to realize tetragonal and hexagonal rhombic topologies [96–98]. For example, a double-linkage strategy, in which the bifunctional monomer FPBA was condensed with HHTP and 4,4′,4″-(1,3,5-triazine-2,4,6-triyl)trianiline (TATTA), was used to fabricate HHTP-FPBA-TATTA COF [96]. Similarly, a 2D COF was prepared by the condensation of FPBA with 1,3,5-tris(4-aminophenyl)benzene (TAPB) and HHTP. The strategy was also employed to synthesize 3D COFs using monomers that can form dual imine and boroxine linkages [97,98].

3. Synthetic methodologies for COFs

3.1. Solvothermal synthesis

In solvothermal synthetic methods, a reaction mixture in a nonaqueous or organic solvent and occurs is placed in a closed system under a certain pressure and temperature, which affects the porosity and crystallinity of the resulting COFs [23,91,99]. Solvothermal synthesis is the most common method for preparing COFs, typically via ligand-exchange or Schiff base reactions at 80–120 °C, depending on the chemical reactivity of the building blocks [26,100,101]. To optimize the COF yield and performance, a reaction time of at least 3 days is typically required. COFs are typically collected as precipitates, washed using suitable solvents, and dried under vacuum to obtain a pure solid [23,100,102,103].

Strategic solvent selection is crucial for the preparation of COFs owing to the strong effect of the solvent on reaction solubility, which can influence the reaction rate, crystal growth, crystal nucleation, and self-healing properties [1,91,104]. Furthermore, solvent mixtures have been employed to synthesize COFs in the presence of acidic catalysts, but challenges remain in the selection of suitable solvents for the construction of crystalline COFs [91,105]. The major limitation of COF synthesis via the solvothermal technique is the difficulty in scaling up to industrial production owing to slow reaction rates and the requirement for high temperatures and pressures [23,91,103].

3.2. Ionothermal synthesis

The ionothermal synthetic method utilizes a molten salt or ionic liquid as both the solvent and catalyst. Advantageously, ionic liquids are reusable and their properties can be modified by varying the counter anion. Moreover, when employed for COF production, ionic liquids yield desirable properties, such as high stability and periodicity [91,106-108]. Typically, COF synthesis via ionothermal methods requires a temperature of approximately 400 °C, which restricts the application of various monomers. Notably, ionothermal synthesis was employed for the trimerization and cyclization of nitrile structural units in molten $ZnCl_2$ at 400 °C to fabricate porous crystalline COFs with high crystallinity as well as high thermal and chemical stabilities [95,109]. Furthermore, an ambient temperature and pressure ionothermal technique was used to produce 3D COFs (3D-IL-COFs) via Schiff base formation with 1-butyl-3-methylimidazolium bis((trifluoromethyl)sulfonyl)imide acting as both the catalyst and solvent. The 3D-IL-COFs were obtained with a relatively short reaction time of 12 h, whereas conventional synthetic methods require 3–7 days [99].

However, the elevated temperatures required for ionothermal synthesis can results in the decomposition of building blocks, unwanted side reactions and byproduct formation, and poor molecular ordering resulting from amorphous monomers. Owing to these disadvantages, the large-scale application of ionothermal synthesis has not yet been realized [91,103,108,110].

3.3. Microwave-assisted synthesis

In microwave-assisted synthetic methods, microwave irradiation is used as an efficient energy source for the production of crystalline COF materials. There numerous benefits associated with this approach, such as accelerated reaction rates, increased COF yields, lower energy consumption, enhanced reaction selectivity, and milder reaction conditions. Hence, microwave-assisted synthesis has potential for the industrial fabrication of COFs [23,91,108]. Another advantage of microwave-assisted synthetic methods is the ability to monitor the reaction progress and simultaneously control the reaction temperature and pressure. Microwave-assisted synthesis has been reported to produce COFs with desirable properties, including high crystallinity and stability, similar to ionothermal and solvothermal synthetic methods [23,103,108].

Recently, COF-5 was synthesized using microwave irradiation at a power of 200 W with stirring for 20 min at 100 °C. Notably, the reaction time was 200 times faster than that required for the conventional solvothermal method (72 h) [2,111,112]. In addition, COF-5 prepared via the microwave-assisted synthetic route contained fewer impurities and had a larger surface area than COF-5 synthesized via the conventional solvothermal method [1,111,112].

3.4. Room-temperature synthesis

Room-temperature synthesis yields COFs with high thermal and acid–base stabilities as well as high surface areas, resulting in enhanced adsorption capacities. Despite the advantages of synthesizing COFs under ambient conditions, the large-scale fabrication of COFs using room-temperature methods requires expensive reagents, including ionic liquids and metal triflate catalysts [91,104,108]. There are two main room-temperature synthetic methods: mechanochemical grinding and the solvent method. Mechanochemical grinding is a facile, solvent-free, economical, and environmentally friendly technique, whereas the solvent method involves the use of large quantities of solvent. However, COFs fabricated via mechanochemical grinding have been reported to exhibit low surface areas, porosity, and crystallinity compared with those synthesized using solvothermal methods [91,108,113].

Nonetheless, the mechanochemical grinding method has received considerable attention because of its simplicity, as it can be performed by manual grinding with a mortar and pestle. This solvent-free route has been explored for the synthesis of COFs using a Schiff base condensation reaction at room temperature, in which COF formation was indicated by a change in color [114–117]. Moreover, COFs with graphene-like layered structures have produced by the exfoliation of COF layers during mechanochemical synthesis. In addition, COF TpAzo was synthesized in a short time (20 min) via the condensation of 4,4-azodianiline (Azo) and Tp. This COF exhibited a sheet-like morphology, high porosity, and thermal stability [1,117].

3.5. Sonochemical synthesis

Sonochemical synthetic methods are more favorable than conventional methods in terms of reaction rates and costs. During sonochemical synthesis, ultrasound-induced bubbles in a solvent grow and collapse by cavitation, thereby providing extremely high and localized temperatures and pressures that can initiate and accelerate chemical reactions [1,118]. This method was effectively employed to fabricate COF-1 with a high surface area of 2122 m^2 g^{-1} using a reaction time that was 400 times faster than that required for the conventional synthetic method. Similarly, a sonochemical method was used to synthesize COF-5 on the surface of graphene and carbon nanotubes, with the aim of forming core–shell structures [1,119,120].

3.6. Light-induced synthesis

Light-induced synthesis has been used to prepare new highly crystalline and conjugated COFs under simulated sunlight irradiation in the wavelength range of 200–2500 nm in the presence of a co-catalyst. Specifically, a mixture of a hexaketocyclohexane octahydrate and 1,2,4,5-benzenetetramine tetrahydrochloride was dissolved in a solvent mixture under an inert atmosphere in the presence of water with acetic acid as a co-catalyst to induce the condensation reaction [1,121]. Crystalline and amorphous hcc-COF were obtained in the presence and absence of light, respectively. The crystalline hcc-COF exhibited desirable properties, including a high electrical conductivity of 2.22×10^{-3} S m^{-1}, likely because charge transfer was enhanced by the formation of an extended conjugated structure [1,121].

4. Characterization of COFs

The complex chemical structures and wide application range of COFs necessitate the characterization of COFs using various analytical methods.

4.1. Fourier transform infrared (FTIR) and Raman spectroscopy

FTIR spectroscopy was used to characterize the functional groups in the as-prepared crystallites of a unique heteroporous COF (COF-ETTA-2,3-Dha) fabricated using 4,4′,4′′,4′′′-(ethane-1,1,2,2-tetrayl)tetraaniline (ETTA) and 2,3-dihydroxybenzene-1,4-dicarbaldehyde (2,3-Dha) as building blocks [17]. The FTIR spectrum revealed the nearly complete disappearance of the peaks at 1649 cm^{-1}, corresponding to C=O in 2,3-Dha, and 3437 and 3353 cm^{-1}, corresponding to $–NH_2$. This behavior indicated a high degree of polymerization owing to the consumption of most of the amine and aldehyde groups in the monomers [17]. Simultaneously, a new band appeared at 1615 cm^{-1}, which was attributed to C=N bonds in imine linkages [17].

Similarly, FTIR spectroscopy was employed to characterize Cd(II)-captured COF-ETTA-2,3-Dha (COF-ETTA-2,3-Dha-Cd). Notably, the O–H bending vibration shifted from 1359.2 cm^{-1} for COF-ETTA-2,3-Dha to 1358.0 cm^{-1} for COF-ETTA-2,3-Dha-Cd. This change was attributed to the adsorption of Cd in the pores of COF-ETTA-2,3-Dha [17].

In addition, a series of sp^2 carbon-conjugated COFs (sp^2c-COF, sp^2c-COF-2, and sp^2c-COF-3) with different sizes of π-lattice comprising tetraphenylpyrene knots with phenyl, biphenyl, and terphenyl linkers, respectively, were fabricated by C=C polycondensation and characterized using FTIR spectroscopy. FTIR analysis confirmed the construction of sp^2-carbon-conjugated COFs via the appearance of a new C≡N vibration band at 2220 cm^{-1} accompanied by a significant decrease in the vibration band at 2720 cm^{-1} corresponding to the C–H stretching vibration of aldehydes in the linkers [110].

The FTIR analysis of COF-DANC-A composites, which were fabricated by incorporating 2,3-dialdehyde nanocrystalline cellulose (DANC) into COF-TpPa-1, revealed strong characteristic peaks at approximately

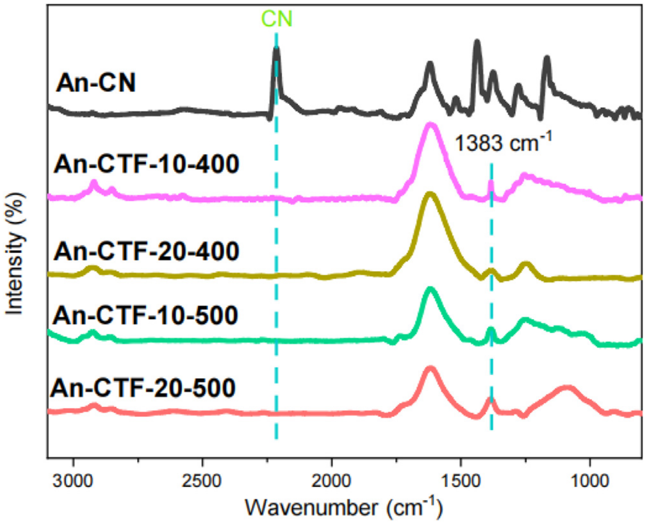

Fig. 21. FTIR spectra of An-CN, An-CTF-10-400, An-CTF-20-400, An-CTF-10-500, and An-CTF-20-500. Adapted from [9] under a Creative Commons license (CC BY 4.0).

1400 and 2900 cm^{-1} corresponding to the C–H bonds in DANC. Moreover, the characteristic peak at 1629 cm^{-1}, ascribed to the C=N stretching vibration, was an indication of imine bond formation. A decrease in the peaks corresponding to C–N bonds in the studied COFs and C=O in DANC indicated the successful incorporation of DANC into the structural network of the COF to obtain COF-TpPa-1 [122–125].

The FTIR spectra of 9,10-cyanoanthracene (An-CN) and corresponding covalent triazine frameworks (CTFs) are compared in Fig. 21. For An-CN, the peak at 2220 cm^{-1} corresponds to the CN groups. For the An-CTFs, the peaks at 1383 and 1566 cm^{-1}, attributed to triazine rings in the CTF, and the absence of the CN peak confirm the cyclization (trimerization) of the nitrile groups [9].

Raman spectroscopy can be used to investigate the defect properties and degree of graphitization exhibited by carbon materials based on bands in the range of 1200–1700 cm^{-1}. As shown by the Raman spectra of the An-CTFs in Fig. 22, two strong peaks are located at 1350 and 1602 cm^{-1} which are characteristic of the D and G bands, respectively, thus confirming the presence of graphitic carbonized structures and carbonaceous materials formed by the CTFs. The D and G bands represent sp^2 and sp^3 hybridization, respectively, corresponding to first- and second-order Raman scattering [9]. I_D/I_G ratios of 1.01, 1.04, 1.11, and 1.03 were reported for An-CTF-10-400, An-CTF-20-400, An-CTF-10-500, and An-CTF-20-500, respectively (Fig. 22). These values suggest that An-CTF-10-400, An-CTF-20-400, and An-CTF-20-500 have higher degrees of graphitization, thereby providing an indirect indication that these materials contained fewer defects and more condensed aromatic structures than An-CTF-10-500 [9].

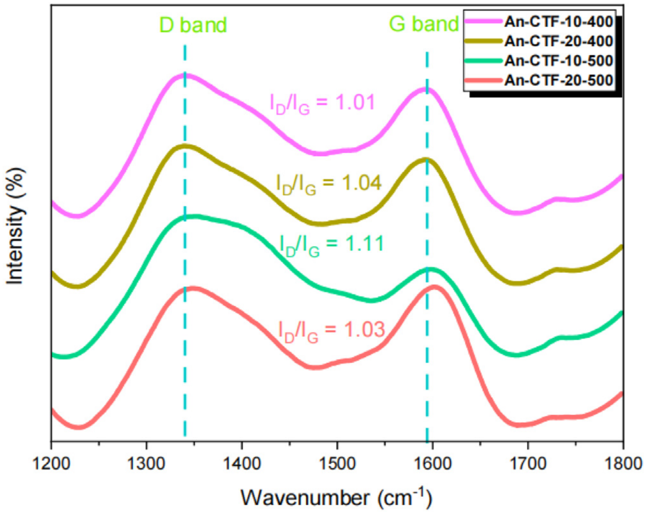

Fig. 22. Raman spectra of An-CTF-10-400, An-CTF-20-400, An-CTF-10-500, and An-CTF-20-500. Adapted from [9] under a Creative Commons license (CC BY 4.0).

4.2. Nuclear magnetic resonance (NMR) spectroscopy

Along with other spectroscopic techniques, NMR has frequently been employed to analyze the structures of COFs [126]. For instance, the fabrication of a CTF-0 via the trimerization of 1,3,5-tricyanobenzene was established using ^{13}C cross-polarization magic-angle spinning (CP/MAS) solid-state NMR. Peaks attributed to the three sp^2 carbons of CTF-0 were recorded at 167×10^{-6}, 136×10^{-6}, and 114×10^{-6} [127]. However, no peak corresponding to residual cyano groups was detected at 110×10^{-6}. Furthermore, a characteristic triazine moiety peak at 121×10^{-6} was observed using ^{15}N solid-state NMR spectroscopy, which confirmed the presence of N in the form of triazine rings in CTF-0 [127].

NMR spectroscopy was also employed to characterize TTF-COF, a COF bonds fabricated using tetrathiafulvalene-tetrabenzaldehyde (TTF) and *p*-phenylenediamine with –C=N– bonds. The ^{13}C CP/MAS NMR spectrum revealed a resonance at 157×10^{-6} corresponding to the carbon of the –C=N– with total suppression of the sideband [126,128].

Solid-state ^{13}C CP/MAS NMR spectroscopy was also employed to characterize COF-ETTA-2,3-Dha. The peak at 159.8×10^{-6} confirmed the presence of imine linkages in COF-ETTA-2,3-Dha, consistent with the FTIR analysis [17]. ^{1}H and ^{13}C NMR spectroscopy were employed to analyze the structure of COF-TpPa-1. The ^{1}H NMR spectrum exhibited a strong peak at approximately 5×10^{-6}, which was assigned to the presence of water molecules in COF-TpPa-1. In addition, the signal at approximately 8.0×10^{-6} was attributed to the protons of amino groups, which suggested the formation of strong intramolecular hydrogen bonds between amino groups and adjacent carbonyls as well as shielding by aromatic rings [125,129]. Moreover, the solid-state ^{13}C NMR spectrum of COF-TpPa-1 exhibited peaks at 146×10^{-6} and 181×10^{-6}, which were attributed to an enamine carbon (=CNH–) and carbonyl carbon (–C=O), respectively. In addition, a small peak at approximately 191×10^{-6} was ascribed to the carbon atom of the aldehyde group in the structural network of COF-TpPa-1 [125,130].

Furthermore, NMR spectroscopy was used to study the occurrence of defects in LZU-111 and COF-300 crystals of different size, as shown in Figs. 23(a)(b). Signals corresponding to terminal groups, such as aldehyde groups, indicate the occurrence of few defects in the synthesized COF-300 crystals [129]. Notably, the number of ^{13}C CP/MAS signals for the 1 and 30 μm COF-300 crystals is significantly higher than that for the 500 nm crystals (Fig. 23(b)), suggesting that the large single crystals of flexible COF-300 show greater structural anisotropy than those of rigid LZU-111. These results reveal the significance of NMR spectroscopy in determining the occurrence of crystal size effects during the size-controlled synthesis of COFs [129].

4.3. X-ray photoelectron spectroscopy (XPS)

XPS has been widely utilized to investigate the linkages between monomeric units in COFs. The XPS spectra of 2D COFs fabricated via the Schiff base reaction of benzene-1,3,5-tricarbaldehyde with DAAQ moieties was used to support the FTIR analysis. The N 1s spectra revealed characteristic peaks at 400.22 eV for the DAAQ monomer and at 399.34 and 400.22 eV for the COF$_{\text{DAAQ-BTA-3DG}}$ composite [126,130,131]. The peaks at 399.34 and 400.22 eV were assigned to N in imine bonds and NH$_2$ in the monomer, respectively. The area of the peak at 400.22 eV

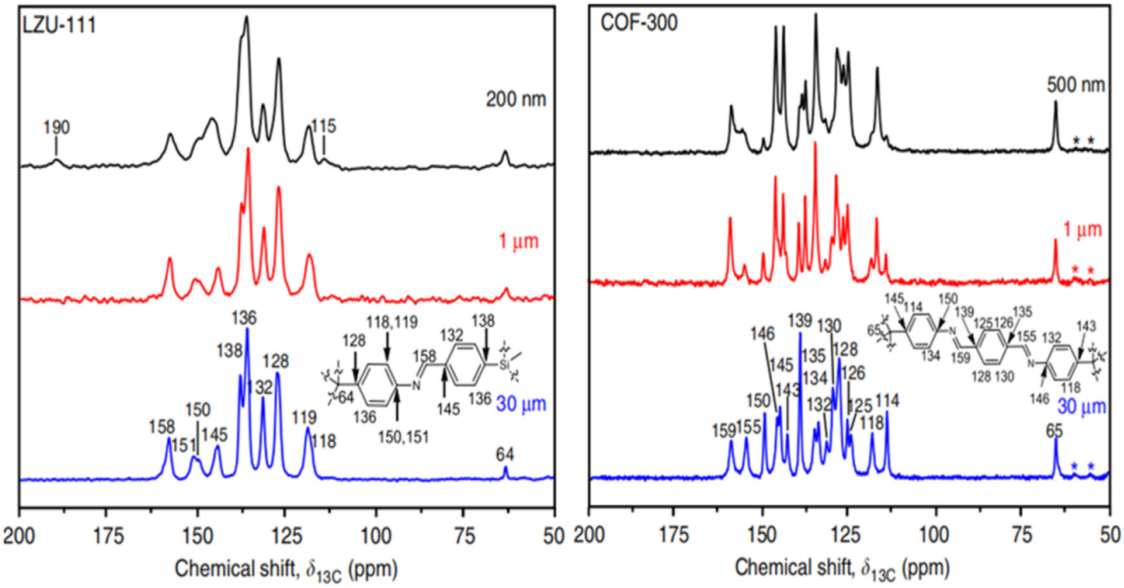

(a) ^{13}C CP/MAS spectra of different-sized LZU-111 (b) ^{13}C CP/MAS spectra of different-sized COF-300

Fig. 23. ^{13}C CP/MAS spectra of (a) LZU-111 and (b) COF-300 crystals of different sizes. The characteristic ^{13}C chemical shifts are assigned on the chemical structures. In (b), the asterisks indicate spinning sidebands. Adapted from [129] under a Creative Commons license (CC BY 4.0).

was approximately one-third that of the peak at 399.34 eV, suggesting that approximately one-fourth of the DAAQ monomers were unreacted, consistent with the FTIR results [126,131].

XPS has also been applied to investigate the functional modification of COFs. For instance, XPS was used to verify the formation of a benzimidazole-functionalized COF (COF-HBI), synthesized by modifying COF-COOH with 2-(2,4-dihydroxyphenyl)-benzimidazole (HBI) [132]. In the N 1s spectrum of COF-HBI, the peak at 399.8 eV was assigned to –NH– of amides, whereas the peaks at 400.6 and 399.1 eV were ascribed to C–N and C–NH–C of imidazole groups. These new peaks demonstrated the successful grafting of HBI to the COF matrix [126,132].

Many other COFs, such as a stereoscopic 2D super-microporous phosphazene-based COF for the environmental remediation of uranium pollutants, have also been characterized using XPS. This technique was used to confirm the removal of uranium from environmental samples using the characteristic peak of U_{4f}. A comparison of the high-resolution U_{4f} spectra of the super-microporous phosphazene-based COF before and after uranium adsorption (MPCOF and MPCOF-U, respectively) revealed the adsorption of uranium in the pores of MPCOF [75,126].

XPS analysis of the COF-DANC-A composite, revealed a slight decrease in the N 1s peak upon the introduction of DANC into the structural network of COF-TpPa-1 [125]. The C/N ratio was lower in TpPa-1 (8.66) than in COF-DANC-A (9.54), thereby verifying the presence of DANC in the COF-DANC-A composite [125,133].

XPS was also employed to characterize An-CTFs (Fig. 24). As shown in Figs. 24(a)–(d), all the synthesized An-CTFs exhibit three peaks at 398.5, 400.0, and 401.5 eV corresponding to different N species (hexagonal pyridinic N atoms in thee triazine unit, pyrrolic species, and quaternary N species, respectively) [9]. In addition, the pyrrolic N peak has a higher intensity than both the pyridinic and quaternary N peaks, which have similar intensities. Furthermore, the three O 1s peaks at 531.5, 533.0, and 535.0 eV (Figs. 24(e)–(h)) are assigned to C–O, moisture, and absorbed oxygen, respectively [9].

4.4. X-ray diffraction (XRD)

Powder X-ray diffraction (PXRD) is suitable for determining the crystalline nature of COFs. PXRD analysis suggested that COF-ETTA-2,3-Dha exhibited durable dual-pore (DP) and single-pore (SP) COF structures, with a strong peak corresponding to the (100) diffraction observed at $2\theta = 2.66^\circ$ [134]. Similarly, PXRD revealed the well-regulated fabrication of TpBD@SiO_2 microspheres based on the peak intensities of TpBD@SiO_2-0.10, TpBD@SiO_2-0.30, and TpBD@SiO_2-0.50 [39,40,41]. XRD analysis of TpPa-1COF showed a slight decrease in the peaks attributed to π–π stacking, which indicated the integration of the Pd NPs into the interlayer space and interior of the COF pores [39,50,51].

Furthermore, hybrid membranes were fabricated by varying the content of a COF in a polymer (PBI-BuI) using DMAc as a solvent to prepare highly flexible COFs (TaPa-1(*n*)@PBI0-BuI and TpBD(*n*)@PBI-BuI, where $n = 20$ wt.%, 40 wt.%, or 50 wt.% TpPa-1 or TpBD). A wide-angle XRD technique was employed to determine the crystalline nature of both TpPa-1(*n*)@PBI-BuI and TpBD(*n*)@PBI-BuI [39,66]. Similarly, films based on a COF with a dual-pore structure were synthesized and characterized using XRD. ETTA and [1,1′-biphenyl]-4,4′-dicarbaldehyde (BPDA) as monomers were dispersed in a homogenous solution of *N*,*N*-dimethylformamide (DMF) with PAN to obtain PAN@COF nanofiber films with different COF loading ratios [134]. XRD characterization revealed that the COF crystals remained intact in the obtained PAN@COF nanofiber films and that these films maintained the characteristic dual-pore structure of the COFs while also exhibiting good stability and excellent reusability for the removal of phytochromes from vegetable extracts [39,134].

A comparison of the XRD patterns of TpPa-1 and TpPa-1-DANC revealed a characteristic peak corresponding to the (110) crystal plane of cellulose at approximately 22°, which verified the incorporation of DANC into TpPa-1 to yield the TpPa-1-DANC composite. Further, a decrease in the peak at $2\theta = 27.22^\circ$ was attributed to the COF grown on the (001) crystal plane being parallel to the direction of cellulose [125,135].

Further, XRD analysis has been reported for the An-CTFs materials. The two broad peaks at 12 and 26° in the XRD pattern of An-CTFs (Fig. 25) are assigned to the (001) and (100) plane indices, respectively, suggesting the formation of a partially crystalline structure [9].

4.5. Scanning electron microscopy (SEM) and transmission emission microscopy (TEM)

The morphologies of COFs have been evaluated using SEM and TEM. For example, SEM and TEM analysis of COF-ETTA-2,3-Dha revealed a large number of hollow and spherical structures with a 2 μm

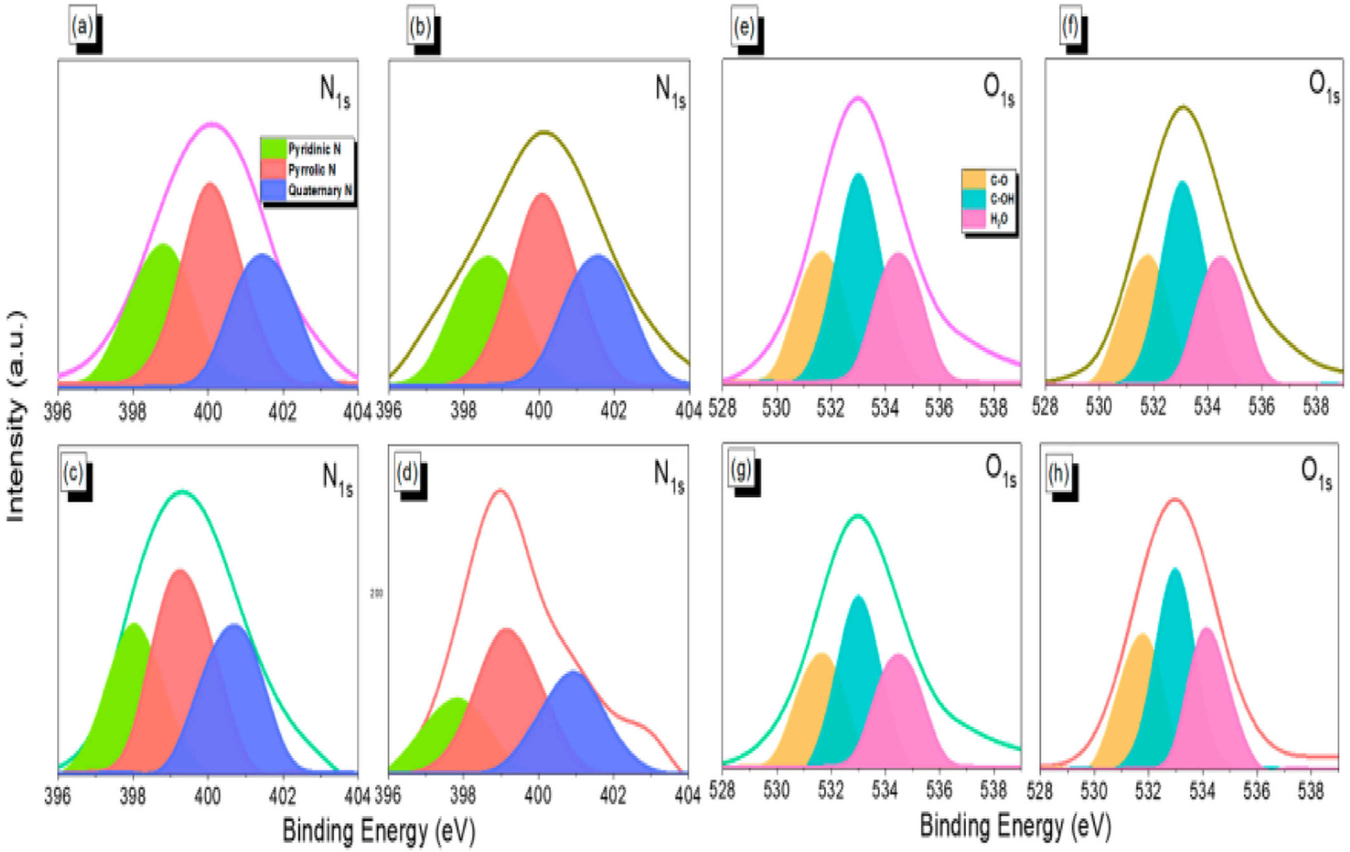

Fig. 24. Fitted XPS (a)–(d) N 1s and (e)–(h) O 2s spectra for An-CTF-10-400, An-CTF-20-400, An-CTF-10-500, and An-CTF-20-500. Adapted from [9] under a Creative Commons license (CC BY 4.0).

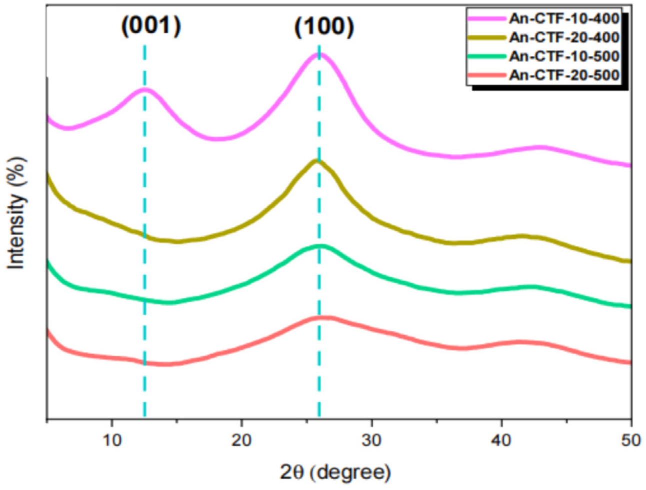

Fig. 25. XRD patterns of An-CTF-10-400, An-CTF-20-400, An-CTF-10-500, and An-CTF-20-500. Adapted from [9] under a Creative Commons license (CC BY 4.0).

diameter [17]. SEM was used to characterize an imine-linked COF-LZU1 membrane grown on alumina tubes. The dark-yellow tubes consisted of intergrown grains with sizes in the range of 100–300 nm. This continuous layer was devoid of visible pinholes or cracks. Furthermore, cross-sectional SEM analysis revealed that the as-fabricated COF-LZU1 layer had a thickness of approximately 400 nm [39,46].

TEM analysis of COF-(TpBD)/Fe_3O_4 revealed that spherical Fe_3O_4 NPs with a size distribution of < 50 nm were reportedly embedded in the TpBD nanosheet [39,136]. A COF-decorated graphene/magnetite composite (MagG@COF-5) was also characterized using TEM. The graphene nanosheets were found to become thicker after coating with COFs and the magnetic NPs incorporated in MagG@COF-5 were completely covered, thereby confirming that the magnetic graphene (MagG) were successfully coated with COF-5 [39,62].

In addition, TEM analysis revealed the uniform distribution of Au NPs (5 ± 3 nm) throughout the framework of TpPa-1COF. When $Pd(OAc)_2$ was used as a precursor, Pd NPs (7 ± 3 nm) were homogeneously distributed in TpPa-1COF [39,50,51]. Similarly, field emission SEM (FESEM) has been employed to characterize COFs. For example, this technique was used to reveal the successful formation of crystalline and spherical Fe_3O_4@c-1 NPs [39,137]

Comparative SEM analysis was used to study the morphologies and PSDs of LZU-111 and COF-300. In particular, SEM analysis was used to reveal the crystal-size effect. When directly mixing the building units without a modulator, 200 nm LZU-111 crystals were obtained. Furthermore, when a variable-temperature heating approach was used to accelerate crystal growth, 30 μm LZU-111 crystals were obtained within 10 days as shown in Figs. 26(a)–(c). This approach also allowed the synthesis of COF-300 crystals with sizes of 500 nm, ~1 μm, and ~30 μm, as shown in Figs. 26(d)–(f) [32].

Combined SEM and HR-TEM analyses were used to characterize the An-CTFs. SEM images show that the An-CTFs consist of regular and uniform spherical particles with small nanorods (Figs. 27(a)–(d)). Furthermore, the HR-TEM images reveal the presence of irregular microporous networks in the An-CTFs, as shown in Figs. 27(e)–(h) [9].

The morphology of a COF-functionalized poly(styrene-divinyl benzene-glycidylmethacrylate) composite (COF@PS-GMA), fabricated by growing of a COF on the surface of PS-GMA particles, was investigated using SEM. The PS-GMA particles exhibited a porous

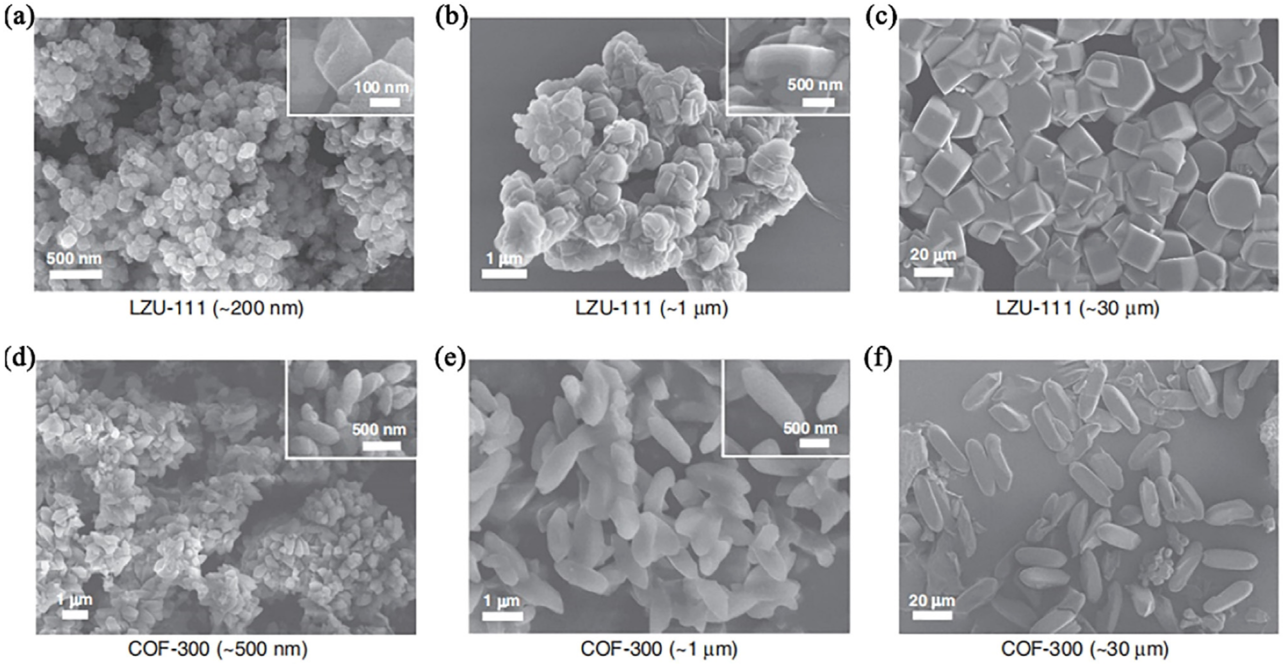

Fig. 26. (a)–(c): SEM images of LZU-111 crystals with average sizes of ~200 nm, ~1 µm, and ~30 µm; (d)–(f): SEM images of COF-300 crystals with average sizes of ~500 nm, ~1 µm, and ~30 µm. Adapted from [32] under a Creative Commons license (CC BY 4.0).

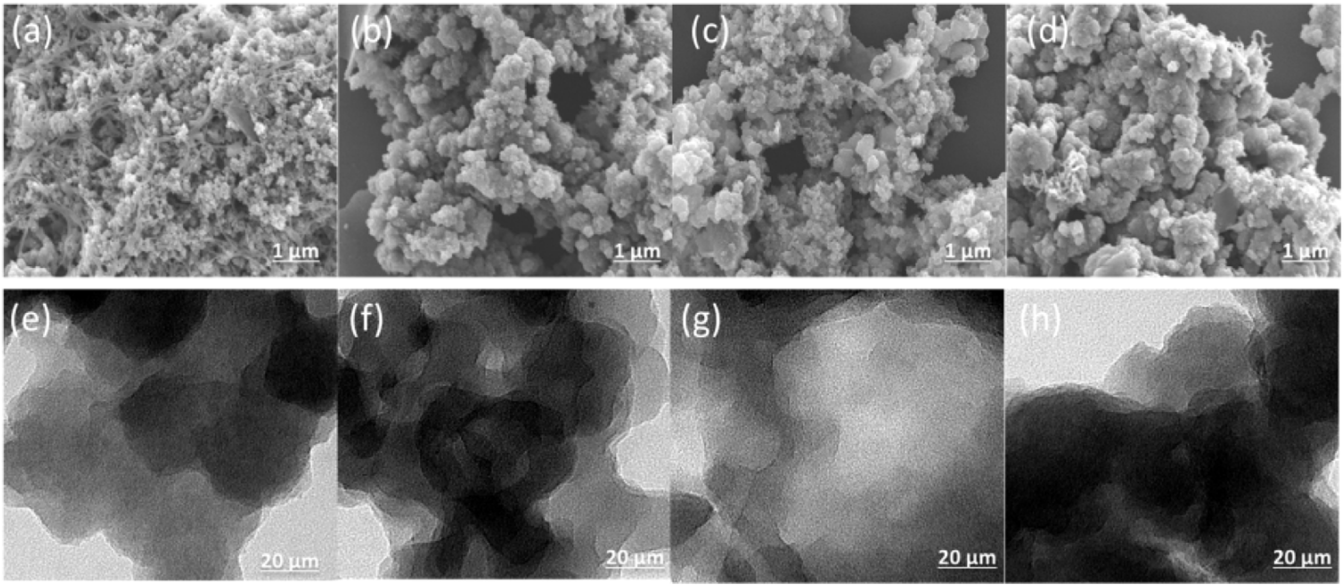

Fig. 27. SEM and TEM images of the An-CTFs: (a) and (e) An-CTF-10-400, (b) and (f): An-CTF-20-400, (c) and (g) An-CTF-10-500, and (d) and (h) An-CTF-20-500. Adapted from [9] under a Creative Commons license (CC BY 4.0).

spherical structure with a size of approximately 6 µm, whereas the COF@PS-GMA particles were characterized by smooth surfaces [39,138]. FESEM and high-resolution TEM (HR-TEM) were used to characterize the surface structures of the sp^2-carbon-conjugated COFs (sp^2c-COF, sp^2c-COF-2, and sp^2c-COF-3) with different π-lattices. The FESEM and HR-TEM results revealed that these COFs had relatively similar morphologies with belt shapes and tetragonal layered structures [110].

4.6. Brunauer–Emmett–Teller (BET) analysis

BET analysis can be used to determine the surface areas of COFs. For COF-ETTA-2,3-Dha, BET analysis of the isotherm data at $P/P_0 = 0.05$–0.3 gave a value a surface area of 1476.5 m^2 g^{-1} with a total pore volume of 0.91 cm^3 g^{-1} at $P/P_0 = 0.99$ [17]. N_2 adsorption–desorption isotherms were also employed to determine the BET surface area of COF-ETTA-2,3-Dha after its application for Cd removal from water. After Cd adsorption, the surface area of COF-ETTA-2,3-Dha was 783.6 m^2 g^{-1}, which is approximately half of that of the pristine COF, and the pore volume decreased significantly from 0.91 to 0.40 cm^3 g^{-1} at $P/P_0 = 0.99$ [17].

BET analysis gave surface areas of 538 and 1346 m^2 g^{-1} for TpBD-Me_2 and Fe_3O_4@COF (TpBD), respectively. In addition, surface areas of 431 and 1033 m^2 g^{-1} were obtained for COF-300@SiO_2 and pristine COF-300, respectively [39,41]. In another study, the BET surface area of MagG@COF-5 was found to be 201 m^2 g^{-1}, whereas the magnetic

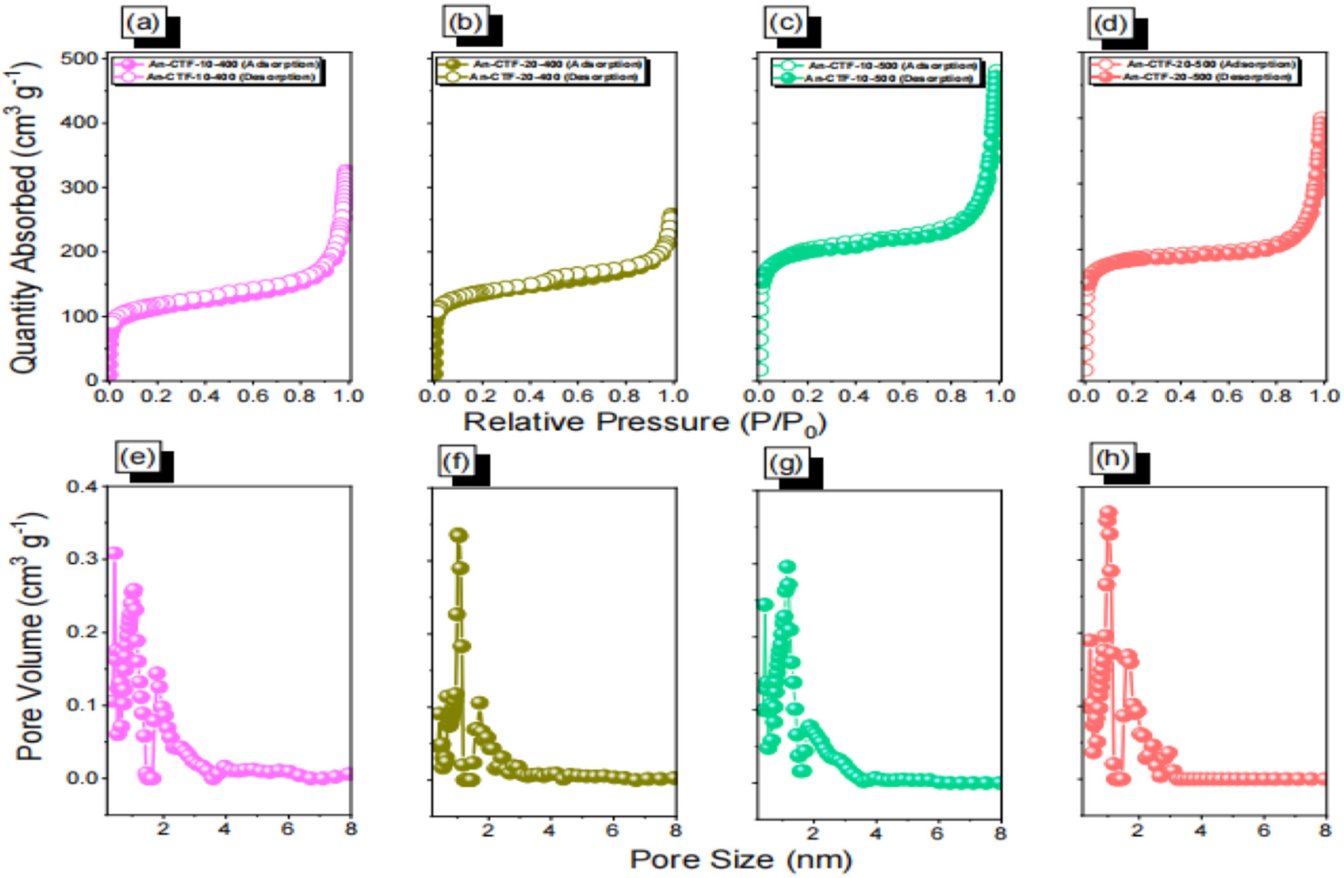

Fig. 28. N_2 adsorption–desorption isotherms and PSDs of (a)(e) An-CTF-10-400, (b)(f) An-CTF-20-400, (c)(g) An-CTF-10-500, and (d)(h) An-CTF-20-500. Adapted from [9] under a Creative Commons license (CC BY 4.0).

graphene sheet exhibited a surface area of 65 m^2 g^{-1} [62]. Furthermore, the successful immobilization of Au NPs through electrostatic interaction with the unsaturated amino on the TAPB-DMTP COF was experimentally demonstrated [39]. Significantly, the COF-derived composite of TAPB-DMTP retained the crystalline nature of the COF with a surface area of approximately 1915 m^2 g^{-1}. However, the surface area of the composite was smaller than that of the bulk COF (2385.65 m^2 g^{-1}) owing to the effect of growing Au NPs within the COF pores. This behavior demonstrates the difficulty in controlling the rapid growth of NPs during the synthesis of COF-metal based composites [39,52,139,140].

The surface area of COF@PS-GMA, fabricated by growing of a COF on the surface of PS-GMA, was also evaluated using BET analysis [39,138]. Notably, the surface area increased significantly from 201 to 404 m^2 g^{-1} after COF growth on the PS-GMA particles. This large increase in surface area was attributed to the successful synthesis of COF@PS-GMA particles [39,138]. Furthermore, BET analysis was used to determine the surface areas of three new β-ketoenamine-linked COFs fabricated via Schiff base [3 + 3] polycondensation of 1,3,5-triformylphloroglucinol (TFP-3OHCHO) with tris(aminophenyl) derivatives with carbazole, amino, or pyridine units under solvothermal conditions. The resulting TFP-COFs exhibited high BET specific surface areas of up to 686 m^2 g^{-1} and excellent crystallinity [74].

BET analysis has also been used to examine the surface area and porosity of the An-CTF materials. As shown by the N_2 adsorption–desorption isotherms of An-CTFs at 77 K (Figs. 28(a)–(d)), these materials all exhibit type IV isotherms with high BET surface areas of 406, 491, 751, and 700 m^2 g^{-1} for An-CTF-10-400, An-CTF-20-400, An-CTF-10-500, and An-CTF-20-500, respectively (9). The corresponding PSDs of the An-CTFs are shown in Figs. 28(e)–(h). The surface area decreased in the order An-CTF-10-500 > An-CTF-20-500 > An-CTF-20-400 > An-CTF-10-400, indicating a correlation with the availability of tightly packed NPs with large defects for ion conduction [9].

4.7. *Thermogravimetric analysis (TGA)*

TGA allows determination of the thermal stability of a substance in response to heat. Recently, TGA has been employed to study the thermal stability of COFs. For instance, TGA revealed the excellent thermal stability of COF-ETTA-2,3-Dha, as indicated by a small weight loss of approximately 6% upon increasing the temperature from ambient condition to 350 °C [17]. Furthermore, TGA of COF-TpPa-1 gave pyrolysis temperatures of approximately 330 and 444 °C with approximately 40% pyrolysis residue as shown in Fig. 29(a). Moreover, the temperature of the highest decomposition rate decreased when the DANC dosage incorporated in COF-TpPa-1 increased, as shown in Fig. 29(a) [125,138,140,141]. A comparison of the TpPa-1-DANC composites revealed that the first pyrolysis peak of TpPa-1-DANC had a larger area than that of the COF-TpPa-1, thereby evidencing the increased carbon content resulting from the incorporation of DANC into COF-TpPa-1. Thus, the TpPa-1-DANC composite with the highest COF content achieved the highest thermal stability [125].

In addition, increasing the COF content resulted in a corresponding increase in the ash component of the composites. This change was attributed to the aromatization of COF residues during carbonization. Consequently, in COF-DANC composites with smaller COF contents, the amount of residue was reduced owing to the decrease in aromatics [125].

FTIR spectroscopy coupled with TGA has been employed to characterize COFs. As shown in Figs. 29(b)–(d), the FTIR spectra and TGA curves of COF-TpPa-1 were obtained at different temperatures (100, 300, and 400 °C) at a heating rate of 15 °C min^{-1} [125]. At 100 °C, a

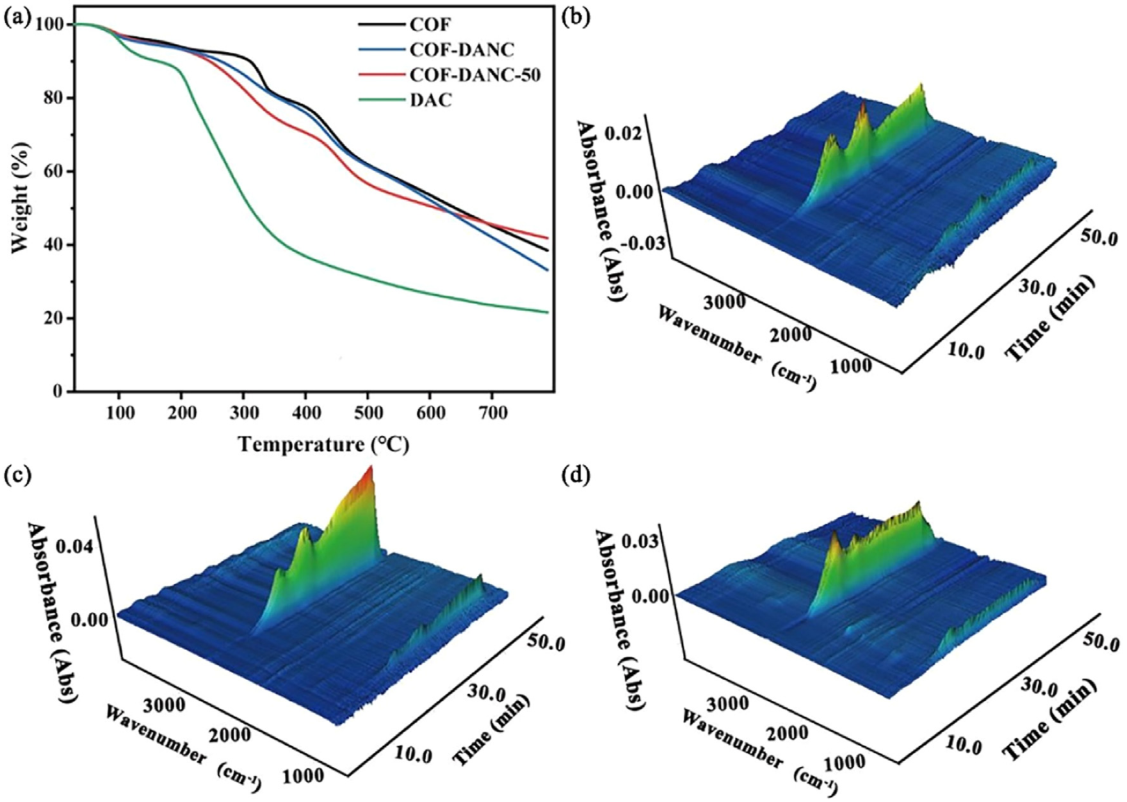

Fig. 29. (a) TGA curves of various materials; thermogravimetric-infrared 3D diagrams of (b) COF-TpPa-1, (c) the TpPa-DANC-50 composite, (d) and COF. Adapted from [125] under a Creative Commons license (CC BY 4.0).

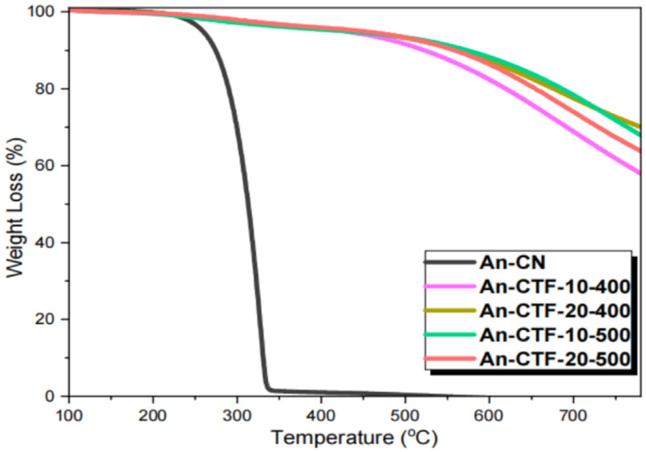

Fig. 30. TGA curves of An-CN, An-CTF-10-400, An-CTF-20-400, An-CTF-10-500, and An-CTF-20-500. Adapted from [9] under a Creative Commons license (CC BY 4.0).

slight weight loss occurs and an FTIR peak appears at 3400–3700 cm^{-1}, which is related to the surface of COF-TpPa-1. At 300 °C, an FTIR peak appears at 1380 cm^{-1}, which corresponds to the absorbance of some CO_2 as well as C–C bonds in the skeleton of COF-TpPa-1. Furthermore, at 400 °C, the intensity of the FTIR peak at 2300 cm^{-1} increases, which suggests the large-scale cracking and decomposition of the COF-TpPa-1 framework [125].

To obtain insight into the thermal stability of An-CN and the corresponding An-CTF materials, TGA was performed under a N_2 atmosphere in the temperature range of 100–800 °C (Fig. 30). An-CTF-10-500 exhibits the highest decomposition temperature of 573 °C. Moreover, the char yield of An-CTF-10-500 (66 wt.%) is higher than those of other An-CTFs (56 wt.%, 69 wt.%, and 62 wt.% for An-CTF-10-400, An-CTF-20-400, and An-CTF-20-500, respectively). Thus, it was suggested that An-CTF-10-500 has the highest thermal stability among the An-CTFs [9].

4.8. Chemical stability

The chemical stability of a chemical compound is a crucial criterion for evaluating durability, reactivity, and potential applications. Therefore, the chemical stability of COF-based compounds should be probed in both organic and aqueous solvents such as water, acidic, and basic solutions. For instance, the chemical stability of COF-ETTA-2,3-Dha in aqueous solution was determined under neutral, acidic, and basic conditions. Specifically, dispersions of COF-ETTA-2,3-Dha were placed in 3 M HCl, 3 M NaOH, or water at a 25 °C for 12 h [17]. Subsequently, the samples were collected by filtration, washed thoroughly using distilled/deionized water, and dried under vacuum at 120 °C for 3 h before PXRD analysis. No obvious differences were observed between the PXRD pattern of the pristine COF and those of the COF-ETTA-2,3-Dha samples subjected to neutral, acidic, and basic conditions indicating COF-ETTA-2,3-Dha exhibited excellent resistance to water, acids, and bases [17]. The high chemical stability of COF-ETTA-2,3-Dha against hydrolysis could be attributable to the presence of intramolecular hydrogen-bonding interactions within the structural framework. These interactions could enhance the stability of COF-ETTA-2,3-Dha by suppressing the torsion of the edge units, thereby establishing a planar structure in the COF layers [17]. Furthermore, the chemical stabilities of the sp^2-carbon-conjugated frameworks sp^{2}c-COF, sp^{2}c-COF-2, and sp^{2}c-COF-3 were evaluated via immersion in various solvents, including DMF, tetrahydrofuran (THF), 12 M HCl, methanol, water, and 14 M NaOH, for 1 week [87]. Notably, these COFs retained their initial PXRD patterns. In addition, no significant weight loss occurred in organic solvents or water, but up to 90% residual weight loss occurred in the strongly acidic and basic media. The corresponding FTIR spectra revealed that the chemical structures of the sp^2-carbon-coordinated COFs were sustained after immersion various solvents, verifying the chemical stability of these materials [110].

4.9. PSD analysis

The PSD of a chemical compound often plays a critical role in determining its potential applications. The PSD of COF-ETTA-2,3-Dha, as estimated using nonlocal density functional theory, revealed two main components at approximately 6.3 and 24.5 Å. These values were similar to the theoretical values derived from the simulated crystal structure (5.9 and 26.3 Å for triangular and hexagonal mesopores, respectively) [17]. Moreover, when COF-ETTA-2,3-Dha was applied for Cd removal from wastewater, the PSD of COF-ETTA-2,3-Dha-Cd exhibited two major components centered at 6.5 and 21.6 Å. A comparison with the pristine COF revealed that the adsorption uptake of Cd(II) had no significant effect on the size of the micropores, whereas the diameter of the mesopores decreased, indicating that the Cd(II) ions were trapped in the mesoporous channels of COF-ETTA-2,3-Dha [17].

For TpBpy-COF, which was fabricated using a $PdCl_2$-prefunctionalized Bpy building block that promoted the rapid growth of Pd NPs, the PSD revealed pore sizes in an increased range of 1.4 to 2.3 nm, corresponding to the characteristic pore size of TpBpy and TpBpy-COF with incorporated Pd NPs. This denotes the partial blocking of the characteristic pores of the fabricated TpBpy-COF by the Pd NPs [39,54]. In addition, the size of the Pd NPs (12 ± 4 nm) was larger than the characteristic pore size of TpBpy-COF. This difference indicated that the Pd NPs grew rapidly in the spaces between the layers and surface of TpBpy-COF, resulting in a composite with homogeneously distributed Pd NPs [39,54].

5. Applications of COFs

5.1. Gas storage

Catastrophic global climate change resulting from greenhouse gases such as atmospheric CO_2 and methane that cause global warming is a major concern. To address this issue, the CO_2 capture and storage abilities of porous materials, including ZIFs, MOFs, and COFs, have been explored. Recently, TPT and triphenylamine (TPA)-based COFs has been fabricated via the polycondensation of 2,4,6-tris(4-aminophenyl)triazine or tris(4-aminophenyl)amine, respectively, with triarylaldehydes with diverse symmetries, planarities, and N-atom contents. The surface area and crystallinity degree of the resulting COFs were dependent on the planarity and symmetry of the monomers [1,141]. CO_2 capture and storage can be promoted by enhancing the interactions between COFs and CO_2 by incorporating triaryltriazine units with higher N-atom contents and greater planarity into the backbones of TPA-COFs or the TPT-COFs [142]. Notably, TFP-COFs fabricated from β-ketoenamine-linked COFs were found to achieve CO_2 uptake efficiencies of 200 mg g^{-1} at 273 K [74].

In addition, numerous 3D COFs with diverse structures have been developed for the separation and adsorption of CO_2. For example, 3D COF-103 and a COF-102 featured high surface area of 3530 and 3620 m^2 g^{-1}, respectively, with outstanding CO_2 adsorption capacities of 1190 and 1200 mg g^{-1}, respectively, at 50 bar and 298 K [1,143]. Further investigations revealed that COFs can be classified into three groups based on their pore sizes and structural dimensions, with group 1 consisting of 2D structures with small 1D pores, group 2 consisting of 2D structures with large 1D pores, and group 3 consisting of 3D structures with moderately sized 3D pores. Notably, COFs in group 3, such as COF-102, outperform those in groups 1 and 2 as well as MOFs and other porous materials for the adsorption and storage of gases including hydrogen, methane, and CO_2, achieving adsorption capacities of 72 mg g^{-1} at 77 K, 187 mg g^{-1} at 298 K, and 1180 mg g^{-1} at 298 K, respectively [143].

The utilization of An-COFs for the capture and storage of CO_2 was investigated using CO_2 adsorption isotherm at 273 and 298 K (Figs. 31(a)(b)). At room temperature (298 K), An-CTF-10-400, An-CTF-20-400, An-CTF-10-500, and An-CTF-20-500 exhibit CO_2 capture capacities of 2.00, 2.13, 2.63, and 2.69 mmol g^{-1}, respectively. However, at a lower temperature of 273 K, the CO_2 capture capacities increase to 3.96, 4.22, 5.22, and 5.25 mmol g^{-1}, respectively. As An-CTF-10-500 has a higher CO_2 capture capacity than the other An-CTF materials, it is a good candidate for CO_2 uptake storage [9].

5.2. Catalysis

Functional porous materials have been widely utilized for heterogeneous catalysis owing to their high surface areas. COFs have emerged as ideal candidates with high selectivity, efficiency, and robustness for catalytic application because they frequently contain catalytic sites and exhibit high thermal and chemical stabilities in both water and organic solvents [39,144]. Imine-linked COF-LZU1, prepared via the Schiff base reaction of 1,3,5-triformylbenzene and 1,4-diaminobenzene, has been reported to form strong coordinate bonds with metal ions. Post-synthetic treatment of COF-LZU1 with $Pd(OAc)_2$ under ambient conditions produced a Pd/COF-LZU1 composite, which acted as an efficient catalyst for Suzuki–Miyaura coupling reactions with a wide range of reactants. Compared with Pd-containing MOFs, Pd/COF-LZU1 gave relatively high product yields of 96%–98% in a short reaction time, exhibited high stability, and could be easily recycled [39,82].

Hybrid catalysts consisting of COFs with metals NPs, including Pt, Au, Ag, and Pd, have been fabricated for the catalytic degradation of organic compounds. For example, an Ag NPs/TPHH COF composite at a minimum dose of 3 mg was employed for the catalytic degradation of a 4-nitrophenol (4-NPh) to a 4-aminophenol (4-AP) [50,52,145]. The catalytic performance was verified experimentally based on the decrease in the absorption peak at 400 nm, corresponding to 4-NPh, and the increase in the absorption peak at 300 nm, corresponding to 4-AP. Similar findings were obtained when the Ag NPs/TPHH COF was applied for the catalytic reduction of other nitroaromatic compounds, including 4-nitroaniline, 4-nitrobenzene, 4-nitrotoluene, 2-nitrophenol, and 1-butoxy-4-nitrobenzene. Thus, the Ag NPs/TPHH COF composite achieved efficient catalytic hydrogenation of –N=N– or –C=N– moieties and degradation of conjugated structures in organic compounds [39,145].

COF-based hybrids have recently been employed for the photocatalytic generation/evolution of hydrogen as a clean fuel from water, offering a promising and sustainable approach for converting solar energy (renewable sunlight) into chemical energy. The combination of highly ordered crystalline COFs with noble metal NPs (or less expensive non-noble metal alternative such as MoS_2) as a co-catalyst can reduce the recombination rates of photogenerated charge carriers [146,147]. A MoS_2/TpPa-1 COF composite was fabricated using an exfoliated MoS_2 dispersion in DMF for the in-situ growth of TpPa-1-COF. This composite acted as a photocatalyst with an optical absorption intensity in the range of 200–800 nm that exceeded those of the individual components [146]. In addition, the calculated valence and conduction bands of MoS_2/TpPa-1 COF were more positive than the O_2/H_2O potential and more negative than the H^+/H_2 potential, respectively, confirming the water splitting ability of this composite material [146,147]. Furthermore, the MoS_2/TpPa-1 COF composite with an optimum MoS_2 loading of 3 wt.% exhibited a hydrogen evolution rate of 55.85 μmol h^{-1} under visible-light irradiation with an apparent quantum efficiency of 0.76% at 420 nm and outstanding stability over five cycles without any decrease in photocatalytic performance. In addition, the MoS_2/TpPa-1 COF composite exhibited better catalytic performance than TpPa-1-COF and Pt/TpPa-1-COF, which achieved hydrogen evolution rates of 1.72 and 54.79 μmol h^{-1}, respectively [146,147].

Owing to its size-dependent electronic properties and suitable band gap of 2.4 eV, CdS is an ideal semiconductor photocatalyst for efficient solar light harvesting. Using a combined impregnation and photodepo-

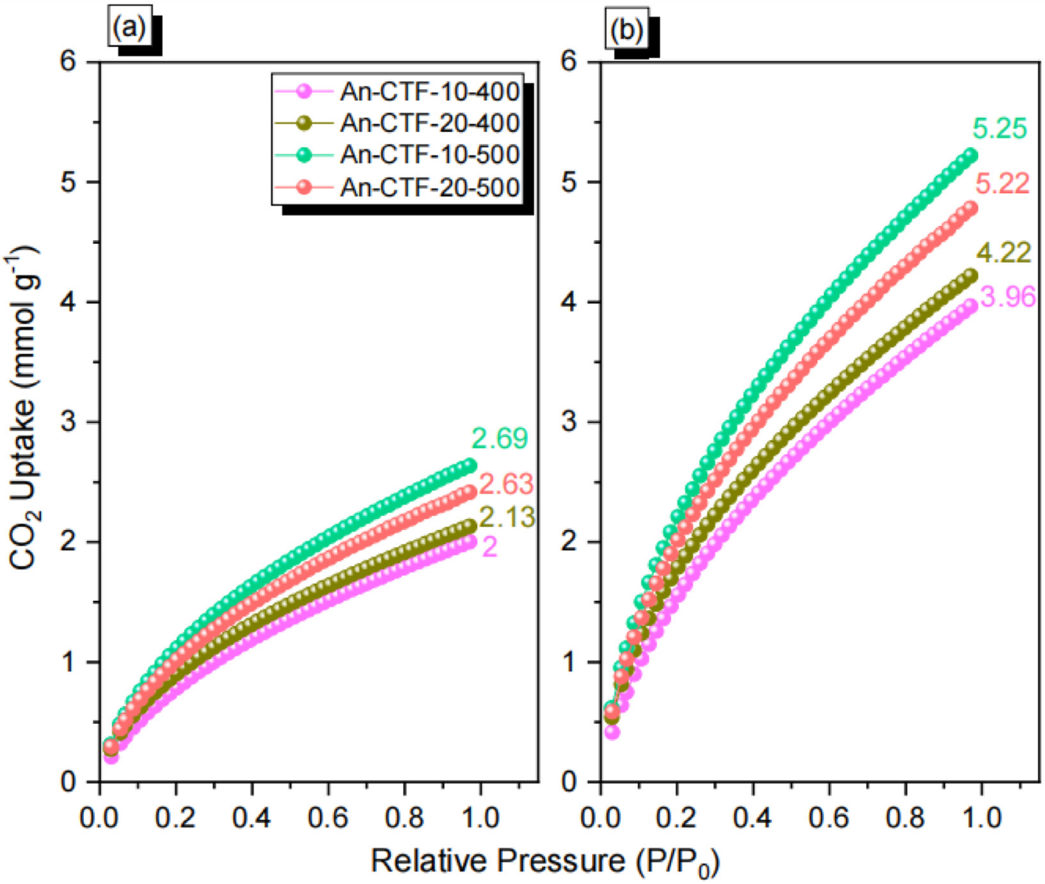

Fig. 31. CO_2 adsorption performance of An-CTF-10-400, An-CTF-20-400, An-CTF-10-50, and An-CTF-20-500 at (a) 298 K and (b) 273 K. Adapted from [9] under a Creative Commons license (CC BY 4.0).

sition method, CdS NPs were incorporated into a CTF to fabricate CdS-CTF-1. The photocatalytic performance of the CdS-CTF-1 composite exhibited superior catalytic performance at an optimum CdS loading of 20% CdS. Charge carriers formed by CTF-1 and CdS under visible-light irradiation promoted the catalytic reduction of water to H_2. Electrons were transferred from CTF-1 to CdS and holes migrated from CdS to CTF-1, where they were quenched by lactic acid as a sacrificial agent [147,148].

Furthermore, a 2D thioether-functionalized COF (TTR-COF) was prepared via the condensation of 2,5-bis(2-(ethylthio)ethoxy) terephthalohydrazide (BETH) and 1,3,5-tris(4-formylphenyl)triazine (TFPT) under solvothermal conditions. TTR-COF was utilized for photocatalytic hydrogen evolution from seawater, achieving a reaction rate of 141 µmol h^{-1} g^{-1} with stable activity over five cycles, unlike the analogous COF without thioether modification (TFPT-COF). The affinity of Au for thioether was suggested to stabilize the Au NPs in TTR-COF, thus ensuring higher catalytic stability than in TFPT-COF. Moreover, the transport of photogenerated charge carriers to the Au co-catalyst for hydrogen generation from water was likely facilitated by the conjugated framework of TTR-COF [147,149].

CO_2 reduction has been suggested as an important technique to reduce CO_2 emissions and alleviate global warming. Ideal catalysts for CO_2 reduction require a stable chemical structure with a suitable band gap for harvesting of visible light and efficient electron transport. To this end, COFs with strong covalent bonds, highly conjugated structures, and microporous lattices are ideal candidates for CO_2 reduction. A comparative study on catalytic CO_2 reduction using a triazine COF (N3-COF) based on 2,4,6-tris(4-bromophenyl)-1,3,5-triazine and undoped ACOF-1 revealed low CO_2 activities at 80 °C and 4 atm, achieving methanol evolution rates of 8.6 and 13.7 µmol g^{-1} for ACOF-1 and N3-COF, respectively [147,150]. Although N3-COF performed better than ACOF-1, both these materials exhibited lower catalytic activities for CO_2 reduction than other materials based on metal dopants, photosensitizers, and sacrificial electron donors [147,150]. Triazine-based COFs typically exhibit better catalytic CO_2 reduction performance than non-triazine systems owing to their higher affinity for negative charge during electron conduction. Nonetheless, to prevent rapid electron–hole recombination in organic semiconductors and thus increase catalytic efficiency, a photosensitizer is required. Photosensitizers can either be introduced as homogenous co-catalysts or incorporated into the COF network by post-synthetic modification [147,150,151].

Photosensitizers have been introduced into COF structures via the incorporation of metal. For example, in 2D sp^2-carbon Bpy-based COF, the photosensitizer-like complex $Re(bpy)(CO)_2Cl$ was integrated into the COF structure via Bpy nitrogen binding sites. This Re-doped COF attained a CO yield of 1040 µmol g^{-1}, whereas the undoped complex only produced trace CO, thereby demonstrating the ability of the photosensitizer to facilitate electron–hole generation. In addition, the Re-doped COF exhibited an enhanced CO_2 adsorption capacity of 1.7 mmol g^{-1} at 273 K with a heat of adsorption of 31 kJ mol^{-1} [147,152].

The photocurrent responses of COFs can be increased by the inclusion of metal dopants, such as Re, allowing the generation of higher current densities. For instance, in the absence of Re NPs, TpPa-1 exhibited the lowest CO yield of 32.4 µmol g^{-1} h^{-1}, whereas at loading of 1 wt.%, 3 wt.%, and 5 wt.%, the CO yield increased to 41.8, 108.8, and 61.8 µmol g^{-1} h^{-1}, respectively [147,153].

Non-precious metals have also been reported to be effective dopants for catalytic CO_2 reduction. For instance, PI-linked COFs with a $[Ni(bpy)_3]^{2+}$ photosensitizer achieved a high catalytic CO_2 reduction activity of 483 µmol g^{-1} h^{-1}, whereas other investigated COFs only exhibited trace activity [147,154]. Lastly, the electronic environment of certain dopants has been found to play a significant role in product selectivity during photocatalytic CO_2 reduction. For a porphyrinic COF (Co-COF-367), Co^{II}-COF-367 was shown to achieve product yields of 48.6, 16.5, and 12.8 μmol g^{-1} h^{-1} for formic acid, CO, and methane, respectively. In contrast, Co^{III}-COF-367 exhibited yields of 93.0, 0.44, and 10.1 μmol g^{-1} h^{-1}, respectively [147,155].

5.3. Supercapacitors

COFs have been exploited as platforms for electrical double-layer superconductors owing to their high surface areas. The 2D COF (DAAQ-TFP COF) obtained via the condensation of DAAQ as a redox-active unit with TFP-30HCHO under solvothermal conditions can function as an effective pseudocapacitor [156,157]. The high surface area (1280 m^2 g^{-1}) and highly ordered porosity of DAAQ-TFP COF favor charge transfer from the redox-active units in the COF to the surfaces of supercapacitor electrodes [1,156]. Over 5000 charge/discharge cycles, the electrode exhibited a stable capacitance of 40 F g^{-1}. This low capacitance indicated that only 2.5% of the redox-active DAAQ units were electrochemically accessible, likely due to poor electrical contact resulting from the random orientation of the polycrystalline DAAQ-TFP COF. These issues were addressed by preparing an oriented thin film of β-ketoenamine-linked 2D COF, which achieved a 400% increase in electrode capacitance [1,158].

Recently, COFs with various redox-active moieties, such as triaryltriazine, carbazole, amino, and pyridine units, and N-atom-rich groups, such as benzobisoxazole, triazine, and triphenylamine, have been incorporated in supercapacitors. These COFs had desirable electrochemical properties owing to their ordered porosities, high surface areas, and redox-active and N-atom-rich units, making them an ideal platform for supercapacitor [1,159-162]. The An-CTF materials were also examined as supercapacitors using galvanostatic charge–discharge measurements in 1 M KOH solution with a three-electrode setup. Among the An-CTF materials, CTF-10-500 exhibited the highest specific capacitance (589 F g^{-1}) and capacity retention (95% over 5000 cycles), as shown in Fig. 32 [9]. The exceptional performance of CTF-10-500 was attributed to the presence of graphitic microporous carbon structures with diverse functional groups, including pyridinic and pyrrolic N atoms, C=O, and phenolic OH [9]. The exceptional performance of CTF-10-500 was also attributed to increasing the An-CN/$ZnCl_2$ molar ratio from 0.05 to 0.1 at 500 °C, which promoted the formation of a carbon-rich network with a high N content (9). Furthermore, as shown in Fig. 32(a), the capacitance of the An-CTF materials decreases as the current density increases from 0.5 to 20 A g^{-1}. In addition, An-CTF-10-400, An-CTF-20-400, An-CTF-10-500, and An-CTF-20-500 achieve capacitance retention of 56%, 72%, 95%, and 90%, respectively (Fig. 32(b)) [9].

5.4. Water treatment

The scarcity of potable water supplies necessitates the protection of natural freshwater resources [163–168]. Hence, wastewater treatment has received significant research interest, and COFs are considered viable materials for water treatment operations.

5.4.1. Removal of heavy metals

Heavy metals are problematic owing to their adverse effects on living organisms and ecological systems [169–171]. Further, the nonbiodegradable nature of heavy metals necessities the removal of heavy metals and their corresponding complexes from water to prevent health and environmental hazards [172,173].

5.4.1.1. Removal of lead.

Carboxyl groups were introduced into COFs via post-synthetic modification to yield a carboxyl-functionalized COF (COOH@COF) with a Pb adsorption capacity of 123.9 mg g^{-1} and high selectivity for Pb, resulting in 90% removal of Pb from water. As a viable adsorbent for Pb removal, COOH@COF also performed well in regeneration studies, maintain the same adsorption capacity for Pb removal over 20 cycles [174].

Furthermore, COFs were modified with hydroxyl (–OH) and triazine (Tz) bifunctional groups to fabricate COF-Tz-OH. Notably, COF-Tz-OH achieved an adsorption capacity of 476 mg g^{-1} and 99% removal of Pb with a contact time of 5 min. The integration of bifunctional groups into the COF structure created numerous chelating sites in the mesopores of COF-Tz-OH that were favorable for the adsorption of Pb. In addition, COF-Tz-OH maintained a 90% Pb removal efficiency over five cycles [175].

A sulfhydryl-functionalized COF (COF-SH) was also developed for the selective removal of Pb from water. The incorporation of sulfhydryl groups into the COF structure has been suggested to alter the electrostatic surface charge and introduce active sites, thus increasing the adsorption capacity of COF-SH to 239 mg g^{-1} with 90% Pb removal in 48 h [176].

A COF was modified with PVDF to fabricate ultrafiltration membranes with high Pb^{2+} removal capabilities. The Pb removal efficacy of the synthesized PVDF-COF membrane was 92.4%, decreasing to 87.5% by the fourth cycle. Consequently, this unique PVDF-COF composite is a promising adsorbent for the removal of Pb^{2+} from contaminated water and wastewater [177].

Two amide-based COFs, which were fabricated via the polymerization of acyl chloride and amino groups using mechanochemical ball milling under ambient conditions, acted as Pb^{2+} adsorbents. Specifically, COFs were synthesized using two types of diamine monomers: *p*-phenylenediamine as an aromatic diamine monomer to produce COF-TP and ethylenediamine as a linear diamine monomer to produce COF-TE [178]. These COF composites exhibited typical lamellar structures, with the amide groups in the COF skeleton acting as active adsorption sites for Pb^{2+} ions. The Pb^{2+} adsorption capacity of COF-TE was superior to that of COF-TP because the smaller aromatic skeleton and weak π–π stacking of COF-TE facilitated the internal diffusion of Pb^{2+}. In addition, COF-TE had a higher amide group, resulting in a maximum adsorption capacity of 185.7 mg g^{-1} compared with that of COF-TP (140 mg g^{-1}). Moreover, excellent recyclability via the adsorption–desorption of Pb^{2+} makes amide-based COFs favorable adsorbents for Pb^{2+} removal [178].

5.4.1.2. Removal of Mercury.

Azole and thiol groups were introduced into the structure of an imine-linked COF to yield a thiol-grafted imine-based COF (TPB-DMTP-COF-SH) with well-structured channels. This material exhibited an Hg adsorption capacity of 4395 mg g^{-1} with high selectivity of 99.98% in 2 min. In addition, a composite material comprising a covalent triazine framework (CTF-1) supporting Fe_2O_3 NPs (in the maghemite γ-Fe_2O_3 phase) was synthesized for Hg removal from wastewater [179]. The Hg^{2+} adsorption capacity of γ-Fe_2O_3@CTF-1 reached 165.8 mg g^{-1}, which was considerably higher than those of the corresponding pure covalent triazine framework or iron-based materials. The γ-Fe_2O_3@CTF-1 composite could also be reused for numerous cycles, maintain its remarkable adsorption capacity [179].

In further studies on Hg removal, an Ag NPs@COF composite was found to have an adsorption capacity of 113 mg g^{-1}, achieving 99% removal from water with good performance over five cycles [56]. Similarly, COOH@COF with 90 nm diameter nanowires acted as an adsorbent for Hg removal, with a maximum adsorption capacity of 99.1 mg g^{-1} and 90% Hg removal were achieved under optimum adsorption conditions of pH = 6.0 and 25 °C. In addition, 90% Hg removal was maintained over 20 cycles [174]. A 2D mesoporous COF containing dense, flexible thiol and thioether chelating groups yielded very high Hg^0 and Hg^{2+} adsorption capacities of 863 and 1350 mg g^{-1}, respectively [180]. Moreover, a high affinity for Hg^{2+} with remarkable dispersion coefficients was observed over a wide pH range (3–10), as well as fast ki-

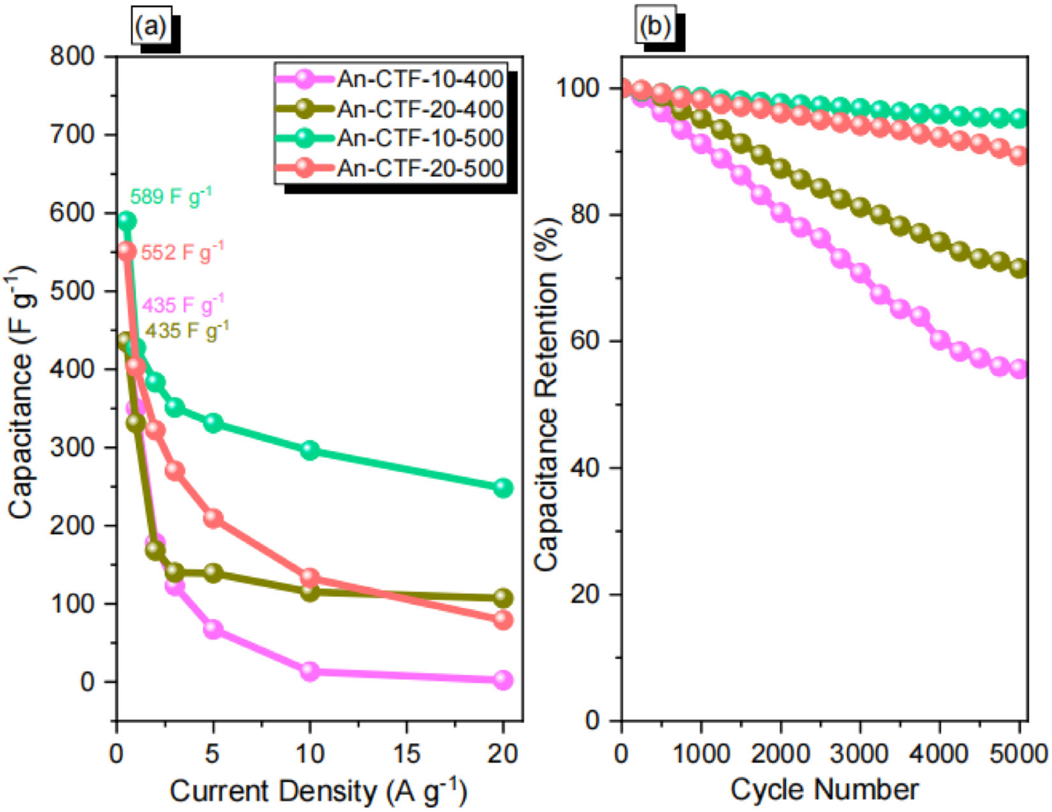

Fig. 32. (a) Capacitance and (b) cycle-life performance of cells with An-CTF-10-400, An-CTF-20-400, An-CTF-10-500, and CTF-20-500. Adapted from [9] under a Creative Commons license (CC BY 4.0).

netics for Hg^{2+} adsorption. These results demonstrate the remarkable potential of COFs as adsorbents for Hg^{2+} removal [180]. Moreover, a thioether-functionalized covalent triazine network (SCTN-1), fabricated via an efficient ionothermal method, achieved high Hg^0 and Hg^{2+} adsorption capacities of 813 and 1253 mg g^{-1}, respectively, fast adsorption kinetics, and facile regeneration [181].

A triazine-based COF (T-COF) exhibited an excellent adsorption capacity of 1826 mg g^{-1} for Hg removal at pH of 5 and ambient temperature. The high adsorption capacity of T-COF, which was maintained over three cycles, was attributed to electrostatic interactions between Hg and the nitrogen atoms localized on the surface of the adsorbent [182]. Furthermore, a sulfhydryl (–SH–)-modified COF (COF-SH) exhibited a high adsorption capacity of 1283 mg g^{-1} for Hg^{2+} removal, which was 25 times higher than that of the unmodified COF (183). COF-SH showed rapid adsorption kinetics, realizing 95% removal of 1000 μg L^{-1} Hg^{2+} within 30 min and exceeding 99% removal after 2 h. Furthermore, this COF exhibited a removal efficiency of > 99%, over a wide pH range as well as selectivity for Hg^{2+} in the presence of other metal cations [183]. Consequently, the COF-SH material demonstrated great potential for removing Hg^{2+} from water and wastewater samples under complex operational conditions [183].

5.4.1.3. Removal of cadmium.

As a unique heteroporous COF based on 2,3-Dha as a basic building block, COF-ETTA-2,3-Dha achieved the selective adsorption of Cd from aqueous solutions [17]. This COF exhibited hierarchical porosity, a large surface area, accessible metal ion chelating sites, high crystallinity, and chemical stability against water in a wide pH range owing to the intramolecular hydrogen-bonding interactions provided by the catechol segment [17]. The COF achieved a maximum adsorption capacity of 116 mg g^{-1}. However, adsorption capacities of 36 and 95.6 mg g^{-1} could be achieved with contact time of only 1 and 20 min. Moreover, the fabricated COF exhibited excellent recyclability and regeneration, with an insignificant decrease in the adsorption capacity for Cd removal during cycling [17].

A crystalline COF with an enhanced nitrogen atom content was fabricated via the condensation of a 2,4,6-tris(hydrazine)-1,3,5-triazine and a 2,4,6-tris(*p*-formylphenoxy)-1,3,5-triazine. The as-fabricated COF was highly efficient as an adsorbent for Cd^{2+} removal from wastewater, achieving an adsorption capacity of 396 mg g^{-1} [184].

5.4.1.4. Removal of Arsenic.

A composite material (γ-Fe_2O_3@CTF-1) consisting of CTF-1 and γ-Fe_2O_3 NPs was applied in environmental remediation studies for the adsorption of As^{3+} and As^{5+} from synthetic wastewater solutions as well real surface, ground, and wastewater [179]. The γ-Fe_2O_3@CTF-1 composite showed high adsorption removal efficiencies for both arsenite and arsenate, with adsorption capacities of 198 and 102.3 mg g^{-1}, respectively. These adsorption capacities were significantly higher than those achieved using conventional adsorbents, indicating the practical applicability of γ-Fe_2O_3@CTF-1 for water decontamination and wastewater treatment applications [179]. Furthermore, the removal of As was studied using an ethidium bromide (EB)-COF:Br material and Fe^0/COFs. The Fe^0/COFs were reported to exhibit remarkable performance for As^{3+} removal, with an optimum adsorption capacity of 135.78 mg g^{-1} [185,186].

5.4.1.5. Removal of chromium.

The modification of COFs with guanidinium has received attention for water treatment applications. Guanidinium, a positively charged nitrogen analogue of urea, can form strong ion pairs with oxoanions through electrostatic forces and hydrogen-bonding interactions [187]. Guanidinium was incorporated at the edges of the hexagonal pores of a COF, thereby increasing the surface area. This novel dual-pore COF exhibited adsorption capacities of 90–200 mg g^{-1} for Cr^{6+} ion removal [187]. Further studies on the use of dual-pore COFs for Cr^{6+} removal revealed fast adsorption kinetics, a Cr^{6+} adsorption capacity of 272 mg g^{-1} in 10 min, and a maximum Cr^{6+} adsorption capacity of 384 mg g^{-1} Cr^{6+}, which is among the highest values achieved for porous materials thus far [188].

In addition, a magnetic COF with the β-ketoenamine linkage synthesized via a facile hydrothermal route exhibited high stability, a high Cr^{6+} adsorption capacity of 245.45 mg g^{-1}, and excellent reusability. Owing to these remarkable features, this magnetic COF is a promising candidate for environmental remediation of heavy metal-contaminated water [189].

5.4.2. *Removal of radioactive elements*

5.4.2.1. *Removal of iodine.*

A COF was also demonstrated to exhibit a very high adsorption capacity of 4810 mg g^{-1} for the removal of volatile iodine owing to the encapsulation of iodine in the structured inner cavities and porous shells of the microspheres in the COF [190]. Nearly 96% of radioactive iodide was adsorbed by the COF during the fifth adsorption–desorption cycle, demonstrating the satisfactory selectivity and reusability of this material. Similarly, a COF network consisting of a microporous elastic hydrogen-bonded cross-linked organic framework (HCOFs) exhibited a rapid equilibrium rate (~ 30 min) and a high adsorption capacity of 2900 mg g^{-1} for radioactive iodine vapor [190].

Moreover, the fabrication of five different classes of 2D COFs pore sizes ranging from 2.2 to 3.3 nm were reported to exhibit an improvement in adsorption capacity as the pore size increased [191]. Up to 70 wt.% of radioactive iodine vapor was captured by the COFs, even at moderate temperature, indicating their impressive adsorption performance. Generally, the iodine adsorption mechanism on 2D COFs is considered to involve van der Waals forces and hydrophobic interactions with the inner cavities of the COF microspheres [191].

As a novel 2D imine-linked COF for the removal of radioactive iodine vapor, a COF@cotton fiber material was fabricated using an imine condensation reaction [192]. This material contained numerous imine functional groups and well-dispersed mesopores. These features result in a rapid adsorption rate and high iodine affinity, as revealed by the adsorption capacity of 533.9 mg g^{-1} [192]. A crystalline mesoporous nitrogen-containing COF, synthesized via an imine condensation reaction, was exploited as a highly efficient adsorbent for iodine removal [193]. The as-synthesized COF exhibited a porous structural network with a high BET surface area of 1082 m^2 g^{-1}, excellent thermal and chemical stabilities, and numerous nitrogen sites. An excellent iodine adsorption capacity of 988.17 mg g^{-1} was achieved under ambient conditions. These findings indicate the considerable potential of this COF for managing problematic nuclear fission waste contamination challenges [193].

5.4.2.2. *Removal of uranium.*

COF-HBI, which was synthesized using a one-step solvothermal method, demonstrated a high U(VI) adsorption capacity of 81 mg g^{-1} [194]. Further experimental studies established that the complexation affinity of U(VI) with the amidoxime groups in okadaic acid (AO)-functionalized COFs was considerably stronger than that with cyano or hydroxyl groups [195]. Consequently, amidoxime-functionalized PAF-1 (PAF-1-CH_2-AO) exhibited an excellent adsorption capacity of 300 mg g^{-1}, with the uranyl concentration decreasing from 4.1×10^{-6} to less than 1.0×10^{-9}, which is lower than the acceptable limit established the US EPA [196].

In addition, AO-COF/graphene composites (oxime-modified GS-COF or o-GS-COF) were characterized by high irradiation and acid stabilities, resulting from intra- and interlayer π–π interactions. The AO-modified COFs could provide improved selectivity for the adsorption of U(VI) in environmental remediation applications [37]. Recently, COF-TpPa was demonstrated to have an excellent adsorption capacity (52 mg g^{-1}), rapid adsorption kinetics, high selectivity, exceptional recycling performance in the presence of competing ions, and good chemical resistance to acids, bases, and high temperatures [197].

5.4.3. *Removal of pharmaceutical residues*

5.4.3.1. *Removal of nonsteroidal anti-inflammatory drugs (NSAIDs).*

NSAIDs are a group of drugs employed as pharmaceutical analgesics for the treatment and reduction of pain and, at higher doses, inflammation. Owing to their large-scale production and the improper disposal of these drugs in the environment, NSAID accumulation has been found in various water sources, including rivers and groundwater, resulting in an ecological predicament [24]. Recently, COFs have been demonstrated to have high selectivities and adsorption capacities for NSAIDs in contaminated wastewater. Two COF-based adsorbents (COF-NO_2 and COF-NH_2) were utilized for the adsorptive removal of three NSAIDs (ibuprofen, ketoprofen, and naproxen) [24,198]. The adsorption capacities of COF-NO_2 for ketoprofen, ibuprofen, and naproxen were as high as 70, 94, and 80 mg g^{-1}, respectively. In contrast, COF-NH_2 exhibited lower adsorption capacities of 33, 18, and 16 mg g^{-1}, respectively [198]. However, COF-NH_2 exhibited better selectivity for the adsorptive removal of ketoprofen than for ibuprofen or naproxen. The adsorption mechanism governing the removal of NSAIDs was attributed to hydrogen bonding between COF-NO_2 and NSAIDs [198]. Furthermore, the increased selectivity of COF-NH_2 for ketoprofen removal was reported to originate from (acid–base interactions, hydrogen bonding, and strong force C=N bonds between the –NH_2 groups of COF-NH_2 and the carbonyl groups of ketoprofen [198].

A fluorine-functionalized bulk COF was recently proposed as an effective adsorbent for ibuprofen elimination from water samples. The fabrication of magnetic COF composites that allow effective adsorbent recovery from a sample matrix has further advanced the application of COFs for contaminant removal [199]. A systemic series of COF composites was fabricated for the adsorptive elimination of sulfonamides, diclofenac, triclocarban, and triclosan from contaminated water. Among these composites, Fe_3O_4/TpPa-1 and Fe_3O_4/TAPB-DMTA exhibited adsorption capacities of 565 and 113 mg g^{-1}, respectively, for the elimination of sodium diclofenac and sulfamethazine from water [43,200].

5.4.3.2. *Removal of antibiotics.*

Nitrofurans (NFs) are a group of bacterial antibiotics with well-defined structures including a characteristic NF group and various side chains. NFs are frequently employed in medical treatments and in the animal breeding industry. As several human health problems can result from NF accumulation in water, their detection and removal are essential [24,201]. Two CTFs based on aggregation-induced emission luminogens (AIEgens) were synthesized via a condensation reaction between the structural building blocks, 4′,4′′,4′′′,4′′′′-(ethene-1,1,2,2-tetrayl) tetrakis(([1,1′-biphenyl]-4-carbaldehyde)) (ETTC), which exhibits AIE behavior, phenamidine hydrochloride, and diphenamidine hydrochloride. The resulting materials (F-CTF-1 and F-CTF-2) had ultrathin lamellar layers [24,202]. Both CTFs exhibited excellent performance for the adsorptive elimination of nitrofurazone (NZF), nitrofurantoin (NFT), and furazolidone (FZD). At pH 6, F-CTF-1 exhibited maximum adsorption capacities of 351, 240, and 196 mg g^{-1} for NZF, NFT, and FZD, respectively, whereas the adsorption capacities of F-CTF-2 were 298, 200, and 154 mg g^{-1}, respectively [202]. The adsorption mechanism was proposed to involve the N atoms in the triazine rings of the COFs as adsorption sites that can form strong interactions with the adsorbates. In addition, F-CTF-1 and F-CTF-2 both exhibited good recyclability and recovery of their initial adsorption capacities over five cycles [24,202].

5.4.4. *Removal of pesticide residues*

A magnetic TpBD-Me_2 composite was successfully applied as an adsorbent for the removal of endocrine-disrupting chemicals, such as pesticides, from contaminated water [203,204]. High removal efficiencies with maximum adsorption capacities of 54 and 270 mg g^{-1} were achieved for the removal of atrazine and chlorpyrifos, respectively, from contaminated wastewater [205]. Conversely, polar diquat exhibited a low adsorption efficacy of approximately 8%, thus demonstrating the selectivity of magnetic TpBD-Me_2. Hydrophobic interactions likely play an essential role in the adsorptive removal of polar diquat using magnetic TpBD-Me_2 [205]. Three COFs with different linkers (PDA, BD, and DT) were used for the adsorptive removal of the insecticide triphenyl phosphate from water. Good adsorption capacities of 387.2, 371.2, and 86.1 mg g^{-1} were achieved for COF-BD, COF-PDA, and COF-DT, respectively [206].

5.4.5. Removal of dyes

Two triazine-functionalized PI-based COFs were synthesized: macroporous TS-COF-1, a triazine-PI-COF with PMDA and TAPT building blocks, and microporous TS-COF-2, a triazine-Schiff base-COF with TP and TAPT building blocks [207]. When applied to the adsorptive elimination of methylene blue (MB), an excellent adsorption capacity of 1691 mg g^{-1} was achieved by TS-COF-1, which is the highest adsorption capacity reported for MB removal to date [207]. In contrast, TS-COF-2 exhibited a lower adsorption capacity of 377 mg g^{-1}. This difference in behavior was attributed to the sizes of the pores in the meso- and microporous TS-COF structures (31 and 11 Å, respectively) [207]. Thus, MB molecules, with a size of 13.4 Å × 5.0 Å × 4.2 Å, could enter and diffuse through TS-COF-1 more easily. In addition, the weak interaction between this COF and MB enabled the regeneration of the COF while maintaining its adsorption capacity over three cycles [24,207]. The TS-COF-1 adsorbent was also studied for the elimination of rhodamine B (RhB) and Congo red dyes, and adsorption capacities of 319 and 625 mg g^{-1}, respectively, were obtained [207].

MOF-5 was blended with a melamine-based COF to fabricate the MC5 composite, which exhibited outstanding adsorption capacities of 18 and 16 mg g^{-1} with a contact time of 8 min for the elimination of auramine-O and RhB, respectively [207].

5.4.6. Removal of other organic and inorganic compounds

TS-COF-1 was utilized for the removal of two other organic pollutants (4-nitrophenol and 3-nitrophenol) with adsorption capacities of 369 and 424 mg g^{-1}, respectively [24]. Using Fe_3O_4 as a superparamagnetic core and porous COF-TpBD as a shell, magnetic core–shell nanospheres (Fe_3O_4@TpBD) exhibited considerable potential for the removal of bisphenol A (BPA) and bisphenol AF (BPAF) from wastewater [208]. The adsorption kinetics of Fe_3O_4@TpBD followed a pseudo-second-order kinetic model and a contact time of 5 min was sufficient for adsorption equilibrium [208]. Further, Fe_3O_4@TpBD achieved a maximum adsorption capacity of 160.6 mg g^{-1} for BPA. The adsorption mechanism was proposed to be controlled by π–π interactions and hydrogen bonding between the hydroxyl groups in BPA and carboxyl groups of the COF [208]. Similarly, a magnetic COF based on Tp-COF series (Fe_3O_4@TpPa-1), achieved exceptional performance for the elimination of BPA in wastewater. The adsorption isotherms of Fe_3O_4@TpPa-1 were consistent with the Langmuir model, with maximum adsorption capacities of 1424.27 and 1220.97 mg g^{-1} for TpPa-1 and Fe_3O_4@TpPa-1, respectively, for removing BPA from wastewater at 298 K [24,189].

EB-COF:Br was also found to be a viable adsorbent for the removal of phosphate and phosphoric acid from water (25 °C, pH = 0.65–0.86). An adsorption capacity of 35.3 mg g^{-1} with 95% removal efficiency was realized for phosphoric acid. The adsorption process depended on electrostatic interactions between the negatively charge phosphate groups and positively charged $=N^{+}-$ groups of the COFs as well as hydrogen bonding [185,209].

5.4.7. Water desalination

NENP-1, a modified COF with a triazine structure, was used as a filler for polysulfonamide (PSA), which was synthesized via the interfacial polymerization (IP) of polyallylamine and 1,3-benzenedisulfonyl dichloride (BDSC) [24,210]. Owing to the porosity and hydrophilicity of the COF, the incorporation of 0.1 w/v% of NENP-1 increased the water flow and $MgCl_2$ rejection [210]. Higher concentrations of the COF led to worse performance because of particle aggregation. Further studies investigated different ions, which exhibited a rejection order of $CaCl_2$ > $ZnCl_2$ > $MgCl_2$ > $Pb(NO_3)_2$ > $MgSO_4$ > NaCl > Na_2SO_4 (94.9% > 93.8% > 93.3% > 92.4% > 90.2 > 58.2% > 54.3%), in agreement with the Donnan effect. This system achieved good compatibility between the polymer matrix and COF [24,210].

Similarly, IP of piperazine (PIP) and trimesoyl chloride (TMC) deposited on a 2D COF nanosheet composite was used to fabricate a PSA layer with a thickness <10 nm to obtain TpPa-1 covalent organic nanosheets (CONs) [102]. The high porosity and hydrophilicity of the TpPa-1 CONs enhanced the assembly of TMC and allowed hydrogen bonding of the PIP monomers on the surface. At the optimum dose of 0.5 mg TpPa-1 CONs, the water flux increased to 535.5 L m^{-2} h^{-1} MPa^{-1} and 94.3% Na_2SO_4 rejection was achieved [24,102].

The interactions between TMC and the amino groups during IP were also exploited for the fabrication of CONs (rCONs) of CTF-1, which were reported to enhance the antifouling properties and hydrophilicity [211]. The maximum water flux of 46.5 L m^{-2} h^{-1} bar^{-1} was obtained at an rCON loading 5 wt.%, which was 6.8 times higher than that with pristine PSA, and Na_2SO_4 rejection reached 93.5%. For other salts, the rejection order was Na_2SO_4 > $MgSO_4$ > $MgCl_2$ > NaCl, consistent with the Donnan theory [24,211].

5.5. Sensors

5.5.1. Electrochemical sensing

Metal NPs and carbon-based nanomaterials have been extensively utilized to prepare electrochemical sensors with unique surfaces. However, poor stability of the electrode surface can deteriorate repeatability [39]. To overcover this issue, current research on electrochemical sensing is focused on the incorporation of nanomaterials with large specific surfaces, high porosities, and high loading capabilities [39,140,212,213]. Although COFs offer many desirable properties, the intrinsically poor electrical conductivity of COFs is problematic for applications in electrochemistry. To increase the functionality of COFs, they have been combined with various highly conductive materials, including conductive polymers, magnetic NPs, carbon nanotubes, noble metal NPs, and GO [39,140,213-215].

For example, COFs were hybridized with Au NPs to yield a TAPB-DMTP@AuNP composite. As a sensor for the selective determination of chlorogenic acid in apples, coffee, and honeysuckle, this system achieved a detection limit of 9.5 nM [140]. The TAPB-DMTP@AuNP composite sensor demonstrated good selectivity for the target analyte complex matrices and could be reused for at least 100 cycles without any activity loss [39,140]. Notably, the composite electrode exhibited better electrochemical behavior than the bare Au NP electrode. This improvement was ascribed to the synergistic effect of the high conductivity of the Au NPs and the active sites of COF [39,140].

In addition, a TpPa-1@Ag NP composite was prepared by incorporating Ag NPs into COF. The Ag NPs were immobilized on the TpPa-1 surface through hydrogen bonding and π–π interactions. This composite exhibited selective recognition of target analyte, such as paraquat, in water samples with a detection limit of 0.014 μM [39,216].

The electrochemical response of a bare glass carbon electrode (GCE) to luteolin was compared with that of GCE coated with TAPB-DMTP COF or the TAPB-DMTP@Fe_3O_4 composite [217]. The COF coating substantially increased the characteristic signal, and a low detection limit of 7.2 nM was achieved, which was ascribed to the selective adsorption of luteolin on the surface of the COF through π–π stacking interactions. In addition, the signal was further enhanced with the magnetic COF coating [217]. This behavior was attributed to the synergistic effect of the improved electron transfer efficiency provided by Fe_3O_4 and the high surface area and active sites provided by TAPB-DMTP [39,217].

5.5.2. Luminescent sensing

Recently, fluorescence sensors have been prepared to exploit the conjugated structures of COFs. A core–shell composite obtained by blending COF-LZU1 as the shell with highly fluorescent NPs as the core. Lanthanide-doped upconversion nanoparticles (UCNPs) were selected as an ultrasensitive fluorescence sensor for analytical determination of perfluorooctane sulfonate (PFOS). The detection mechanism was ascribed to fluorescence quenching of the UCNPs in the presence of PFOS [39,218]. This novel COF-LZU1 composite was successfully applied for the selective detection of PFOS in water and food samples with a detection limit of 0.15 pM. The enhanced fluorescence intensity of the composite was attributed to the formation of –C=N– bonds, which increased the π-conjugation of the COF-LZU1 composite, thus enhancing its fluorescence response [39,218]. Similarly, a composite consisting of carbon dots (CDs) loaded in a RhB-prefunctionalized PT-DHTA COF (CDs/RhB@PT-DHTA) was used as a fluorescence probe for trace Hg(II) in cosmetic and water samples, and a detection limit of 15.9 nM was achieved [39,219].

In another approach, COFs were hybridized with molecularly imprinted polymers (MIPs) to obtain hybrid COF/MIP composites as fluorescence sensors. Furthermore, CDs as optosensing nanomaterials were incorporated into the hybrid COF/MIP composites. A composite consisting of CDs coated with an MIP and grafted onto the surface of TpPa-1 COF (CDs-MIP/TpPa-1) was applied to the selective sensing of 4-ethylguaiacol in wine samples with a detection limit of 0.11 μM [39,220,221]. TpPa-1 allowed efficient analyte adsorption and contributed to the selective exclusion of interfering chemical species. The CD fluorescence was quenched by transportation of the analyte to the core of the composite, where it interacted specifically with the molecular cavities of the MIP [39,220,221].

5.5.3. Colorimetric sensing

Colorimetric analysis, which does not require the use of advanced analytical instrumentation, is inexpensive and simple to operate with and good sensitivity. Thus far, COF-based composites fabricated by combining COFs and noble metal NPs have been employed for colorimetric assays [39,222]. Recently, a Pd NPs/CMC-LZU1 composite device, fabricated via the in-situ growth of Pd NPs on COF-LZU1 supported on carboxymethyl cellulose (CMC), was applied for the colorimetric detections of HeLa cancer cells in human serum samples. The surface area of the Pd NPs/CMC-LZU1 (403 $m^2\ g^{-1}$) was comparable to that of bulk COF-LZU1 (460 $m^2\ g^{-1}$). For the colorimetric assay, Pd NPs functionalized with folic acid (FA) were immobilized on the composite, resulting in a FA-Pd NPs/CMC-LZU1 composite with the capacity to specifically bind HeLa cancer cells with a detection limit of 100 cells mL^{-1} [39,222].

Moreover, two composites (Au NPs/TpBpy COF nanosheets and Au NPs/PTAzo COF) obtained by the in situ growth of Au NPs on a COF were used as colorimetric sensors for Hg(II) in water samples with detection limits of 0.33 and 0.75 nM, respectively. The Hg concentration was found to be directly proportional to the intensity of the color resulting from the oxidation of a 3,3′,5,5′-tetramethylbenzidine in the presence of hydrogen peroxide, which results in a color change from colorless to blue [223,224]. In addition, interference from other ions in the water samples were negligible because the high affinity between Au and Hg provided excellent selectivity. Disadvantageously, this strong interaction between Au and Hg results in the formation of an amalgam that limits the reusability of the sensor [39,223,224].

5.6. Photovoltaic devices

The incorporation of organic chromophores as building blocks during the fabrication of COFs can result in active sites for solar energy conversion. Under light irradiation, these sites can generate singlet excitons and act as electron donor (D) units for suitable acceptor (A) units incorporated into the pores of the COF [1,225].

5.6.1. COFs as electroactive materials

Two semiconductive and photoconductive COFs (TP-COF and PPy-COF) were fabricated based on a highly ordered π-conjugated pyrene derivative that can transport charge along the COF. TP-COF showed semiconducting characteristics and exhibited strong blue emission [1,226,227]. Upon harvesting visible light, TP-COF and PPy-COF generated photocurrents of 4.3 and 5 nA, respectively. In addition, TP-COF was able to harvest photons throughout the UV and visible regions, which were then converted to blue emission owing to intramolecular singlet energy transfer from the triphenylene to pyrene moiety. This behavior demonstrated electronic coupling between the building blocks in the COF structure [1,226,227].

5.6.2. D–A heterojunction systems

D–A systems consisting of electron-withdrawing A units alternately aligned with D units can improve charge carrier transport and light absorption [1,228]. A D–A COF system consisting of benzothiadiazole (A) and phthalocyanine (D) units exhibited periodic D-on-D and A-on-A channels that delivered vertically orientated D and A heterojunction arrays. These arrays promoted the transport of electrons and holes through the aligned columns of benzothiadiazole and phthalocyanine unites, respectively. Notably, charge carrier transport in this system followed a different path than in the n-type phthalocyanine COF [1,228].

5.6.3. Fully π-conjugated systems

A fully π-conjugated COF system was synthesized using all-sp^2-hybridized carbon atoms extended into a 2D lattice with π-conjugation. The sp^2-hybridized c-COF demonstrated oxidation and reduction potentials of 0.94 and −0.96 eV, respectively, with a narrow band gap of 1.90 eV [1,87]. When the sp^2-hybridized c-COF was doped with I_2, the conductivity increased by 12 orders of magnitude to 7.1×10^{-2} S m^{-1}. The color could be altered by changing the linking group and extending the π-conjugated system. In particular, red and yellow were obtained for sp^2 c-COF and the imine-linked 2D COF, respectively [1,87].

5.6.4. 2D COFs based on π-electron-rich macrocycles

The introduction of π-electron-rich macrocycles, including phthalocyanine and porphyrin, into the structural building blocks of the COF can enhance the optical absorption capacity and charge transport [1,229]. Similarly, the integration of a metal phthalocyanine into the structural network of the COF increased the panchromatic light response and photoconductivity owing to high charge carrier mobility in the π-systems of the 2D metal phthalocyanine with well-ordered stacking layers [1,230,231]. In terms of broadness and intensity, the central metal ion in the metal phthalocyanine has been shown to have a strong effect on charge carrier transport and light absorption. For instance, 2D NiPc-COF, prepared by integrating a well-ordered nickel phthalocyanine stacking unit into the COF structure, exhibited light-harvesting capabilities in the near-IR and visible regions [1,230,231].

5.6.5. COF thin films

Thin films are advantageous for applications in photoelectronic devices. Therefore, the fabrication and electronic characteristics of COF-based thin films have been investigated. The high crystallinity and orientation of a COF thin film on a single-layer graphene/SiO_2 substrate was used to fabricate photovoltaic devices with functional π-electron systems consisting of crystalline and aligned triphenylene-pyrene COF or phthalocyanine COF thin films [1,232-234].

An electron acceptor, comprising I_2 and tetracyanoquinodimethane as charge-transfer partners, was integrated into the structural network of a COF to produce an oriented TTF-COF thin film. For these thin films, the relative conductivites were measure using an Au/Cr electrode [1,128,235]. Direct charge carrier transport along the columnar stacks of a COF thin film was achieved in an oriented BDT-COF thin-film device. The BDT-COF thin films with thicknesses in the range of 80–200 nm exhibited higher hole mobility because the thinness of these films led to a lower content of electronic defects [1,236].

5.6.6. 3D COFs as new platforms for next-generation photovoltaic devices

3D COFs have been proposed as new platforms for next-generation crystalline organic photovoltaic devices. For example, a subphthalocyanine-based 3D COF that can form co-crystals with fullerene (C60) through periodic ball-and-socket binding motifs was developed [1,237,238]. In perovskite solar cells (PSCs), doping with 3D COFs can increase the power efficiency and charge transport ability. For instance, compared with an undoped PSC, simple bulk doping with 3D spirobifluorene-based COFs (SP-3D-COFs) significantly enhanced the average power conversion efficiency (15.9% and 18.0% for SP-3D-COF 1 and SP-3D-COF 2, respectively [1,239]. In addition, the 3D framework of these SP-3D-COFs can provide electron transport channels in highly ordered and aligned frameworks, thereby improving the charge transport in planar-type PSCs. In such cases, a few layers of CONs exfoliated from the COFs can be utilized as the hole-transport layer combined with poly(ethylenedioxythiophene): polystyrene sulfonate (PEDOT:PSS). When these layers were employed as an interlayer material in an inverted planar PSC, the power conversion efficiency reached 10.2%, which corresponding to a 1% increase compared with that of the reference device [1,240].

5.7. Chromatographic and spectroscopic analyses

The development of COF-derived functionalized nanocomposites has gained significant attention for specialized instrumental analysis that require matrix separation prior to quantitative and qualitative characterization of the analytes. Recently, a unique COF functionalized with hydrophilic magnetic graphene (magG@PDA@TbBd), which was fabricated using a facile and efficient method, was employed as a magnetic solid-phase extraction matrix for the analysis of phthalate esters [63]. In addition, magG@PDA@TbBd exhibited excellent water dispersibility, a strong magnetic response, a large surface area, a mesoporous structure, and a strong π–π electron system. Owing to these characteristics, magG@PDA@TbBd demonstrated excellent performances for the analysis of phthalates with reliable recoveries (91.4%–105.2%), good linearity in the range of 50–8000 ng mL^{-1}, and satisfactory reusability [63]. Furthermore, the limit of detection was in the range of 0.004–0.02 ng mL^{-1}, and the intraday and interday relative standard deviations were less than 4.4% and 6.7%, respectively. Notably, magG@PDA@TbBd was successfully used for the analysis of nine phthalate acid esters in packaged milk samples [63].

Nitrogen-rich triazine-based COFs were successfully applied for the ^{1}H NMR analysis of nitrogen and sulfur mustards in the presence of background levels of hydrocarbons [241]. Nitrogen-rich triazine-based COFs were also for solid-phase extraction to prepare of samples for gas chromatography analysis. This system achieved good linearity at concentrations of 0.05–100.00, 0.04–20.00, and 0.20–20.00 μg mL^{-1} for organophosphate esters, nerve agents, and mustards, respectively, with correlation coefficients in the range of 0.9867–0.9998 [241]. Furthermore, for organophosphate esters, nerve agents, and blister agents, the limits of detection were 0.015–0.050, 0.010–0.030, and 0.05–1.00 μg mL^{-1}, respectively, whereas the limits of quantification were 0.050–0.200, 0.040–0.100, and 0.180–0.350 μg mL^{-1}, respectively [241].

A Au NP/COF composite was utilized as a surface-enhanced Raman scattering platform for the detection of β-lactoglobulin, polycyclic aromatic hydrocarbons (PAHs), and adenosine triphosphate in food, water, and urine samples [242–244]. Similarly, an Au NP/SNW-1 COF composite was applied as a surface-enhanced Raman scattering platform to identify different PAHs in pond and tap water, with limits of detection in the range of 1.0–0.1 μM [242]. Lastly, crystalline and highly COFs were embedded with radicals to construct peroxyl-radical-embedded COFs (PR(χ)-CFs) for dynamic nuclear polarization enhancement during solid-state NMR analysis [245].

5.8. Biomedical applications

5.8.1. Bioimaging

Bioimaging via fluorescence imaging has been recognized as an important technique for facilitating preliminary medical diagnosis and the detection of various cancers. COFs are promising candidates for bioimaging application owing to their advantageous properties, including π–π stacking, long-range crystal domains, high photostability, extended π-conjugation, and minimal toxicity [246]. A benzothiadiazole-based COF (TPI-COF) was found to increase two-photon induction (TPI) to achieve highly efficient two-photon promoted fluorescence emission. This system outperformed those obtained using previous conventional techniques such as polymerization and molecular design. In addition, TPI-COF was successfully employed for confirming malignant cellular dispersion and endocytosis processes [246–248].

Fluorescein sodium was integrated into a COF to yield TpPa-1@Dye as a hydrogel. This system was applied to analyze sialic acid (SA) as a potential ovarian cancer biomarker. Using TpPa-1@Dye as an indicator with Cr^{3+} as an electron-deficient receptor, ultrasensitive SA detection with a broad linear range (10^{-8} to 10^{-2} M) was achieved. The competitive SA and Cr^{3+} interaction provide a potential avenue for cancer imaging and diagnosis [246,249].

Furthermore, for bioimaging applications, MCOF nanospheres were fabricated with highly crystalline COFs as the shell and Fe_3O_4 nanoassemblies as the core. The unique fluorescence quenching interaction between hairpin DNA and MCOF was utilized for the sensitive identification and quantification of miRNA-182 in the serum of glioma patients, thereby facilitating glioma detection and diagnosis [246,250].

5.8.2. Drug delivery

The excellent properties of COFs, including high surface areas, high porosities, and tunable pore sizes and geometries combined with the ability of various COFs to effectively disintegrate in the slightly acidic tumor microenvironment offer a competitive advantage for the targeted delivery of a number of anticancer drugs to tumor sites [246]. For instance, for chemotherapeutic drug delivery, two 3D PI-COFs (PI-COF-5 and PI-COF-4), based on pyromellitic dianhydride and tetra(4-aminophenyl)methane or 1,3,5,7-tetraaminoadamantane, achieved high ibuprofen loadings and well-controlled release profiles [10,80]. COFs prepared via the condensation of amines and aldehydes, were applied as drug carriers for captopril, 5-FU, and ibuprofen, achieving high loading capacities, high release capacities, and low degrees of cytotoxicity [10,251]. Similarly, a nanoscale covalent triazine polymer employed as a carrier for the anticancer drug doxorubicin realized controlled released profiles at pH of 4.8 and 7.4 [10,252]. Owing to the high stability and biocompatibility of COF NPs as drug carriers, a quercetin-loaded COF (TTI-COF@Q) was successfully engulfed by human breast carcinoma cells and induced apoptosis. Furthermore, compared with the direct administration of this drug, TTI-COF@Q suppressed the proliferation rate of human breast carcinoma cells [246,253].

In another study, improved antitumor efficiency was achieved owing to the high drug-loading capacity and pH-responsive of doxorubicin-loaded DOX@COF. Compared with administering doxorubicin alone, the high biocompatibility and pH-responsiveness of DOX@COF could induce cancer therapeutic effects and decrease the overdose risk [246,253].

6. Perspectives

Research on the synthesis of high-quality COF materials has been aimed at in developing new strategies. One recently reported novel approach involves the use of multicomponent reaction and multistep synthesis strategies, in which more than two types of building blocks are used to fabricate COFs, thereby enriching the structural diversity (Fig. 1). The catalyst has also been reported to play a significant role in fabricating enriched COF materials. For example, the utilization of basic pyrrolidine as a catalyst promotes the conversion of amorphous polyimine to TpBD-based COF crystals. In contrast, aqueous acetic acid is typically used as an efficient catalyst in the synthesis of most imine-linked COFs materials.

Furthermore, the linker-exchange strategy has received recent attention for the synthesis of COFs at a solid-solution interface, allowing the transformation of COFs with amorphous properties into highly crystalline COF materials. The linker-exchange strategy has also been integrated with the multicomponent reaction and multistep synthesis strategies to fabricate COFs with more than two types of building blocks (Fig. 1). Lastly, the synthesis of 3D COFs is of considerable interest, as these materials have been proposed a new platform for next-generation crystalline organic photovoltaic devices. In addition, COFs have recently been considered as promising candidates for biomedical applications, such as bioimaging for preliminary cancer diagnosis and drug delivery.

7. Concluding remarks

This review provided an extensive overview of COFs as a class of porous polymers with a high crystallinity and considerable advantages over other porous materials, including MOFs, CMPs, SOFs, and inorganic zeolites, owing to their predictable design, structural diversity, high surface areas, and tunable properties and functions. Significant advances have been made in the development of design strategies (e.g., type of COF linker and hybridization for COF-based composites), synthetic methodologies, characterization techniques, and applications in a wide range of fields. In particular, COFs have potential applicability in catalysis, photovoltaic devices, chromatographic and spectroscopic analyses, sensors, biomedicine, gas storage, and environmental remediation.

COF materials have been used for water treatment for less than a decade, but significant outcomes for water desalination and treatment have provided prospects for the utilization of COFs as an efficient membranes and adsorbents for the elimination of pollutants from water. Nevertheless, there is a lack of information on the employment of COFs in some critical areas of water treatment, including membrane distillation and electrodialysis. Hence, deeper insight into the structure–performance relationships of COFs is critical for both current and future applications of COFs. In addition, COFs have been reported to play a crucial role in biomedical applications, including drug delivery. Furthermore, COFs have been applied for bioimaging in various biomedical studies involving the preliminary diagnosis and early detection of various cancers.

However, the techno-economical assessment of COFs is an essential challenge associated with the cost of synthesizing COF-based materials compared with other commercially available materials. Thus, there is a necessity to guide synthetic methodologies coupled with biocompatibility toward cost-effective and large-scale design and fabrication strategies for industrial applications. Such progress would enable the engineering of novel COF platforms for groundbreaking applications with considerable impact for addressing societal challenges.

Declaration of Competing Interests

The author declares that there are no known competing financial interests or personal relationships that could have appeared to influence the work reported in this paper.

References

[1] H.R. Abuzeid, A.F.M. EL-Mahdy, S.W. Kuo, Covalent organic frameworks: Design principles, synthetic strategies, and diverse applications, Giant 6 (2021) 100054.

[2] A.P. Côté, A.I. Benin, N.W. Ockwig, M. O'Keeffe, A.J. Matzger, O.M. Yaghi, Porous, crystalline, covalent organic frameworks, Science 310 (2005) 1166–1170.

[3] J. Gong, R.B. Lin, B. Chen, Conjugated microporous polymers with rigid backbones for organic solvent nanofiltration, Chem. 4 (2018) 2269–2271.

[4] W.T. Chung, I. Mekhemer, M.G. Abuosoaud, A. Elewa, A. EL-Mahdy, H.H. Chou, S.W. Kuo, K.C.W. Wu, Recent advances in metal/covalent organic frameworks based materials: Their synthesis, structure design and potential applications for hydrogen production, Coord. Chem. Rev. 483 (2023) 215066.

[5] M.G. Mohamed, T.C. Chen, S.W. Kuo, Solid-state chemical transformations to enhance gas capture in benzoxazine-linked conjugated microporous polymers, Macromolecules 54 (2021) 5866–5877.

[6] M. Mohamed Samy, I.M.A. Mekhemer, M.G. Mohamed, M. Hammad Elsayed, K.H. Lin, Y.K. Chen, Conjugated microporous polymers incorporating thiazolo[5,4-d]thiazole moieties for sunlight-driven hydrogen production from water, Chem. Eng. J. 446 (2022) 137158.

[7] M. Ejaz, M.G. Mohamed, S.W. Kuo, Solid state chemical transformation provides a fully benzoxazine-linked porous organic polymer displaying enhanced CO_2 capture and supercapacitor performance, Polym. Chem. 14 (2023) 2494–2509.

[8] M.G. Mohamed, H.Y. Hu, M. Madhu, M.M. Samy, I.M.A. Mekhemer, W.L. Tseng, Ultrastable two-dimensional fluorescent conjugated microporous polymers containing pyrene and fluorene units for metal ion sensing and energy storage, Eur. Polym. J. 189 (2023) 111980.

[9] M.G. Mohamed, S.U. Sharma, N.Y. Liu, T.H. Mansoure, M.M. Samy, S.V. Chaganti, Ultrastable covalent triazine organic framework based on anthracene moiety as platform for high-performance carbon dioxide adsorption and supercapacitors, Int. J. Mol. Sci. 23 (2022) 3174.

[10] L. Song, X. Wang, M. Zhang, W. Jia, Q. Wang, W. Ye, A single-component supramolecular organic framework with efficient ultralong phosphorescence, CCS Chem. 3 (2021) 466–472.

[11] W. Yao, C. Ma, H. Ma, L. Fu, S. Lu, A. Lv, Supramolecular organic frameworks with ultralong phosphorescence via breaking π-conjugated structures, Giant 1 (2020) 1–7.

[12] B.M. Weckhuysen, J. Yu, Recent advances in zeolite chemistry and catalysis, Chem Soc Rev 44 (2015) 7022–7024.

[13] S. Akinnawo, Synthesis, modification, applications and challenges of titanium dioxide nanoparticles, Res. J. Nanosci. Eng. 3 (2019) 10–22.

[14] K.A. Adegoke, S.O. Akinnawo, O.S. Bello, N.W. Maxakato, R.O. Adegoke, R.K. Gupta, T.A. NguyenYasin GBT-M-OF-BN for EC and S, Chapter 6 -MOF-based electrocatalysts for oxygen evolution reactions, , Micro and Nano Technologies editors, Elsevier, 2022, pp. 107–134.

[15] J. Liu, G. Han, D. Zhao, K. Lu, J. Gao, T.S. Chung, Self-standing and flexible covalent organic framework (COF) membranes for molecular separation, Sci. Adv. 6 (2020) 1–9.

[16] Y. Song, Q. Sun, B. Aguila, S. Ma, Opportunities of covalent organic frameworks for advanced applications, Adv Sci 6 (2019) 1801410.

[17] N. Liu, L. Shi, X. Han, Q.Y. Qi, Z.Q. Wu, X. Zhao, A heteropore covalent organic framework for adsorptive removal of Cd(II) from aqueous solutions with high efficiency, Chinese Chem. Lett. 31 (2020) 386–390.

[18] M.S. Lohse, T. Bein, Covalent organic frameworks: Structures, synthesis, and applications, Adv Funct Mater 28 (2018) 1705553.

[19] S.Y. Ding, W. Wang, Covalent organic frameworks (COFs): From design to applications, Chem Soc Rev 42 (2013) 548–568.

[20] R.K. Sharma, P. Yadav, M. Yadav, R. Gupta, P. Rana, A. Srivastava, Recent development of covalent organic frameworks (COFs): Synthesis and catalytic (organic–electro-photo) applications, Mater. Horizons 7 (2020) 411–454.

[21] J. Wang, S. Zhuang, Covalent organic frameworks (COFs) for environmental applications, Coord Chem Rev 400 (2019) 213046.

[22] Y. Sun, Z. Ning, A. Ishag, Y. Li, H. Wang, H. Guo, P. Mei, Q. Meng, Recent investigations and progress in environmental remediation by using covalent organic framework-based adsorption method: A review, J. Clean. Prod. 277 (2020) 123360.

[23] M. Gatou, P. Bika, T. Stergiopoulos, P. Dallas, E.A. Pavlatou, Recent advances in covalent organic frameworks for heavy metal removal applications, Energies 14 (2021) 1–26.

[24] C. Arqueros, F. Zamora, C. Montoro, A Perspective on the application of covalent organic frameworks for detection and water treatment, Nanomaterials 11 (2021) 1–31.

[25] Z. Xia, Y. Zhao, S.B. Darling, Covalent organic frameworks for water treatment, Adv. Mater. Interfaces. 8 (2021) 2001507.

[26] J.L. Segura, M.J. Mancheño, F. Zamora, Covalent organic frameworks based on Schiff-base chemistry: Synthesis, properties and potential applications, Chem. Soc. Rev. 45 (2016) 5635–5671.

[27] F.J. Uribe-Romo, J.R. Hunt, H. Furukawa, C. Klöck, M. O'Keeffe, O.M. Yaghi, A crystalline imine-linked 3-D porous covalent organic framework, J. Am. Chem. Soc. 131 (2009) 4570–4571.

[28] S. Dalapati, S. Jin, J. Gao, Y. Xu, A. Nagai, D. Jiang, An azine-linked covalent organic framework, J. Am. Chem. Soc. 135 (2013) 17310–17313.

[29] Y. Li, C. Wang, S. Ma, H. Zhang, J. Ou, Y. Wei, Fabrication of hydrazone-linked covalent organic frameworks using alkyl amine as building block for high adsorption capacity of metal ions, ACS Appl. Mater. Interfaces. 11 (2019) 11706–11714.

[30] X. Qin, X. Tang, Y. Ma, H. Xu, Q. Xu, W. Yang, Decorating covalent organic frameworks with high-density chelate groups for uranium extraction, Chem. Res. Chinese Univ. 38 (2022) 433–439.

[31] A. Nagai, Z. Guo, X. Feng, S. Jin, X. Chen, X. Ding, Pore surface engineering in covalent organic frameworks, Nat. Commun. 2 (2011) 536.

[32] Z. Qu, C. Lai, G. Zhao, A. Knebel, H. Fan, H. Meng, Pore engineering in covalent organic framework membrane for gas separation, Adv. Membr. 2 (2022) 100037.

[33] X. Xu, X. Wu, K. Xu, H. Xu, H. Chen, N. Huang, Pore partition in two-dimensional covalent organic frameworks, Nat. Commun. 14 (2023) 1–9.

[34] T. Ma, L. Wei, L. Liang, S. Yin, L. Xu, Diverse crystal size effects in covalent organic frameworks, Nat. Commun. 11 (2020) 1–9.

[35] C. Liu, Y. Jiang, A. Nalaparaju, J. Jiang, A. Huang, Post-synthesis of a covalent organic framework nanofiltration membrane for highly efficient water treatment, J. Mater. Chem. A. 7 (2019) 24205–24210.

[36] H. Yang, L. Yang, H. Wang, Z. Xu, Y. Zhao, Y. Luo, Covalent organic framework membranes through a mixed-dimensional assembly for molecular separations, Nat. Commun. 10 (2019) 2101.

[37] R. Wen, Y. Li, M. Zhang, X. Guo, X. Li, X. Li, Graphene-synergized 2D covalent organic framework for adsorption: A mutual promotion strategy to achieve stabilization and functionalization simultaneously, J. Hazard Mater. 358 (2018) 273–285.

[38] Z.J. Xia, H.C. Yang, Z. Chen, R.Z. Waldman, Y. Zhao, C. Zhang, Porphyrin covalent organic framework (POF)-based interface engineering for solar steam generation, Adv. Mater. Interfaces. 6 (2019) 1900254.

[39] J.J. Jarju, A.M. Lavender, B. Espiña, V. Romero, L.M. Salonen, Covalent organic framework composites : Synthesis and analytical applications, Molecules 25 (2020) 1–41.

[40] L.L. Wang, C.X. Yang, X.P. Yan, In situ growth of covalent organic framework shells on silica microspheres for application in liquid chromatography, Chempluschem 82 (2017) 933–938.

[41] H.L. Qian, C. Yang, X.P. Yan, Layer-by-layer preparation of 3D covalent organic framework/silica composites for chromatographic separation of position isomers, Chem. Commun. 54 (2018) 11765–11768.

[42] S. He, T. Zeng, S. Wang, H. Niu, Y. Cai, Facile synthesis of magnetic covalent organic framework with three-dimensional bouquet-like structure for enhanced extraction of organic targets, ACS Appl. Mater. Interfaces. 9 (2017) 2959–2965.

[43] L. Huang, N. Mao, Q. Yan, D. Zhang, Q. Shuai, Magnetic covalent organic frameworks for the removal of diclofenac sodium from water, ACS Appl. Nano Mater. 3 (2020) 319–326.

[44] D. Hao, J. Zhang, H. Lu, W. Leng, R. Ge, X. Dai, Fabrication of a COF-5 membrane on a functionalized α-Al_2O_3 ceramic support using a microwave irradiation method, Chem. Commun. 5 (2014) 1462–1464.

[45] H. Lu, C. Wang, J. Chen, R. Ge, W. Leng, B. Dong, A novel 3D covalent organic framework membrane grown on a porous α-Al_2O_3 substrate under solvothermal conditions, Chem. Commun. 51 (2015) 15562–15565.

[46] H. Fan, J. Gu, H. Meng, A. Knebel, J. Caro, High-flux membranes based on the covalent organic framework COF-LZU1 for selective dye separation by nanofiltration, Angew Chem. Int. Ed. Engl. 57 (2018) 4083–4087.

[47] H. Fan, M. Peng, I. Strauss, A. Mundstock, H. Meng, J. Caro, High-flux vertically aligned 2D covalent organic framework membrane with enhanced hydrogen separation, J. Am. Chem. Soc. 142 (2020) 6872–6877.

[48] C. Wang, W. Gao, N. Liu, Y. Xin, X. Liu, X. Wang, Covalent organic framework decorated TiO_2 nanotube arrays for photoelectrochemical cathodic protection of steel, Corros. Sci. 176 (2020) 108920.

[49] S.B. Kalidindi, H. Oh, M. Hirscher, D. Esken, C. Wiktor, T.S. Metal@COFs, Covalent organic frameworks as templates for Pd nanoparticles and hydrogen storage properties of Pd@COF-102 hybrid material, Chem – A. Eur. J. 18 (2012) 10848–10856.

[50] P. Pachfule, S. Kandambeth, D. Díaz Díaz, R. Banerjee, Highly stable covalent organic framework–Au nanoparticles hybrids for enhanced activity for nitrophenol reduction, Chem. Commun. 50 (2014) 3169–3172.

[51] P. Pachfule, M.K. Panda, S. Kandambeth, S.M. Shivaprasad, D.D. Díaz, R. Banerjee, Multifunctional and robust covalent organic framework–nanoparticle hybrids, J. Mater. Chem. A. 2 (2014) 7944–7952.

[52] X. Shi, Y. Yao, Y. Xu, K. Liu, G. Zhu, L. Chi, Imparting catalytic activity to a covalent organic framework material by nanoparticle encapsulation, ACS Appl. Mater. Interfaces. 9 (2017) 7481–7488.

[53] G.J. Chen, X.B. Li, C.C. Zhao, H.C. Ma, J.L. Kan, Y.B. Xin, Ru nanoparticles-loaded covalent organic framework for solvent-free one-pot tandem reactions in air, Inorg. Chem. 57 (2018) 2678–2685.

[54] M. Bhadra, H.S. Sasmal, A. Basu, S.P. Midya, S. Kandambeth, P. Pachfule, Predesigned metal-anchored building block for in situ generation of Pd nanoparticles in porous covalent organic framework: Application in heterogeneous tandem catalysis, ACS Appl. Mater. Interfaces. 9 (2017) 13785–13792.

[55] C. Hu, Z. Zhang, S. Liu, X. Liu, M. Pang, Monodispersed CuSe sensitized covalent organic framework photosensitizer with an enhanced photodynamic and photothermal effect for cancer therapy, ACS Appl. Mater. Interfaces. 11 (2019) 23072–23082.

[56] L. Wang, H. Xu, Y. Qiu, X. Liu, W. Huang, N. Yan, Utilization of Ag nanoparticles anchored in covalent organic frameworks for mercury removal from acidic waste water, J. Hazard Mater. 389 (2020) 121824.

[57] J.X. Guo, H.L. Qian, X. Zhao, C. Yang, X.P. Yan, In situ room-temperature fabrication of a covalent organic framework and its bonded fiber for solid-phase microextraction of polychlorinated biphenyls in aquatic products, J. Mater. Chem. A. 7 (2019) 13249–13255.

[58] Y. Tian, Y. Hou, Q. Yu, X. Wang, M. Tian, Layer-by-layer self-assembly of a novel covalent organic frameworks microextraction coating for analyzing polycyclic aromatic hydrocarbons from aqueous solutions via gas chromatography, J. Sep. Sci. 43 (2020) 896–904.

[59] L. Wen, P. Wu, L.L. Wang, L.Z. Chen, M.L. Wang, X. Wang, Solid-phase microextraction using a β-ketoenamine-linked covalent organic framework coating for efficient enrichment of synthetic musks in water samples, Anal. Methods. 12 (2020) 2434–2442.

[60] I.A. Kinloch, J. Suhr, J. Lou, R.J. Young, P.M. Ajayan, Composites with carbon nanotubes and graphene: An outlook, Science 362 (2018) 547–553.

[61] L. Chen, W. Wang, Q. Fang, K. Zuo, G. Hou, Q. Ai, High performance hierarchically nanostructured graphene oxide/covalent organic framework hybrid membranes for stable organic solvent nanofiltration, Appl. Mater. Today. 20 (2020) 100791.

[62] J. Wang, J. Li, M. Gao, X. Zhang, Self-assembling covalent organic framework functionalized magnetic graphene hydrophilic biocomposites as an ultrasensitive matrix for N-linked glycopeptide recognition, Nanoscale 9 (2017) 10750–10756.

[63] Y. Lu, B. Wang, C. Wang, Y. Yan, D. Wu, H. Liang, A covalent organic framework-derived hydrophilic magnetic graphene composite as a unique platform for detection of phthalate esters from packaged milk samples, Chromatographia 82 (2019) 1089–1099.

[64] Y.J. Yu, W. Li, S.B. Ren, X.J. Zhou, D.M. Han, Rational design of COF–MOF composites for ratiometric fluorescence detection of phosphate, New J. Chem. 47 (2023) 6186–6190.

[65] J. Fu, S. Das, G. Xing, T. Ben, V. Valtchev, S. Qiu, Fabrication of COF-MOF composite membranes and their highly selective separation of H_2/CO_2, J. Am. Chem. Soc. (2016).

[66] B.P. Biswal, H.D. Chaudhari, R. Banerjee, U.K. Kharul, Chemically stable covalent organic framework (COF)-polybenzimidazole hybrid membranes: Enhanced gas separation through pore modulation, Chemistry 22 (2016) 4695–4699.

[67] R. Wang, X. Shi, Z. Zhang, A. Xiao, S.P. Sun, Z. Cui, Undirectional diffusion synthesis of covalent organic frameworks (COFs) on polymeric substrates for dye separation, J. Memb. Sci. 586 (2019) 274–280.

[68] S.B. Alahakoon, G.T. McCandless, A.A.K. Karunathilake, C.M. Thompson, R.A. Smaldone, Enhanced structural organization in covalent organic frameworks through fluorination, Chemistry 23 (2017) 4255–4259.

[69] S.B. Alahakoon, C.M. Thompson, A.X. Nguyen, G. Occhialini, G.T. McCandless, R.A. Smaldone, An azine-linked hexaphenylbenzene based covalent organic framework, Chem. Commun. 52 (2016) 2843–2845.

[70] J. Lu, F. Lin, Q. Wen, Q.Y. Qi, J.Q. Xu, X. Zhao, Large-scale synthesis of azine-linked covalent organic frameworks in water and promoted by water, New J. Chem. 43 (2019) 6116–6120.

[71] X. Li, Y. Qi, G. Yue, Q. Wu, Y. Li, M. Zhang, Solvent- and catalyst-free synthesis of an azine-linked covalent organic framework and the induced tautomerization in the adsorption of U(vi) and Hg(ii), Green Chem. 21 (2019) 649–657.

[72] P. Guan, J. Qiu, Y. Zhao, H. Wang, Z. Li, Y. Shi, A novel crystalline azine-linked three-dimensional covalent organic framework for CO_2 capture and conversion, Chem. Commun. 55 (2019) 12459–12462.

[73] S. Kandambeth, A. Mallick, B. Lukose, M.V. Mane, T. Heine, R. Banerjee, Construction of crystalline 2D covalent organic frameworks with remarkable chemical (acid/base) stability via a combined reversible and irreversible route, J. Am. Chem. Soc. 134 (2012) 19524–19527.

[74] A.F.M. EL-Mahdy, Y.H. Hung, T.H. Mansoure, H.H. Yu, Y.S. Hsu, K.C.W. Wu, Synthesis of $[3+3]$ β-ketoenamine-tethered covalent organic frameworks (COFs) for high-performance supercapacitance and CO_2 storage, J. Taiwan Inst. Chem. Eng 103 (2019) 199–208.

[75] Y. Zhang, X. Shen, X. Feng, H. Xia, Y. Mu, X. Liu, Covalent organic frameworks as pH responsive signaling scaffolds, Chem. Commun. 52 (2016) 11088–11091.

[76] Y. Wang, Y. Liu, H. Li, X. Guan, M. Xue, Y. Yan, Three-dimensional mesoporous covalent organic frameworks through steric hindrance engineering, J. Am. Chem. Soc. 142 (2020) 3736–3741.

[77] L. Stegbauer, K. Schwinghammer, B.V. Lotsch, A hydrazone-based covalent organic framework for photocatalytic hydrogen production, Chem. Sci. 5 (2014) 2789–2793.

[78] Z.J. Li, S.Y. Ding, H.D. Xue, W. Cao, W. Wang, Synthesis of –C=N– linked covalent organic frameworks via the direct condensation of acetals and amines, Chem. Commun. 52 (2016) 7217–7220.

[79] Q. Fang, Z. Zhuang, S. Gu, R.B. Kaspar, J. Zheng, J. Wang, Designed synthesis of large-pore crystalline polyimide covalent organic frameworks, Nat. Commun. 5 (2014) 4503.

[80] Q. Fang, J. Wang, S. Gu, R.B. Kaspar, Z. Zhuang, J. Zheng, 3D porous crystalline polyimide covalent organic frameworks for drug delivery, J. Am. Chem. Soc. 137 (2015) 8352–8355.

[81] C. Montoro, D. Rodríguez-San-Miguel, E. Polo, R. Escudero-Cid, M.L. Ruiz–González, J.A.R. Navarro, Ionic conductivity and potential application for fuel cell of a modified imine-based covalent organic framework, J. Am. Chem. Soc. 139 (2017) 10079–10086.

[82] S.Y. Ding, J. Gao, Q. Wang, Y. Zhang, W.G. Song, C.Y. Su, Construction of covalent organic framework for catalysis: Pd/COF-LZU1 in Suzuki–Miyaura coupling reaction, J. Am. Chem. Soc. 133 (2011) 19816–19822.

[83] D.M. Fischbach, G. Rhoades, C. Espy, F. Goldberg, B.J. Smith, Controlling the crystalline structure of imine-linked 3D covalent organic frameworks, Chem. Commun. 55 (2019) 3594–3597.

[84] X. Wu, B. Wang, Z. Yang, L. Chen, Novel imine-linked covalent organic frameworks: Preparation, characterization and application, J. Mater. Chem. A 7 (2019) 5650–5655.

[85] M.G. Rabbani, A.K. Sekizkardes, Z. Kahveci, T.E. Reich, R. Ding, H.M. El-Kaderi, A 2D mesoporous imine-linked covalent organic framework for high pressure gas storage applications, Chemistry 19 (2013) 3324–3328.

[86] W.L. Dong, S.Y. Li, J.Y. Yue, C. Wang, D. Wang, L.J. Wan, Fabrication of bilayer tetrathiafulvalene integrated surface covalent organic frameworks, Phys. Chem. Chem. Phys. 18 (2016) 17356–17359.

[87] E. Jin, M. Asada, Q. Xu, S. Dalapati, M.A. Addicoat, M.A. Brady, Two-dimensional sp(2) carbon-conjugated covalent organic frameworks, Science 357 (2017) 673–676.

[88] X. Zhuang, W. Zhao, F. Zhang, Y. Cao, F. Liu, S. Bi, A two-dimensional conjugated polymer framework with fully sp2-bonded carbon skeleton, Polym. Chem. 7 (2016) 4176–4181.

[89] R. Chen, J.L. Shi, Y. Ma, G. Lin, X. Lang, C. Wang, Designed synthesis of a 2D porphyrin-based sp(2) carbon-conjugated covalent organic framework for heterogeneous photocatalysis, Angew Chem. Int. Ed. Engl. 58 (2019) 6430–6434.
[90] Y. Zhao, H. Liu, C. Wu, Z. Zhang, Q. Pan, F. Hu, Fully Conjugated two-dimensional sp(2) -carbon covalent organic frameworks as artificial photosystem i with high efficiency, Angew Chem. Int. Ed. Engl. 58 (2019) 5376–5381.
[91] J. You, Y. Zhao, L. Wang, W. Bao, Recent developments in the photocatalytic applications of covalent organic frameworks: A review, J. Clean Prod. 291 (2021) 125822.
[92] K. Geng, V. Arumugam, H. Xu, Y. Gao, D. Jiang, Covalent organic frameworks: Polymer chemistry and functional design, Prog. Polym. Sci. 108 (2020) 101288.
[93] F. Haase, E. Troschke, G. Savasci, T. Banerjee, V. Duppel, S. Dörfler, Topochemical conversion of an imine- into a thiazole-linked covalent organic framework enabling real structure analysis, Nat. Commun. 9 (2018) 2600.
[94] P.J. Waller, Y.S. AlFaraj, C.S. Diercks, N.N. Jarenwattananon, O.M. Yaghi, Conversion of imine to oxazole and thiazole linkages in covalent organic frameworks, J. Am. Chem. Soc. 140 (2018) 9099–9103.
[95] P. Kuhn, M. Antonietti, A. Thomas, Porous, covalent triazine-based frameworks prepared by ionothermal synthesis, Angew Chem. Int. Ed. Engl. 47 (2008) 3450–3453.
[96] X. Chen, M. Addicoat, E. Jin, H. Xu, T. Hayashi, F. Xu, Designed synthesis of double-stage two-dimensional covalent organic frameworks, Sci. Rep. 5 (2015) 1–19.
[97] Y. Zeng, R. Zou, Z. Luo, H. Zhang, X. Yao, X. Ma, Covalent organic frameworks formed with two types of covalent bonds based on orthogonal reactions, J. Am. Chem. Soc. 137 (2015) 1020–1023.
[98] H. Li, Q. Pan, Y. Ma, X. Guan, M. Xue, Q. Fang, Three-dimensional covalent organic frameworks with dual linkages for bifunctional cascade catalysis, J. Am. Chem. Soc. 138 (2016) 14783–14788.
[99] X. Guan, Y. Ma, H. Li, Y. Yusran, M. Xue, Q. Fang, Fast, Ambient temperature and pressure ionothermal synthesis of three-dimensional covalent organic frameworks, J. Am. Chem. Soc. 140 (2018) 4494–4498.
[100] B.J. Smith, A.C. Overholts, N. Hwang, W.R. Dichtel, Insight into the crystallization of amorphous imine-linked polymer networks to 2D covalent organic frameworks, Chem. Commun. 52 (2016) 3690–3693.
[101] C. Qian, Q.Y. Qi, G.F. Jiang, F.Z. Cui, Y. Tian, X. Zhao, Toward covalent organic frameworks bearing three different kinds of pores: The strategy for construction and COF-to-COF transformation via heterogeneous linker exchange, J. Am. Chem. Soc. 139 (2017) 6736–6743.
[102] N. Li, J. Du, D. Wu, J. Liu, N. Li, Z. Sun, Recent advances in facile synthesis and applications of covalent organic framework materials as superior adsorbents in sample pretreatment, TrAC Trends Anal. Chem. 108 (2018) 154–166.
[103] S. Cao, B. Li, R. Zhu, H. Pang, Design and synthesis of covalent organic frameworks towards energy and environment fields, Chem. Eng. J. 355 (2019) 602–623.
[104] B.T. Koo, R.F. Heden, P. Clancy, Nucleation and growth of 2D covalent organic frameworks: Polymerization and crystallization of COF monomers, Phys. Chem. Chem. Phys. 19 (2017) 9745–9754.
[105] V. Singh, S. Jang, N.K. Vishwakarma, D.P. Kim, Intensified synthesis and post-synthetic modification of covalent organic frameworks using a continuous flow of microdroplets technique, NPG Asia Mater. 10 (2018) e456–e456.
[106] A. Kuchenbuch, R. Giernoth, Ionic liquids beyond simple solvents: Glimpses at the state of the art in organic chemistry, ChemistryOpen 4 (2015) 677–681.
[107] Y. Gao, C. Wang, H. Hu, R. Ge, M. Lu, J. Zhang, Synthesis of two-dimensional covalent organic frameworks in ionic liquids, Chemistry 25 (2019) 15488–15492.
[108] J. Gan, A.R. Bagheri, N. Aramesh, I. Gul, M. Franco, Y.Q. Almulaiky, Covalent organic frameworks as emerging host platforms for enzyme immobilization and robust biocatalysis - A review, Int. J. Biol. Macromol. 167 (2021) 502–515.
[109] M.J. Bojdys, J. Jeromenok, A. Thomas, M. Antonietti, Rational extension of the family of layered, covalent, triazine-based frameworks with regular porosity, Adv. Mater. 22 (2010) 2202–2205.
[110] L.A. Baldwin, J.W. Crowe, D.A. Pyles, P.L. McGrier, Metalation of a mesoporous three-dimensional covalent organic framework, J. Am. Chem. Soc. 138 (2016) 15134–15137.
[111] N.L. Campbell, R. Clowes, L.K. Ritchie, A.I. Cooper, Rapid microwave synthesis and purification of porous covalent organic frameworks, Chem. Mater. 21 (2009) 204–206.
[112] L.K. Ritchie, A. Trewin, A. Reguera-Galan, T. Hasell, A.I. Cooper, Synthesis of COF-5 using microwave irradiation and conventional solvothermal routes, Microporous Mesoporous Mater. 132 (2010) 132–136.
[113] H. Lyu, B. Gao, F. He, C. Ding, J. Tang, J.C. Crittenden, Ball-milled carbon nanomaterials for energy and environmental applications, ACS Sustain Chem. Eng. 5 (2017) 9568–9585.
[114] T. Friščić, New opportunities for materials synthesis using mechanochemistry, J. Mater. Chem. 20 (2010) 7599–7605.
[115] S.L. James, C.J. Adams, C. Bolm, D. Braga, P. Collier, T. Friščić, Mechanochemistry: Opportunities for new and cleaner synthesis, Chem. Soc. Rev. 41 (2012) 413–447.
[116] B.P. Biswal, S. Chandra, S. Kandambeth, B. Lukose, T. Heine, R. Banerjee, Mechanochemical synthesis of chemically stable isoreticular covalent organic frameworks, J. Am. Chem. Soc. 135 (2013) 5328–5331.
[117] X. Wang, R. Ma, L. Hao, Q. Wu, C. Wang, Z. Wang, Mechanochemical synthesis of covalent organic framework for the efficient extraction of benzoylurea insecticides, J. Chromatogr. A 1551 (2018) 1–9.
[118] J.H. Bang, K.S. Suslick, Applications of ultrasound to the synthesis of nanostructured materials, Adv. Mater. 22 (2010) 1039–1059.
[119] S.T. Yang, J. Kim, H.Y. Cho, S. Kim, W.S. Ahn, Facile synthesis of covalent organic frameworks COF-1 and COF-5 by sonochemical method, RSC Adv. 2 (2012) 10179–10181.
[120] J. Yoo, S. Lee, S. Hirata, C. Kim, C.K. Lee, T. Shiraki, In situ synthesis of covalent organic frameworks (COFs) on carbon nanotubes and graphenes by sonochemical reaction for CO_2 adsorbents, Chem. Lett. 44 (2015) 560–562.
[121] S. Kim, H.C. Choi, Light-promoted synthesis of highly-conjugated crystalline covalent organic framework, Commun. Chem. 2 (2019) 60, doi:10.1038/s42004-019-0162-z.
[122] E. Jin, J. Li, K. Geng, Q. Jiang, H. Xu, Q. Xu, D. Jiang, Designed synthesis of stable light-emitting two-dimensional sp^2 carbon-conjugated covalent organic frameworks, Nat. Commun. 9 (2018) 1–10.
[123] P. Wang, Q. Wu, L. Han, S. Wang, S. Fang, Z. Zhang, Synthesis of conjugated covalent organic frameworks/graphene composite for supercapacitor electrodes, RSC Adv. 5 (2015) 27290–27294.
[124] M. Çalışkan, T. Baran, Design of a palladium nanocatalyst produced from Schiff base modified dialdehyde cellulose and its application in aryl halide cyanation and reduction of nitroarenes, Cellulose 29 (2022) 4475–4493.
[125] C. Zhu, S. Pang, Z. Chen, L. Bi, S. Wang, C. Liang, Synthesis of covalent organic frameworks (COFs)-nanocellulose composite and its thermal degradation studied by TGA/FTIR, Polymers (Basel) 14 (2022) 3158.
[126] H. Guo, L. Zhang, R. Xue, B. Ma, W. Yang, Eyes of covalent organic frameworks: Cooperation between analytical chemistry and COFs, Rev. Anal. Chem. 38 (2019) 20170023.
[127] P. Katekomol, J. Roeser, M. Bojdys, J. Weber, A. Thomas, Covalent triazine frameworks prepared from 1,3,5-tricyanobenzene, Chem. Mater. 25 (2013) 1542–1548.
[128] H. Ding, Y. Li, H. Hu, Y. Sun, J. Wang, C. Wang, A tetrathiafulvalene-based electroactive covalent organic framework, Chemistry 20 (2014) 14614–14618.
[129] J. Ma, X.B. Fu, Y. Li, T. Xia, L. Pan, Y.F. Yao, Solid-state NMR study of adsorbed water molecules in covalent organic framework materials, Microporous Mesoporous Mater. 305 (2020) 110287.
[130] A. Halder, M. Ghosh, M.A. Khayum, S. Bera, M. Addicoat, H.S. Sasmal, Interlayer hydrogen-bonded covalent organic frameworks as high-performance supercapacitors, J. Am. Chem. Soc. 140 (2018) 10941–10945.
[131] C. Zhang, G. Li, Z. Zhang, A hydrazone covalent organic polymer based micro–solid phase extraction for online analysis of trace Sudan dyes in food samples, J. Chromatogr. A 1419 (2015) 1–9.
[132] J. Li, X. Yang, C. Bai, Y. Tian, B. Li, S. Zhang, A novel benzimidazole-functionalized 2-D COF material: Synthesis and application as a selective solid-phase extractant for separation of uranium, J. Colloid Interface Sci. 437 (2015) 211–218.
[133] X. Zhong, W. Liang, Z. Lu, M. Qiu, B. Hu, Ultra-high capacity of graphene oxide conjugated covalent organic framework nanohybrid for U(VI) and Eu(III) adsorption removal, J. Mol. Liq. 323 (2021) 114603.
[134] W. Li, H.X. Jiang, Y. Geng, X.H. Wang, R.Z. Gao, A.N. Tang, Facile removal of phytochromes and efficient recovery of pesticides using heteropore covalent organic framework-based magnetic nanospheres and electrospun films, ACS Appl. Mater. Interfaces. 12 (2020) 20922–20932.
[135] X. Wan, X. Wang, G. Chen, C. Guo, B. Zhang, Covalent organic framework/nanofibrillated cellulose composite membrane loaded with Pd nanoparticles for dechlorination of dichlorobenzene, Mater. Chem. Phys. 246 (2020) 122574.
[136] Y.H. Pang, Q. Yue, Y.Y. Huang, C. Yang, X.F. Shen, Facile magnetization of covalent organic framework for solid-phase extraction of 15 phthalate esters in beverage samples, Talanta 206 (2020) 120194.
[137] D. Rodríguez-San-Miguel, A. Yazdi, V. Guillerm, J. Pérez-Carvajal, V. Puntes, D. Maspoch, Confining functional nanoparticles into colloidal imine-based COF spheres by a sequential encapsulation-crystallization method, Chemistry 23 (2017) 8623–8627.
[138] W. Li, L. Huang, D. Guo, Y. Zhao, Y. Zhu, Self-assembling covalent organic framework functionalized poly (styrene-divinyl benzene-glycidylmethacrylate) composite for the rapid extraction of non-steroidal anti-inflammatory drugs in wastewater, J. Chromatogr. A 1571 (2018) 76–83.
[139] K.M. Koczkur, S. Mourdikoudis, L. Polavarapu, S.E. Skrabalak, Polyvinylpyrrolidone (PVP) in nanoparticle synthesis, Dalt Trans. 44 (2015) 17883–17905.
[140] T. Zhang, Y. Chen, W. Huang, Y. Wang, X. Hu, A novel AuNPs-doped COFs composite as electrochemical probe for chlorogenic acid detection with enhanced sensitivity and stability, Sensors Actuators B Chem. 276 (2018) 362–369.
[141] H. Zhu, X. Yang, E.D. Cranston, S. Zhu, Flexible and porous nanocellulose aerogels with high loadings of metal-organic-framework particles for separations applications, Adv. Mater. 28 (2016) 7652–7657.
[142] A.F.M. EL-Mahdy, C.H. Kuo, A. Alshehri, C. Young, Y. Yamauchi, J. Kim, Strategic design of triphenylamine- and triphenyltriazine-based two-dimensional covalent organic frameworks for CO_2 uptake and energy storage, J. Mater. Chem. A. 6 (2018) 19532–19541.
[143] H. Furukawa, O.M. Yaghi, Storage of hydrogen, methane, and carbon dioxide in highly porous covalent organic frameworks for clean energy applications, J. Am. Chem. Soc. 131 (2009) 8875–8883.
[144] Y. Zhang, S.N. Riduan, Functional porous organic polymers for heterogeneous catalysis, Chem. Soc. Rev. 41 (2012) 2083–2094.
[145] R.L. Wang, D.P. Li, L.J. Wang, X. Zhang, Z.Y. Zhou, J.L. Mu, The preparation of new covalent organic framework embedded with silver nanoparticles and its applications in degradation of organic pollutants from waste water, Dalt Trans. 48 (2019) 1051–1059.
[146] M.Y. Gao, C.C. Li, H.L. Tang, X.J. Sun, H. Dong, F.M. Zhang, Boosting visible-light–driven hydrogen evolution of covalent organic frameworks through compositing with MoS_2: A promising candidate for noble-metal-free photocatalysts, J. Mater. Chem. A 7 (2019) 20193–20200.
[147] P. Verma, J.J.M. Le Brocq, R. Raja, Rational design and application of covalent organic frameworks for solar fuel production, Molecules 26 (2021) 4181.

[148] D. Wang, H. Zeng, X. Xiong, M.F. Wu, M. Xia, M. Xie, Highly efficient charge transfer in CdS-covalent organic framework nanocomposites for stable photocatalytic hydrogen evolution under visible light, Sci. Bull 65 (2020) 113–122.
[149] L. Li, Z. Zhou, L. Li, Z. Zhuang, J. Bi, J. Chen, Thioether-functionalized 2D covalent organic framework featuring specific affinity to Au for photocatalytic hydrogen production from seawater, ACS Sustain. Chem. Eng. 7 (2019) 18574–18581.
[150] Y. Fu, X. Zhu, L. Huang, X. Zhang, F. Zhang, W. Zhu, Azine-based covalent organic frameworks as metal-free visible light photocatalysts for CO_2 reduction with H_2O, Appl. Catal. B Environ. 239 (2018) 46–51.
[151] S. Guo, P. Yang, Y. Zhao, X. Yu, Y. Wu, H. Zhang, Direct Z-scheme heterojunction of SnS(2) /sulfur-bridged covalent triazine frameworks for visible-light-driven CO(2) photoreduction, ChemSusChem 13 (2020) 6278–6283.
[152] Z. Fu, X. Wang, A.M. Gardner, X. Wang, S.Y. Chong, G. Neri, A stable covalent organic framework for photocatalytic carbon dioxide reduction, Chem. Sci. 11 (2020) 543–550.
[153] K. Guo, X. Zhu, L. Peng, Y. Fu, R. Ma, X. Lu, Boosting photocatalytic CO_2 reduction over a covalent organic framework decorated with ruthenium nanoparticles, Chem. Eng. J. 405 (2021) 127011.
[154] X. Chen, Q. Dang, R. Sa, L. Li, L. Li, J. Bi, Integrating single Ni sites into biomimetic networks of covalent organic frameworks for selective photoreduction of CO_2, Chem. Sci. 11 (2020) 6915–6922.
[155] Y.N. Gong, W. Zhong, Y. Li, Y. Qiu, L. Zheng, J. Jiang, Regulating photocatalysis by spin-state manipulation of cobalt in covalent organic frameworks, J. Am. Chem. Soc. 7 (2020) 142.
[156] E.L. Spitler, B.T. Koo, J.L. Novotney, J.W. Colson, F.J. Uribe-Romo, G.D. Gutierrez, A 2D covalent organic framework with 4.7-nm pores and insight into its interlayer stacking, J. Am. Chem. Soc. 133 (2011) 19416–19421.
[157] M. Wang, H. Guo, R. Xue, Q. Li, H. Liu, N. Wu, Covalent organic frameworks: A new class of porous organic frameworks for supercapacitor electrodes, ChemElectroChem 6 (2019) 2984–2997.
[158] C.R. DeBlase, K. Hernández-Burgos, K.E. Silberstein, G.G. Rodríguez-Calero, R.P. Bisbey, H.D. Abruña, Rapid and efficient redox processes within 2D covalent organic framework thin films, ACS Nano 9 (2015) 3178–3183.
[159] M.G. Mohamed, A.F.M. El-Mahdy, M.M.M. Ahmed, S.W. Kuo, Direct synthesis of microporous bicarbazole-based covalent triazine frameworks for high-performance energy storage and carbon dioxide uptake, Chempluschem 84 (2019) 1767–1774.
[160] A.F.M. El-Mahdy, Y.H. Hung, T.H. Mansoure, H.H. Yu, T. Chen, S.W. Kuo, A Hollow Microtubular triazine- and benzobisoxazole-based covalent organic framework presenting sponge-like shells that functions as a high-performance supercapacitor, Chem. Asian J. 14 (2019) 1429–1435.
[161] A.F.M. EL-Mahdy, C. Young, J. Kim, J. You, Y. Yamauchi, S.W. Kuo, Hollow microspherical and microtubular [3 + 3] carbazole-based covalent organic frameworks and their gas and energy storage applications, ACS Appl. Mater. Interfaces 11 (2019) 9343–9354.
[162] A.F.M. EL-Mahdy, M.B. Zakaria, H.X. Wang, T. Chen, Y. Yamauchi, S.W. Kuo, Heteroporous bifluorenylidene-based covalent organic frameworks displaying exceptional dye adsorption behavior and high energy storage, J. Mater. Chem. A 8 (2020) 25148–25155.
[163] A. Solomon, The emergence of nanotechnology and its applications, Res. J. Nanosci. Eng. 2 (2018) 8–12.
[164] Y.A. Adeshina, A. Solomon, A.F. Ademola, Contamination levels of organochlorine and organophosphorous pesticide residues in water and sediment from river Owena, Nigeria. Curr. J. Appl. Sci. Technol. 34 (2019) 1–11.
[165] O.A. Ajala, S.O. Akinnawo, A. Bamisaye, D.T. Adedipe, M.O. Adesina, O.A. Okon-Akan, Adsorptive removal of antibiotic pollutants from wastewater using biomass/biochar-based adsorbents, RSC Adv. 13 (2023) 4678–4712.
[166] S.O. Akinnawo, P.O. Ayadi, M. Temitope, Chemical coagulation and biological techniques for wastewater treatment, Ovidius University Annals of Chemistry 34 (2023) 14–21.
[167] S.O. Akinnawo, K.A. Adegoke, T.A. Ajala, R.O. Adegoke, W.N. Maxakato, O.S. Bello, Modified biomass adsorbents for removal of organic pollutants : A review of batch and optimization studies, Int. J. Environ. Sci. Technol. 20 (2023) 11615–11644.
[168] S.O. Akinnawo, Eutrophication : Causes, consequences, physical, chemical and biological techniques for mitigation strategies, Environmental Challenges 12 (2023) 1–18.
[169] A. Solomon, K. Rasheed, E. Olanipekun, Spatial distribution and speciation of heavy metals in sediment of river Ilaje, Nigeria. Int. Res. J. Pure Appl. Chem. 10 (2015) 1–10.
[170] K. Rasheed, A. Solomon, A. Aiyesanmi, Chemical speciation and fractionation study of heavy metals in top sediment deposit of Owena river, Nigeria. Phys. Sci. Int. J. 21 (2019) 1–13.
[171] A. Peter, O. Ajayi, E. Abata, A. Solomon, M. Oluwalope, Chemical fractionation of heavy metals in the soil of auto-mechanic workshops in Akure, Ondo State, Nigeria. Chem. Sci. Int. J. 21 (2018) 1–16.
[172] A. Solomon, A. Christiana, E. Olanipekun, Seasonal variation in the physico-chemical and microbial characterization of sediment and water samples from selected areas in Ondo coastal region, Nigeria. J. Geogr. Environ. Earth Sci. Int. 5 (2016) 1–12.
[173] K. Adesina, S.O. Akinnawo, O. Aderemi, T. Adewumi, W.N. Maxakato, O.S. Bello, Progress and challenges in batch and optimization studies on the adsorptive removal of heavy metals using modified biomass-based adsorbents, Bioresour. Technol. Reports. 19 (2022) 1–12.
[174] X.F. Lu, W.H. Ji, L. Yuan, S. Yu, D.S. Guo, Preparation of carboxy-functionalized covalent organic framework for efficient removal of Hg^{2+} and Pb^{2+} from water, Ind. Eng. Chem. Res. 58 (2019) 17660–17667.
[175] T. Xu, L. Zhou, Y. He, S. An, C. Peng, J. Hu, Covalent organic framework with triazine and hydroxyl bifunctional groups for efficient removal of lead(II) ions, Ind. Eng. Chem. Res. 58 (2019) 19642–19648.
[176] Y. Cao, X. Hu, C. Zhu, S. Zhou, R. Li, H. Shi, Sulfhydryl functionalized covalent organic framework as an efficient adsorbent for selective Pb (II) removal, Colloids Surfaces A Physicochem Eng. Asp. 600 (2020) 125004.
[177] W. Xu, X. Sun, M. Huang, X. Pan, X. Huang, H. Zhuang, Novel covalent organic framework/PVDF ultrafiltration membranes with antifouling and lead removal performance, J. Environ. Manage. 269 (2020) 110758.
[178] G. Li, J. Ye, Q. Fang, F. Liu, Amide-based covalent organic frameworks materials for efficient and recyclable removal of heavy metal lead (II), Chem. Eng. J. 370 (2019) 822–830.
[179] K. Leus, K. Folens, N.R. Nicomel, J.P.H. Perez, M. Filippousi, M. Meledina, Removal of arsenic and mercury species from water by covalent triazine framework encapsulated γ-Fe_2O_3 nanoparticles, J. Hazard Mater. 353 (2018) 312–319.
[180] B. Sun, J. Liu, A. Cao, W. Song, D. Wang, Interfacial synthesis of ordered and stable covalent organic frameworks on amino-functionalized carbon nanotubes with enhanced electrochemical performance, Chem. Commun. 53 (2017) 6303–6306.
[181] S. Mondal, S. Chatterjee, S. Mondal, A. Bhaumik, Thioether-functionalized covalent triazine nanospheres: A robust adsorbent for mercury removal, ACS Sustain. Chem. Eng. 7 (2019) 7353–7361.
[182] M. Afshari, M. Dinari, K. Zargoosh, H. Moradi, Novel triazine-based covalent organic framework as a superadsorbent for the removal of mercury(II) from aqueous solutions, Ind. Eng. Chem. Res. 59 (2020) 9116–9126.
[183] Z. Ma, F. Liu, N. Liu, W. Liu, M. Tong, Facile synthesis of sulfhydryl modified covalent organic frameworks for high efficient Hg(II) removal from water, J. Hazard Mater. 405 (2021) 124190.
[184] M. Dinari, M. Hatami, Novel N-riched crystalline covalent organic framework as a highly porous adsorbent for effective cadmium removal, J. Environ. Chem. Eng. 7 (2019) 102907.
[185] C.H. Yang, J.S. Chang, D.J. Lee, Covalent organic framework EB-COF:Br as adsorbent for phosphorus (V) or arsenic (V) removal from nearly neutral waters, Chemosphere 253 (2020) 126736.
[186] X. Liu, H. Xu, L. Wang, Z. Qu, N. Yan, Surface nano-traps of FeO/COFs for arsenic(III) depth removal from wastewater in non-ferrous smelting industry, Chem. Eng. J. 381 (2020) 122559.
[187] S. Jansone-Popova, A. Moinel, J.A. Schott, S.M. Mahurin, I. Popovs, G.M. Veith, Guanidinium-based ionic covalent organic framework for rapid and selective removal of toxic Cr(VI) oxoanions from water, Environ. Sci. Technol. 53 (2019) 878–883.
[188] F.Z. Cui, R.R. Liang, Q.Y. Qi, G.F. Jiang, X. Zhao, Efficient removal of Cr(VI) from aqueous solutions by a dual-pore covalent organic framework, Adv. Sustain. Syst. 3 (2019) 1800150.
[189] X. Zhong, Z. Lu, W. Liang, B. Hu, The magnetic covalent organic framework as a platform for high-performance extraction of Cr(VI) and bisphenol a from aqueous solution, J. Hazard Mater. 393 (2020) 122353.
[190] Y. Lin, X. Jiang, S.T. Kim, S.B. Alahakoon, X. Hou, Z. Zhang, An elastic hydrogen-bonded cross-linked organic framework for effective iodine capture in water, J. Am. Chem. Soc. 139 (2017) 7172–7175.
[191] P. Wang, Q. Xu, Z. Li, W. Jiang, Q. Jiang, D. Jiang, Exceptional iodine capture in 2D covalent organic frameworks, Adv. Mater. 30 (2018) 1801991.
[192] Y. Li, Y. Li, Q. Zhao, L. Li, R. Chen, C. He, Cotton fiber functionalized with 2D covalent organic frameworks for iodine capture, Cellulose 27 (2020) 1–13.
[193] R. Chen, T. Hu, Y. Li, Stable nitrogen-containing covalent organic framework as porous adsorbent for effective iodine capture from water, React Funct. Polym. 159 (2020) 104806.
[194] L. Suo, J. Li, Y. Meng, H. Li, Graph-based fair resource allocation scheme combining interference alignment in femtocell networks, IET Commun. 9 (2015) 211–218.
[195] C. Bai, M. Zhang, B. Li, X. Zhao, S. Zhang, L. Wang, Modifiable diyne-based covalent organic framework: A versatile platform for in situ multipurpose functionalization, RSC Adv. 6 (2016) 39150–39158.
[196] B. Li, Q. Sun, Y. Zhang, C.W. Abney, B. Aguila, W. Lin, S. Ma, Functionalized porous aromatic framework for efficient uranium adsorption from aqueous solutions, ACS Appl. Mater. Interfaces. 9 (2017) 12511–12517.
[197] Z.D. Li, H.Q. Zhang, X.H. Xiong, F. Luo, U(VI) adsorption onto covalent organic frameworks-TpPa-1, J. Solid State Chem. 277 (2019) 484–492.
[198] Y. Liang, L. Feng, X. Liu, Y. Zhao, Q. Chen, Z. Sui, Enhanced selective adsorption of NSAIDs by covalent organic frameworks via functional group tuning, Chem. Eng. J. 404 (2021) 127095.
[199] A. Mellah, S.P.S. Fernandes, R. Rodríguez, J. Otero, J. Paz, J. Cruces, Adsorption of pharmaceutical pollutants from water using covalent organic frameworks, Chem – A Eur. J. 24 (2018) 10601–10605.
[200] S. Zhuang, R. Chen, Y. Liu, J. Wang, Magnetic COFs for the adsorptive removal of diclofenac and sulfamethazine from aqueous solution: Adsorption kinetics, isotherms study and DFT calculation, J. Hazard Mater. 385 (2020) 121596.
[201] A. Peter, A. Solomon, Isolation and anti-bacterial activity of the active components from the stem-back of enantial chlorantha, European J. Med. Plants. 22 (2018) 1–7.
[202] Y. Tang, H. Huang, W. Xue, Y. Chang, Y. Li, X. Guo, Rigidifying induced fluorescence enhancement in 2D porous covalent triazine framework nanosheets for the simultaneously luminous detection and adsorption removal of antibiotics, Chem. Eng. J. 384 (2020) 123382.
[203] A. Solomon, Determination of organochlorine pesticide residues in water and sediment samples from selected areas of river Ilaje, Nigeria. Chem. Sci. Int. J. 11 (2015) 1–6.

[204] A. Solomon, Concentration of organophosphorous pesticide residues in water and sediment samples from river Ilaje, Nigeria. Chem. Sci. Int. J. 11 (2015) 1–9.

[205] V. Romero, S.P.S. Fernandes, P. Kovář, M. Pšenička, Y.V. Kolen'ko, L.M. Salonen, Efficient adsorption of endocrine-disrupting pesticides from water with a reusable magnetic covalent organic framework, Microporous Mesoporous Mater. 307 (2020) 110523.

[206] W. Wang, S. Deng, L. Ren, D. Li, W. Wang, M. Vakili, Stable covalent organic frameworks as efficient adsorbents for high and selective removal of an aryl-organophosphorus flame retardant from water, ACS Appl. Mater. Interfaces. 10 (2018) 30265–30272.

[207] X. Zhu, S. An, Y. Liu, J. Hu, H. Liu, C. Tian, Efficient removal of organic dye pollutants using covalent organic frameworks, AIChE J. 63 (2017) 3470–3478.

[208] Y. Li, C.X. Yang, X.P. Yan, Controllable preparation of core–shell magnetic covalent-organic framework nanospheres for efficient adsorption and removal of bisphenols in aqueous solution, Chem. Commun. 53 (2017) 2511–2514.

[209] C.H. Yang, C.C. Cheng, D.J. Lee, Excess adsorption of phosphoric acid from extremely acidic solutions by covalent organic framework EB-COF:Br, Chemosphere 257 (2020) 127244.

[210] H. Wang, H. Wang, H. Jiang, A. Sheng, Z. Wei, Y. Li, Positively charged polysulfonamide nanocomposite membranes incorporating hydrophilic triazine-structured COFs for highly efficient nanofiltration, ACS Appl. Nano Mater. 3 (2020) 9329–9339.

[211] N.A. Khan, J. Yuan, H. Wu, T. Huang, X. You, A.U. Rahman, Covalent organic framework nanosheets as reactive fillers to fabricate free-standing polyamide membranes for efficient desalination, ACS Appl. Mater. Interfaces. 12 (2020) 27777–27785.

[212] X. Tan, Y. Fan, S. Wang, Y. Wu, W. Shi, T. Huang, Ultrasensitive and highly selective electrochemical sensing of sodium picrate by Dihydroxylatopillar[6]arene-modified gold nanoparticles and cationic Pillar[6]arene functionalized covalent organic framework, Electrochim Acta 335 (2020) 135706.

[213] C. Zhang, M. Cui, J. Ren, Y. Xing, N. Li, H. Zhao, Facile synthesis of novel spherical covalent organic frameworks integrated with Pt nanoparticles and multiwalled carbon nanotubes as electrochemical probe for tanshinol drug detection, Chem. Eng. J. 401 (2020) 126025.

[214] B. Ma, H. Guo, M. Wang, Q. Wang, W. Yang, Y. Wang, Electrocatalysis and simultaneous determination of hydroquinone and acetaminophen using PNCOF/graphene oxide modified electrode, Microchem J 155 (2020) 104776.

[215] Y. Sun, G.I.N. Waterhouse, L. Xu, X. Qiao, Z. Xu, Three-dimensional electrochemical sensor with covalent organic framework decorated carbon nanotubes signal amplification for the detection of furazolidone, Sensors Actuators B Chem. 321 (2020) 128501.

[216] X. Tan, Z. Zhang, T. Cao, W. Zeng, T. Huang, G. Zhao, Control assembly of Pillar[6]arene-modified Ag nanoparticles on covalent organic framework surface for enhanced sensing performance toward paraquat, ACS Sustain. Chem. Eng. 7 (2019) 20051–20059.

[217] Y. Xie, T. Zhang, Y. Chen, Y. Wang, L. Wang, Fabrication of core-shell magnetic covalent organic frameworks composites and their application for highly sensitive detection of luteolin, Talanta 213 (2020) 120843.

[218] J. Li, C. Zhang, M. Yin, Z. Zhang, Y. Chen, Q. Deng, Surfactant-sensitized covalent organic frameworks-functionalized lanthanide-doped nanocrystals: An ultrasensitive sensing platform for perfluorooctane sulfonate, ACS Omega 4 (2019) 15947–15955.

[219] L. Guo, Y. Song, K. Cai, L. Wang, On-off" ratiometric fluorescent detection of Hg^{2+} based on N-doped carbon dots-rhodamine B@TAPT-DHTA-COF, Spectrochim Acta Part A Mol. Biomol. Spectrosc. 227 (2020) 117703.

[220] H. Liu, Y. Zhang, D. Zhang, F. Zheng, M. Huang, J. Sun, A fluorescent nanoprobe for 4-ethylguaiacol based on the use of a molecularly imprinted polymer doped with a covalent organic framework grafted onto carbon nanodots, Microchim Acta 186 (2019) 182.

[221] M. Wang, M. Gao, L. Deng, X. Kang, K. Zhang, Q. Fu, A sensitive and selective fluorescent sensor for 2,4,6-trinitrophenol detection based on the composite material of magnetic covalent organic frameworks, molecularly imprinted polymers and carbon dots, Microchem. J. 154 (2020) 104590.

[222] P. Sun, J. Hai, S. Sun, S. Lu, S. Liu, H. Liu, Aqueous stable Pd nanoparticles/covalent organic framework nanocomposite: An efficient nanoenzyme for colorimetric detection and multicolor imaging of cancer cells, Nanoscale 12 (2020) 825–831.

[223] W.R. Cui, C.R. Zhang, W. Jiang, R.P. Liang, S.H. Wen, D. Peng, Covalent organic framework nanosheet-based ultrasensitive and selective colorimetric sensor for trace Hg^{2+} detection, ACS Sustain. Chem. Eng. 7 (2019) 9408–9415.

[224] W. Li, Y. Li, H.L. Qian, X. Zhao, C.X. Yang, X.P. Yan, Fabrication of a covalent organic framework and its gold nanoparticle hybrids as stable mimetic peroxidase for sensitive and selective colorimetric detection of mercury in water samples, Talanta 204 (2019) 224–228.

[225] M. Dogru, T. Bein, On the road towards electroactive covalent organic frameworks, Chem. Commun. 50 (2014) 5531–5546.

[226] S. Wan, J. Guo, J. Kim, H. Ihee, D. Jiang, A belt-shaped, blue luminescent, and semiconducting covalent organic framework, Angew Chem. Int. Ed. Engl. 47 (2008) 8826–8830.

[227] S. Wan, J. Guo, J. Kim, H. Ihee, D. Jiang, A photoconductive covalent organic framework: Self-condensed arene cubes composed of eclipsed 2D polypyrene sheets for photocurrent generation, Angew Chem. Int. Ed. Engl. 48 (2009) 5439–5442.

[228] X. Feng, L. Chen, Y. Honsho, O. Saengsawang, L. Liu, L. Wang, An ambipolar conducting covalent organic framework with self-sorted and periodic electron donor-acceptor ordering, Adv. Mater. 24 (2012) 3026–3031.

[229] X. Feng, L. Liu, Y. Honsho, A. Saeki, S. Seki, S. Irle, High-rate charge-carrier transport in porphyrin covalent organic frameworks: Switching from hole to electron to ambipolar conduction, Angew Chem. Int. Ed. Engl. 51 (2012) 2618–2622.

[230] X. Ding, J. Guo, X. Feng, Y. Honsho, J. Guo, S. Seki, Synthesis of metallophthalocyanine covalent organic frameworks that exhibit high carrier mobility and photoconductivity, Angew Chem. Int. Ed. Engl. 50 (2011) 1289–1293.

[231] X. Ding, X. Feng, A. Saeki, S. Seki, A. Nagai, D. Jiang, Conducting metallophthalocyanine 2D covalent organic frameworks: The role of central metals in controlling π-electronic functions, Chem. Commun. 48 (2012) 8952–8954.

[232] J.W. Colson, A.R. Woll, A. Mukherjee, M.P. Levendorf, E.L. Spitler, V.B. Shields, Oriented 2D covalent organic framework thin films on single-layer graphene, Science 332 (2011) 228–231.

[233] H. Wang, Z. Zeng, P. Xu, L. Li, G. Zeng, R. Xiao, Recent progress in covalent organic framework thin films: Fabrications, applications and perspectives, Chem. Soc. Rev. 48 (2019) 488–516.

[234] D. Cui, D.F. Perepichka, J.M. MacLeod, F. Rosei, Surface-confined single-layer covalent organic frameworks: Design, synthesis and application, Chem. Soc. Rev. 49 (2020) 2020–2038.

[235] S.L. Cai, Y.B. Zhang, A.B. Pun, B. He, J. Yang, F.M. Toma, Tunable electrical conductivity in oriented thin films of tetrathiafulvalene-based covalent organic framework, Chem. Sci 5 (2014) 4693–4700.

[236] D.D. Medina, M.L. Petrus, A.N. Jumabekov, J.T. Margraf, S. Weinberger, J.M. Rotter, Directional charge-carrier transport in oriented benzodithiophene covalent organic framework thin films, ACS Nano 11 (2017) 2706–2713.

[237] M.G. Mohamed, C.C. Lee, A.F.M. EL-Mahdy, J. Lüder, M.H. Yu, Z. Li, Exploitation of two-dimensional conjugated covalent organic frameworks based on tetraphenylethylene with bicarbazole and pyrene units and applications in perovskite solar cells, J. Mater. Chem. A 8 (2020) 11448–11459.

[238] J.M. Cox, B. Mileson, A. Sadagopan, S.A. Lopez, Molecular recognition and band alignment in 3D covalent organic frameworks for cocrystalline organic photovoltaics, J. Phys. Chem. C 124 (2020) 9126–9133.

[239] C. Wu, Y. Liu, H. Liu, C. Duan, Q. Pan, J. Zhu, Highly conjugated three-dimensional covalent organic frameworks based on spirobifluorene for perovskite solar cell enhancement, J. Am. Chem. Soc. 140 (2018) 10016–10024.

[240] S. Park, M.S. Kim, W. Jang, J.K. Park, D.H. Wang, Covalent organic nanosheets for effective charge transport layers in planar-type perovskite solar cells, Nanoscale 10 (2018) 4708–4717.

[241] K. Sinha Roy, D.R. Goud, A. Mazumder, B. Chandra, A.K. Purohit, M. Palit, Triazine-based covalent organic framework: A promising sorbent for efficient elimination of the hydrocarbon backgrounds of organic sample for GC–MS and 1H NMR analysis of chemical weapons convention related compounds, ACS Appl. Mater. Interfaces. 11 (2019) 16027–16039.

[242] J. He, F. Xu, Z. Chen, X. Hou, Q. Liu, Z. Long, AuNPs/COFs as a new type of SERS substrate for sensitive recognition of polyaromatic hydrocarbons, Chem. Commun. 53 (2017) 11044–11047, doi:10.1039/C7CC06440C.

[243] Y. Su, D. Wu, J. Chen, G. Chen, N. Hu, H. Wang, Ratiometric surface enhanced raman scattering immunosorbent assay of allergenic proteins via covalent organic framework composite material based nanozyme tag triggered Raman signal "turn-on" and amplification, Anal. Chem. 91 (2019) 11687–11695.

[244] D. Yao, C. Li, H. Wang, G. Wen, A. Liang, Z. Jiang, A new dual-mode SERS and RRS aptasensor for detecting trace organic molecules based on gold nanocluster–doped covalent-organic framework catalyst, Sensors Actuators B Chem. 319 (2020) 128308.

[245] W. Cao, W.D. Wang, H.S. Xu, I.V. Sergeyev, J. Struppe, X. Wang, F. Mentink-Vigier, Z. Gan, M.X. Xiao, L.Y. Wang, G.P. Chen, S.Y. Ding, S. Bai, W. Wang, Exploring applications of covalent organic frameworks: Homogeneous reticulation of radicals for dynamic nuclear polarization, J. Am. Chem. Soc. 140 (2018) 6969–6977.

[246] N. Singh, J. Kim, J. Kim, K. Lee, Z. Zunbul, I. Lee, Covalent organic framework nanomedicines: Biocompatibility for advanced nanocarriers and cancer theranostics applications, Bioact. Mater. 21 (2023) 358–380.

[247] J.Y. Zeng, X.S. Wang, B.R. Xie, M.J. Li, X.Z. Zhang, Covalent organic framework for improving near-infrared light induced fluorescence imaging through two-photon induction, Angew Chem. Int. Ed. Engl. 59 (2020) 10087–10094.

[248] G.S. He, L.S. Tan, Q. Zheng, P.N. Prasad, Multiphoton absorbing materials: Molecular designs, characterizations, and applications, Chem. Rev. 108 (2008) 1245–1330.

[249] J. Wang, L. Zhao, B. Yan, Indicator displacement assay inside dye-functionalized covalent organic frameworks for ultrasensitive monitoring of sialic acid, an ovarian cancer biomarker, ACS Appl. Mater. Interfaces. 12 (2020) 12990–12997.

[250] D. Liang, X. Zhang, Y. Wang, T. Huo, M. Qian, Y. Xie, Magnetic covalent organic framework nanospheres-based miRNA biosensor for sensitive glioma detection, Bioact. Mater. 14 (2022) 145–151.

[251] L. Bai, S.Z.F. Phua, W.Q. Lim, A. Jana, Z. Luo, H.P. Tham, Nanoscale covalent organic frameworks as smart carriers for drug delivery, Chem. Commun. 52 (2016) 4128–4131.

[252] A. Rengaraj, P. Puthiaraj, Y. Haldorai, N.S. Heo, S.K. Hwang, Y.K. Han, Porous covalent triazine polymer as a potential nanocargo for cancer therapy and imaging, ACS Appl. Mater. Interfaces. 8 (2016) 8947–8955.

[253] S. Liu, C. Hu, Y. Liu, X. Zhao, M. Pang, J. Lin, One-pot synthesis of DOX@covalent organic framework with enhanced chemotherapeutic efficacy, Chemistry 25 (2019) 4315–4319.